University of Trento

Department of Physics

Doctoral Thesis

~ · ~

Submitted to the

Doctoral School of Physics - XXXVIII cycle

by

Chiara Rogora

Physics of ultracold spin mixtures in low and stable magnetic field environment

Supervisor
Prof. Gabriele Ferrari

Final examination date: April 2026

Contents

Introduction

Bose Einstein Condensate (BEC) is a particular phase of matter emerging when an ensemble of bosons is cooled down to sufficiently low temperatures, characterized by a macroscopic occupation of the lowest-energy quantum state of the system.

The study of these systems became more and more attractive thanks to the development of techniques to cool and trap atoms from '80s [1]. They allow atomic gases to be cooled down to temperatures on the order of hundreds of nanokelvin, typically below the degeneracy temperature at which the phase transition to BEC occurs. The first monoatomic BECs of alkaline atoms were experimentally realized in 1995 by the group of Cornell and Wienman, who created condensates of ^{87}Rb [2], and by the group of Ketterle, who produced condensates of ^{23}Na [3]. Since then, ultra-cold atomic BECs have become a rich area of research. Initially, their fundamental properties such as long-range coherence, superfluid character, thermodynamics, topological excitations and many others have been investigated by many groups. Then, in recent years these systems have also begun to be employed as quantum simulators and as analogue models, thanks to their long time coherence, their superfluid character and their high degree of controllability: a wide range of parameters can be easily tuned, and ad hoc external potentials can be engineered.

The first condensates were trapped using magnetic traps, which could only trap low-field-seeking states. As a result, these were scalar condensates in which the spin degree of freedom was frozen, since all atoms occupied the same magnetic state. Then, the employment of different trapping techniques exploiting optical potentials [4] allowed the confinement of different magnetic sublevels within the same spatial region. This advancement paved the way for the creation of mixtures with magnetic character having more than one macroscopically occupied quantum state, exploiting internal degrees of freedom of the atoms. These systems are described by a multi-component wave function [5] and exhibit much richer properties and dynamics compared to single-component BECs. They maintain the superfluid properties characteristics of single-component BECs but also display magnetic properties arising

from their spin structure. Moreover, they offer the possibility of population transfer between different components, giving rise to internal state dynamics.

In particular, a distinction can be made between pseudo-spin systems and spinor condensates. Pseudo-spin systems consist of mixtures of atomic states belonging to different hyperfine manifolds. In this case the interconversion mechanism between components can be induced through a coherent coupling by external radiation fields, such as microwave or radio-frequency transitions. In contrast, spinor condensates involve mixtures of magnetic sublevels within the same hyperfine manifold, where population transfer between components may arise from spin-changing collisions, a purely interaction-driven mechanism. A crucial aspect of magnetic mixtures is that the energy of each internal state depends on the external magnetic field via the Zeeman shift. Therefore, achieving and maintaining a highly stable magnetic field is essential to ensure well-defined energy levels and to preserve the coherence and controllability. There are experimental contexts in which it is sufficient to have a high stability of the magnetic field, as it happens in the first experiment discussed in the thesis about the observation of dynamical properties of ferromagnetic superfluid, and other contexts in which the key constraints relate to the magnetic field magnitude, which in general should be minimized below a threshold depending on the process to be studied. In particular, the second experiment described in this thesis is about the development of a technique to characterize very low magnetic fields in order to create quasi-zero magnetic field environment where novel phases of matter can be studied. The high control of magnetic field required in this thesis is obtained by employing a magnetic shield that surrounds the science chamber in which the experiments take place, attenuating external magnetic field by 6 orders of magnitudes.

For the purposes of this thesis, two types of BEC mixture of ^{23}Na are employed. On one hand, the immiscible pseudo-spin 1/2 mixture, realized using the two hyperfine states $|F = 1, m_F = -1\rangle$ and $|F = 2, m_F = -2\rangle$, which are coherently coupled by a microwave field. On the other hand, the spin-1 spinor condensate, characterized by antiferromagnetic interactions and composed of magnetic sublevels of the $|F = 1\rangle$ hyperfine manifold.

In the first part of this thesis I consider the pseudo-spin mixture. The Hamiltonian of this mixture, in one dimension, is formally equivalent to a continuous version of the transverse-field Ising model, describing magnetic systems at zero temperature [6, 7]. Within this mapping, the ratio between the intraspecies interaction energy and the coherent coupling strength plays the role of the effective control parameter: the non-linear interaction term originates from the self-interaction energy, while the coupling acts as a transverse field [8]. As the ratio is tuned across unity, the ground state of the system exhibits

a qualitative change. When the coupling dominates over the interactions, the system is in a paramagnetic phase. Conversely, when the interactions prevail, the system is in an ordered ferromagnetic phase characterized by two equivalent and opposite magnetizations. The emergence of these degenerate ground states signals the occurrence of a second-order quantum phase transition, taking place thanks to the immiscibility properties of the mixture in the absence of coherent coupling [9]. In the condensed matter magnetic framework, the degeneracy between the two ferromagnetic states can be lifted by introducing a longitudinal field. In the atomic framework the degeneracy is broken by the detuning between the coupling radiation and the resonant transition frequency of the non-interacting atoms.

Owing to the correspondence with the transverse field Ising model, the coherently coupled atomic mixture provides a powerful platform for exploring ferromagnetic behavior and quantum critical phenomena in superfluids. In particular, the static properties characterizing magnetic materials have been experimentally demonstrated in [8], such as the emergence of hysteresis cycle upon varying the detuning of the coupling between the two components. The presence of hysteresis enables controlled access to different regions of the ferromagnetic landscape, allowing deterministic preparation of the condensate either in the global energy minimum, or in metastable local minima at higher energy.

The capability to engineer metastability on the superfluid makes the system particularly suitable for investigating non-equilibrium decay processes. In a classical scenario, the relaxation from a local minimum would proceed via the interplay of thermally activated barrier crossing and the energy balance including the creation of magnetic domains. In contrast, for a quantum field system such as a zero temperature ferromagnetic Bose-Einstein condensate, the decay is triggered by quantum fluctuations via the mechanism known as False Vacuum Decay (FVD). This is a non-perturbative phenomenon in quantum field theory originally formulated in high-energy and cosmological contexts to describe the transition from a metastable vacuum to the ground state.

False vacuum decay consists in the transition from an extended metastable state (the false vacuum) to the absolute ground state (the true vacuum), occurring via the probabilistic formation of a resonant bubble of true vacuum within the false vacuum background. Once formed, the bubble expands across the system because it is energetically favorable. In the zero temperature limit, this process is entirely driven by quantum fluctuations and it is quantitatively described by instanton theory [10], later generalized to the finite temperature case [11]. The theory predicts an exponential dependence of the decay rate on the properties of the potential barrier separating the two minima.

The observation of FVD is notoriously challenging due to the exponentially-dependent timescales upon the system's parameters. Ultracold atomic gases overcome this limitation thanks to their long coherence time and high tunability, in contrast to typical solid state systems that suffer from rapid incoherent dissipation. Exploiting these advantages, bubble nucleation has been directly observed in a ferromagnetic Bose-Einstein condensate in Trento [12], by preparing the superfluid in a metastable local energy minimum and monitoring its relaxation towards the true ground state. This observation was later followed by others in different platforms [13, 14]. In [12], the decay time was characterized as a function of the control parameters determining the shape of the barrier at fixed temperature, showing agreement with numerical simulations and with an analytic model based on instanton theory adapted to the microscopic properties of our superfluid mixture.

Building upon the results reported in [12], the present thesis introduced a protocol for controlling the sample temperature, enabling a systematic investigation of thermal effects on the decay dynamics. I will show that the experimental results are consistent with the finite temperature extension of instanton theory: increasing temperature accelerates the decay, reflecting the enhancement of the tunneling rate due to thermal fluctuations.

In the second part of this thesis, I shifted my focus on the $F = 1$ spinor mixture. An interesting aspect of this mixture is that its mean field ground state is determined by minimizing an energy functional containing two competing contributions. The first contribution arises from the Zeeman shift, which is proportional to the strength of the external magnetic field. In particular, if the system magnetization is conserved, the linear Zeeman term contributes only a uniform energy offset and can therefore be disregarded and the quadratic Zeeman shift plays a crucial role in determining the structure of the ground state. The Zeeman term energetically favors accumulation of atoms in the $|F = 1, m_F = 0\rangle$ state. A second energy contribution originates from spin-dependent contact interactions, which in the case of sodium have an antiferromagnetic character. At the mean field level, these interactions favor configurations where atoms organize in the $|F = 1, m_F = -1\rangle$ and $|F = 1, m_F = 1\rangle$ states, with the relative populations determined by the total magnetization of the system. As a result of the competition between the quadratic Zeeman and contact magnetic interaction, the system undergoes a second order phase transition as the magnetic field is varied. For large enough quadratic Zeeman energy, the system ground state is in a Broken-Axisymmetry (BA) phase, dominated by the population of $m_F = 0$ state. For sufficiently low magnetic fields, the antiferromagnetic phase is favored, with atoms redistributed between the $m_F = \pm 1$ states. The first experimental study of the equilibrium phase diagram of a $F = 1$ sodium con-

densate with antiferromagnetic interactions was reported in [15]. In this work, a small atomic sample, consisting of a few thousand atoms, was employed. For such a system the critical magnetic field associated with the transition from the BA phase to the antiferromagnetic phase is on the order of hundreds of milligauss. The experimentally measured phase diagram was found to be in quantitative agreement with the predictions of mean-field theory.

Further theoretical studies [16, 17] have investigated the system beyond the mean field approximation, predicting the emergence of a fragmented many body ground state characterized by super-Poissonian fluctuations of the Zeeman populations in the three $|m_F\rangle$ states. Experimentally observing such a state is particularly challenging due to its fragility with respect to perturbations that break spin-rotational symmetry. In our system, the main symmetry-breaking mechanism is provided by the quadratic Zeeman effect, which favors the occupation of the $|m_F = 0\rangle$ state. In particular, the typical width of the crossover region between the fragmented many-body ground state and the conventional condensate state is predicted to decrease with increasing atom number, implying that larger systems require increasingly smaller symmetry-breaking perturbations to favor the conventional condensate state. Experimental evidence of such beyond-mean-field physics has been achieved in zero-dimensional (0D) systems [18, 19], where a state close to the expected many-body ground state has been observed. These experiments demonstrate how the interplay between symmetry and interactions can generate strong quantum correlations and entanglement in mesoscopic quantum systems. In a one-dimensional (1D) experimental configuration, however, the critical magnetic field associated with the phase transition is expected to be extremely small, on the level of tens of μG. As a consequence, even tiny residual magnetic fields can dominate over the spin-interaction energy, thereby suppressing the transition. Therefore, to observe this phase transition, a very precise technique to characterize and compensate the residual magnetic field is required.

My contribution to this problem lies in the development of such a technique, based on Landau-Zener spectroscopy. With this technique the atoms play the role of sensors for the magnetic field which allows us to characterize the magnetic field with a precision of the order of 10 μG, which is expected to be sufficiently low to observe the phase transition mentioned above.

The thesis is organized in the following Chapters:

- Chapter 1 provides an overview of the theoretical foundations of Bose Einstein Condensation (BEC) and presents the wide variety of possible atomic mixtures that can be realized. The Chapter first focuses on pseudo-spin 1/2 mixtures, illustrating how the ferromagnetic phase transition occurs in such systems. It then turns to the $S = 1$ spinor

condensate, discussing its behavior at the mean-field level and beyond mean-field discussing the role of interactions and external field in determining the ground state.

- Chapter 2 provides a description of the experimental apparatus and the tools available in our laboratory. Here I outline the experimental procedure employed to produce a Bose-Einstein condensate, including the cooling and trapping stages, as well as the imaging techniques used to detect and analyze the atomic cloud. Finally the Chapter presents the spectroscopic methods adopted for magnetic field characterization.

- Chapter 3 discusses the observation of the dependence of False Vacuum Decay (FVD) on temperature in a sperfluid metastable ferromagnetic mixture. I introduce the instanton theory, which is a semiclassical analytical model describing the relaxation of a metastable field, and its generalization to finite temperature, showing how it applies to coherently coupled BECs. The Chapter then describes the experimental procedure used to generate bubbles of true vacuum from the metastable ferromagnetic state, and how to vary and measure the T of the sample, followed by a presentation and discussion of the experimental results obtained.

- Chapter 4 introduces the theoretical background of Landau-Zener spectroscopy and explains how it can be exploited for high-precision residual magnetic field characterization. It describes the experimental implementation of the technique for the characterization of such a magnetic field, both in the transverse and longitudinal directions, and presents the results obtained.

Chapter 1

Theory of Bose Einstein Condensates

This Chapter presents the theoretical framework of relevance to this thesis. We first review the basic principles of BEC theory. We then describe the dynamics of the condensate within the mean field approximation by introducing the Gross-Pitaevskii equation, governing the behavior of a homogeneous, weakly interacting diluite Bose gas at zero temperature.

After the discussion of the properties of a single component BEC, we extend the analysis to multicomponent systems. We briefly review the different types of condensate mixtures that have been experimentally realized, then we focus on two cases of particular relevance to this work. The first is a coherently coupled pseudo-spin 1/2 mixture, which exhibits a ferromagnetic behavior; for this system the Gross-Pitaevskii equation is generalized to account for coherent coupling leading to interchange mechanism between components. The second is a $S = 1$ spinor condensate with antiferromagnetic interactions. This system is initially analyzed within mean-field theory and the single mode approximation, showing the emergence of a second-order phase transition driven by the competition between interaction energy and magnetic-field-induced energy shift. Finally, we discuss the role of beyond mean-field effects and their impact on the behavior of the system.

1.1 Bose Einstein Condensation

The concept of Bose-Einstein condensation (BEC) was first theoretically proposed in 1924 by Bose [20], in his work on the statistical description of quanta of light. Then the same idea was extended by A. Einstein [21] to massive particles.

BEC is a thermal phase transition which occurs when an ideal gas of identical bosons is cooled below a critical temperature T_c which depends on the density of the particles. Below this threshold, a macroscopic fraction of particles occupies the lowest energy state. This phenomenon emerges only in the thermodynamic limit and it occurs even in the absence of interactions, since it is driven only by quantum statistics [22].

As a phase transition, Bose-Einstein condensation is characterized by the appearance of a macroscopic complex order parameter which vanishes above T_c and becomes finite below it. This quantity, identified with the condensate wave function, characterizes the collective quantum state of the system and signals the appearance of long-range coherence among particle sharing the same quantum state.

From a symmetry perspective, Bose-Einstein condensation is associated with the spontaneous breaking of global $U(1)$ symmetry. Although the system's Hamiltonian remains invariant under global transformation, the condensate wave function acquires a definite phase, thereby selecting a particular direction in phase space and breaking the continuous symmetry of the underlying Hamiltonian.

1.1.1 Scattering in ultracold gases

The treatment can be extended by including interparticle interactions, which play a crucial role in determining the properties of the condensate ground state. At the extremely low temperatures required for Bose-Einstein condensation, a system would be expected to form a solid state phase. To realize an ultracold gas, the particle density must be kept sufficiently low in order to suppress the process of three-body recombination. Consequently, interactions in ultracold dilute gases are dominated by two-body collisions. These interactions are typically weak and short-ranged, allowing the system to be well described within the weak-coupling approximation. It consists of replacing the true, generally unknown, short-range interatomic potential with a simplified effective interaction that neglects the short-range dynamics while preserving the correct low-energy scattering properties. In particular, the effective potential reproduces the same s-wave scattering length of the original interaction, since this single parameter provides a universal characterization of low-energy collisions.

The validity of this approximation relies on the diluteness condition of the gas, quantified by the condition $na^3 \ll 1$. Here, n denotes the atomic density, corresponding to an average interparticle distance $d = n^{-1/3}$ while a is the scattering length. Under these conditions, the average distance between particles greatly exceeds the interaction range, ensuring that two-body scattering processes are effectively unaffected by the presence of other atoms and higher

order scattering processes can be neglected.

The diluteness criterion is well satisfied in ultracold dilute atomic gases, justifying the use of a contact pseudopotential such as the commonly adopted Fermi-contact pseudopotential,

$$V = g\delta(\mathbf{r}) \tag{1.1}$$

where $\delta(\mathbf{r})$ is the Dirac distribution and g is interaction constant which is related to the s-wave scattering length by

$$g = \frac{4\pi\hbar^2 a}{m} \tag{1.2}$$

This contact potential is isotropic and, therefore, invariant under rotations.

1.2 Gross-Pitaevskii Equation

The Gross-Pitaevskii Equation (GPE) provides a mean-field description of a Bose-Einstein condensate in terms of the evolution of the macroscopic order parameter [23]. Its derivation relies on the assumption that the gas is fully described by the order parameter and the thermal fluctuations are neglected. Under these conditions, the complex many-body problem is significantly simplified while the exact ground state is, in general, not accessible through analytical methods. The resulting equation has the form of a nonlinear Schroedinger equation, where the nonlinearity arises from interparticle interactions.

Within these approximations, the N-body Hamiltonian of the system can be expressed in second quantization as:

$$\hat{H} = \int d\mathbf{r} \left[\hat{\Psi}^+(\mathbf{r}) \left(-\frac{\hbar^2}{2m}\nabla^2 + V_{ext} \right) \hat{\Psi}(\mathbf{r}) + \frac{g}{2}\hat{\Psi}^+(\mathbf{r})\hat{\Psi}^+(\mathbf{r})\hat{\Psi}(\mathbf{r})\hat{\Psi}(\mathbf{r}) \right] \tag{1.3}$$

where m is the particle mass, $V_{\text{ext}}(\mathbf{r})$ is the external trapping potential, $\hat{\Psi}(\mathbf{r})$ is the bosonic quantum field operator describing particle distribution, and g is the interaction strength describing the two-body collisions, introduced in the previous Section.

The central approximation underlying the GPE consists in assuming that all particles are in the condensate, thereby neglecting quantum fluctuations and particle-number depletion from the ground state. Within this framework the system quantum nature is hidden and field operators are replaced by a classical complex field according to

$$\begin{cases} \hat{\Psi}(\mathbf{r}) \to \langle \hat{\Psi}(\mathbf{r}) \rangle = \Psi(\mathbf{r}) \\ \hat{\Psi}^+(\mathbf{r}) \to \langle \hat{\Psi}^+(\mathbf{r}) \rangle = \Psi^*(\mathbf{r}) \end{cases} \tag{1.4}$$

$\Psi(\mathbf{r})$ is the condensate wave function, and the local particle density is given by $n(\mathbf{r}) = |\Psi(\mathbf{r})|^2$.

The condensate order parameter is identified with the average of the expectation value of the field operator,

$$\langle\hat{\Psi}(\mathbf{r})\rangle = \Psi(\mathbf{r}) = \sqrt{n(\mathbf{r})}e^{i\phi} \tag{1.5}$$

where ϕ is the global phase.

Under this assumption, the expectation value of the system energy can be written as the functional

$$E_0 = \int d\mathbf{r}\left[\Psi^*(\mathbf{r})\left(-\frac{\hbar^2\nabla^2}{2m} + V_{\text{ext}}(\mathbf{r})\right)\Psi(\mathbf{r}) + \frac{g}{2}|\Psi(\mathbf{r})|^4\right] \tag{1.6}$$

The stationary GPE is obtained by minimizing this energy functional with respect to $\Psi^*(\mathbf{r})$ with the normalization constraints to the total number of particles N. This constraint is enforced through the introduction of a Lagrange multiplier μ, which can be identified with the chemical potential. The resulting equation reads

$$\left(-\frac{\hbar^2\nabla^2}{2m} + V_{\text{ext}}(\mathbf{r})\right)\Psi(\mathbf{r}) + g|\Psi(\mathbf{r})|^2\Psi(\mathbf{r}) = \mu\Psi(\mathbf{r}) \tag{1.7}$$

whose solutions determine the ground state properties of the condensate.

The time dependent GPE can be obtained by minimizing the action associated with the system and takes the form:

$$i\hbar\frac{\partial}{\partial t}\Psi(\mathbf{r},t) = \left(-\frac{\hbar^2\nabla^2}{2m} + V_{ext}(\mathbf{r})\right)\Psi(\mathbf{r},t) + g|\Psi(\mathbf{r},t)|^2\Psi(\mathbf{r},t) \tag{1.8}$$

Although the derivation assumes that all particles are condensed and neglects quantum depletion due to interactions, the GPE provides an accurate description of the system not only at zero temperature, but also at finite yet sufficiently low temperatures, where thermal and quantum fluctuations remain small.

1.2.1 Thomas-Fermi limit

This regime corresponds to neglecting the quantum pressure term, proportional to $\frac{\hbar^2\nabla^2}{2m}$, which allows for a simplified description of the condensate and its ground state. Such an approximation is justified for homogeneous systems or whenever the density varies slowly over space. In the presence of a non uniform external potential, it is useful to introduce the healing length, characterizing the distance over which the condensate order parameter recovers from zero

to its bulk value. The quantum pressure term becomes significant when the density varies sharply over a length scale such that kinetic and interaction energies are comparable. This characteristic healing length is given by [24, 25]

$$\xi = \frac{1}{\sqrt{8\pi a n}} \tag{1.9}$$

where a is the s-wave scattering length and n the condensate density. The healing length, therefore sets the minimum size of density modulations or excitations in the condensate.

In the dilute regime ($na^3 \ll 1$), the healing length is much larger than the mean interparticle distance. Two distinct regimes can be recognized depending on the relative magnitude of the condensate size and the healing length. If the condensate radius is much smaller than ξ, the kinetic energy contribution dominates over the interactions energy, and interactions can be treated as perturbative corrections to the non interacting case. Conversely, when the condensate radius is much larger than the healing length, the interaction energy wins over the kinetic energy which becomes negligible. In this latter situation, the Thomas-Fermi approximation applies and and it well describes the system ground state in typical experimental conditions.

Within the Thomas-Fermi limit, the stationary GPE reduces to the simple form

$$V_{\text{ext}}\psi(\mathbf{r}) + gn\psi(\mathbf{r}) = \mu\psi(\mathbf{r}) \tag{1.10}$$

from which a simple expression for the density profile follows

$$\begin{cases} \frac{\mu - V_{\text{ext}}}{g} & \mu - V_{\text{ext}} > 0 \\ 0 & \mu - V_{\text{ext}} < 0 \end{cases} \tag{1.11}$$

This solution clearly highlights the necessity of a positive interaction constant g, corresponding to repulsive inter-particle interactions. Conversely, in the presence of an attractive interaction, no mechanism would counterbalance the attractive forces, leading to the collapse of the condensate [26]. Furthermore, the solution shows that the density distribution is fully determined by the external trapping potential.

In the case of a harmonic confinement characterized by frequencies ω_x, ω_y and ω_z, the density profile takes the form of an inverted parabola in each spatial direction, peaked at the center of the trap where $gn_0 = \mu$. Explicitly, the density reads

$$n(\mathbf{r}) = \frac{\mu}{g}\left(1 - \frac{x^2}{R_x^2} - \frac{y^2}{R_y^2} - \frac{z^2}{R_z^2}\right) \tag{1.12}$$

Where the Thomas-Fermi radii are defined as

$$R_{x,y,z} = \sqrt{\frac{2\mu}{m\omega_{x,y,z}^2}} \tag{1.13}$$

The value of the chemical potential μ is determined by the normalization condition on the total number of particles,

$$N = \int d\mathbf{r} n(\mathbf{r}) \tag{1.14}$$

which yields to

$$\mu = \frac{\hbar\omega_{\text{ho}}}{2}\left(\frac{15Na}{a_{\text{ho}}}\right)^{2/5} \tag{1.15}$$

where $a_{\text{ho}} = \sqrt{\hbar/(m\omega_{\text{ho}})}$ is the oscillator length associated to the geometric average $\omega_{\text{ho}} = \sqrt[3]{\omega_x\omega_x\omega_y}$ of the oscillator angular frequencies. The chemical potential thus represents the energy per particle in the condensate and it corresponds to the energy required to extract one particle from the cloud.

1.2.2 Quantum Mixtures

It is also possible to confine different atomic species within the same spatial region, realizing quantum mixtures characterized by the simultaneous macroscopic occupation of more than a single quantum state. These types of systems offer a much richer dynamics and many-body behavior compared to singe component BECs.

Thanks to advances in cooling and trapping techniques, a wide variety of ultracold atomic mixtures has been experimentally realized.

Heteronuclear mixtures can be obtained by trapping different atomic species together. These include mixtures of two bosonic species, such as $^{41}\text{K} - ^{87}\text{Rb}$ [27], $^{7}\text{Li} - ^{133}\text{Cs}$ [28], and $^{133}\text{Cs} - ^{87}\text{Rb}$ [29]; mixtures of two fermionic species, such as $^{40}\text{K} - ^{6}\text{Li}$ [30, 31]; or Bose-Fermi mixtures such as $^{40}\text{K} - ^{23}\text{Na}$ [32], $^{6}\text{Li} - ^{41}\text{K}$ [33], $^{6}\text{Li} - ^{7}\text{Li}$ [34], [35] or $^{40}\text{K} - ^{87}\text{Rb}$ [36].

In this thesis, however, we focus on homonuclear mixtures, which are realized by exploiting the atomic internal degrees of freedom of a single atomic isotope. In this case, the system consists of one atomic species described by a multicomponent order parameter, preserving the superfluid properties of a single-component condensate while simultaneously exhibiting magnetic behavior arising from its spin structure. Such systems are typically realized using alkali, alkaline-earth atoms, transition metal atoms and lanthanide atoms.

The main difference between heteronuclear and homonuclear mixtures lies in the conservation of population of each component. In heteronuclear mixtures, the particle numbers of each species are fixed, and the system properties are determined by mean-field interaction energy. Conversely, in homonucear mixtures the relative populations of the components are not necessarily conserved, as various interconversion mechanisms between different internal states are possible.

In this context, it is useful to make a distinction between pseudo-spin systems and spinor condensates. Pseudo-spin systems are mixtures of atomic states belonging to different hyperfine manifolds, where interconversion between components can be induced via coherent coupling by external radiation fields. Spinor condensates, on the other hand, involve different magnetic sublevels within the same hyperfine manifold; in this case, component interconversion mechanism occurs through spin-changing collisions. These mixtures have been experimentally realized using both alkali and alkaline-earth atoms, where long coherence times enable for the study of systems with effective spin $S = 1/2$ [37, 38, 39], $S = 1$ [40, 41, 42], and $S = 2$ [43].

1.2.3 Miscibility condition

Due to the presence of internal degrees of freedom, the system can be described by a multi-component order parameter. In order to analyze the miscibility condition let us focus on a two component BEC described by

$$\Psi(\mathbf{r}) = e^{i\theta} \begin{pmatrix} \psi_1(\mathbf{r}) \\ \psi_2(\mathbf{r}) \end{pmatrix} \tag{1.16}$$

where $\psi_i(\mathbf{r}) = \sqrt{n_i(\mathbf{r})}e^{i\phi_i}$ with $i = 1, 2$, labeling the two atomic species, are the two classical complex fields where $n_i(\mathbf{r})$ and ϕ_i denote the density and phase of i-component, respectively, and θ is the global phase associated with the condensate.

In the presence of spin-dependent interactions, the interaction term of the Hamiltonian can be written as

$$V = \frac{1}{2}\sum_{\sigma,\sigma'} \int d\mathbf{r}d\mathbf{r}' V_{\sigma,\sigma'}(\mathbf{r}-\mathbf{r}')\psi^+_\sigma(\mathbf{r})\psi^+_{\sigma'}(\mathbf{r}')\psi_{\sigma'}(\mathbf{r}')\psi_\sigma(\mathbf{r}) \tag{1.17}$$

where $\sigma, \sigma' = 1, 2$ label the two components.

The system is characterized by two intra-component interaction potentials, $V_{1,1}$ and $V_{2,2}$, and one inter-component interaction potential $V_{1,2}$, each one characterized by its own s-wave scattering length. In the diluite and ultracold regime, each one of these interactions is well approximated by an appropriate

effective contact potential, leading to three different coupling constants. The two intra-component interaction constants are given by

$$g_{ii} = \frac{4\pi\hbar^2 a_{ii}}{m_i} \qquad i = 1, 2 \tag{1.18}$$

while the the inter-component coupling constant reads

$$g_{12} = \frac{2\pi\hbar^2 a_{12}}{m_r} \tag{1.19}$$

where m_r is the reduced mass of the two interacting species.

Within the mean-field approximation, the interaction energy density can be expressed as

$$\epsilon = \frac{1}{2} g_{11} n_1^2 + \frac{1}{2} g_{22} n_2^2 + g_{12} n_1 n_2 \tag{1.20}$$

The ground state of the system, obtained by minimizing this energy density, depends on the relative value of the coupling constants, giving rise to distinct physical regimes. Assuming repulsive intra-component interactions ($g_{11} > 0$ and $g_{22} > 0$), necessary condition to ensure stability against collapse, two qualitatively different situations arise when the inter-component interaction is also repulsive. They are represented in Fig. 1.1.

- If $g_{12}^2 < g_{11} g_{22}$, the intra-species interactions dominate over the inter-component one. In this regime, the energy is minimized when the two components spatially overlap, resulting in a miscible mixture.

- If $g_{12}^2 > g_{11} g_{22}$, the inter-component interaction dominates over the inter-component one. This is the opposite situation in which the system minimizes its energy through spatial separation of the two components and the formation of an interface, leading to an immiscible mixture which energy is minimized minimizing the area of the interface.

The situation becomes more complex in the presence of attractive inter-component interactions. In this regime, the beyond mean field effects play a crucial role [44] and, under suitable conditions, they can favor self-bound states known as quantum droplets [45, 46, 47].

While the previous discussion strictly applies to a uniform box potential, the same qualitative behavior extends to harmonically trapped systems. In this case however, the miscibility condition is not sufficient to guarantee identical density profiles. Even in the miscible regime, the spatial distributions of the two components depend on the relative magnitude of the intra-component

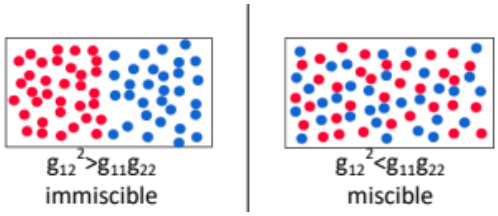

Figure 1.1: Immiscible mixture with phase separated components (left panel) and miscible mixture (right panel) in a box potential.

interaction strengths. In particular, equal density profiles are obtained only when $g_{11} = g_{22}$. Otherwise, the component with the larger intra-component interaction constant is pushed towards the edges of the trap, where the density is lower, while the other component accumulates near the trap center. This behavior of the system of having unequal spatial distributions is known as buoyancy.

In the presence of an interface between the two components, it is possible, by analogy with the healing length in single-component condensates, to define a spin healing length characterizing the width of the interface

$$\xi_s = \frac{\hbar^2}{\sqrt{m\delta g n}} \tag{1.21}$$

where $\hbar\delta g = \frac{g_{11}+g_{22}}{2} - g_{12}$.

It is important to note that both the concepts of miscibility and bouyancy are well defined only if the particle number in each component is conserved and no interconversion mechanisms, such as coherent coupling between internal states, are present.

1.3 S = 1/2 Pseudo-Spin Mixtures

1.3.1 GPE for Mixtures

The mean-field formalism developed in the previous section for a single component BEC can be easily extended to multi-component systems, which are described in terms of coupled GPEs. In the case of a two-component condensate, the system is characterized by two classical complex fields

$$\psi_i(\mathbf{r}) = \sqrt{n_i(\mathbf{r})}e^{i\phi_i} \qquad i = 1, 2 \tag{1.22}$$

representing the macroscopic wave functions of the two components.

Within this framework, the energy functional of the system takes the form

$$E_{1,2} = \int d\mathbf{r} \left(\left(\sum_{i=1,2} \frac{\hbar}{2m_i} |\nabla \psi_i(\mathbf{r})|^2 + V_i(\mathbf{r}) + \frac{1}{2} g_{ii}(\mathbf{r}) |\psi_i(\mathbf{r})|^4 \right) + g_{12} |\psi_1(\mathbf{r})|^2 |\psi_2(\mathbf{r})|^2 \right) \tag{1.23}$$

where m_i denote the masses of the two species, $V_i(\mathbf{r})$ are the trapping potentials, which in principle are different for the two species, $g_{ii} = \frac{4\pi\hbar^2 a_{ii}}{m_i}$ with $i = 1, 2$ are the inter-component coupling constants and $g_{12} = \frac{2\pi\hbar^2 a_{12}}{m_r}$ is the intra-component coupling constant, with $m_r = \frac{m_1 m_2}{m_1 + m_2}$ the reduced mass. By applying the variational principle independently for each of the two fields, one obtains a set of two coupled time-dependent Gross-Pitaevskii equations,

$$i\hbar \frac{\partial \psi_1(\mathbf{r}, t)}{\partial t} = \left(-\frac{\hbar^2 \nabla^2}{2m_1} + V_1(\mathbf{r}) + g_{11} |\psi_1(\mathbf{r}, t)|^2 + g_{12} |\psi_2(\mathbf{r}, t)|^2 \right) \psi_1(\mathbf{r}, t) \tag{1.24}$$

$$i\hbar \frac{\partial \psi_2(\mathbf{r}, t)}{\partial t} = \left(-\frac{\hbar^2 \nabla^2}{2m_2} + V_2(\mathbf{r}) + g_{22} |\psi_2(\mathbf{r}, t)|^2 + g_{12} |\psi_1(\mathbf{r}, t)|^2 \right) \psi_2(\mathbf{r}, t) \tag{1.25}$$

In the following we restrict our attention to a homonuclear pseudo-spin mixture, for which $m_1 = m_2 \coloneqq m$, and assuming that the external potential is engineered such that both components feel the same confinement, $V_1(\mathbf{r}) = V_2(\mathbf{r}) \coloneqq V_{\text{ext}}$. Under these conditions, the physical properties of the mixture are fully determined by the solutions of the coupled Gross-Pitaevskii equations.

In particular, stationary solutions give two chemical potentials, one for each component

$$\mu_1 \psi_1(\mathbf{r}) = \left(-\frac{\hbar^2 \nabla^2}{2m} + V_{ext}(\mathbf{r}) + g_{11} |\psi_1(\mathbf{r})|^2 + g_{12} |\psi_2(\mathbf{r})|^2 \right) \psi_1(\mathbf{r}) \tag{1.26}$$

$$\mu_2 \psi_2(\mathbf{r}) = \left(-\frac{\hbar^2 \nabla^2}{2m} + V_{ext}(\mathbf{r}) + g_{22} |\psi_2(\mathbf{r})|^2 + g_{12} |\psi_1(\mathbf{r})|^2 \right) \psi_2(\mathbf{r}) \tag{1.27}$$

1.3.2 Coherent coupling

The coupled GPEs derived so far rely on the assumption that the particle numbers of the two components are independently conserved. We now extend this framework by introducing an interconversion mechanism between the two

internal states. Such a mechanism can be experimentally realized by applying a microwave field acting homogeneously on the entire atomic cloud which coherently couples the two internal electronic states. In the absence of interactions, the system reduces to an effective two-level atom driven by an oscillating electromagnetic field.

Atom-field interaction Let us consider a two-level system irradiated by an electromagnetic field at frequency ω_L. The energy associated with the atomic transition between the two levels is given by

$$\hbar\omega_{12} = \hbar(\omega_2 - \omega_1) \tag{1.28}$$

where ω_1 and ω_2 denote the energies of the ground and excited states, respectively. The detuning of the driving field is defined as the difference between the atomic transition frequency and the field frequency.

$$\delta = \omega_{12} - \omega_L \tag{1.29}$$

The electromagnetic field is assumed to be linearly polarized along the x-direction and can be written as

$$E(t) = \vec{x}E_0 \cos(\omega_L t) \tag{1.30}$$

where E_0 is the field amplitude. The strength of the atom-field coupling is characterized by the Rabi frequency,

$$\Omega_R = \frac{E_0 p}{\hbar} \tag{1.31}$$

with p denoting the electric dipole matrix element associated with the transition. A generic atomic state, described by a wave function, can be expressed as

$$\Psi(\mathbf{r}, t) = c_2(t)u_2(\mathbf{r})e^{i\omega_2 t} + c_1(t)u_1(\mathbf{r})e^{-i\omega_1 t} \tag{1.32}$$

where $u_i(\mathbf{r})$ are the spatial wave functions of the two internal states and $c_i(t)$ are the corresponding probability amplitudes, satisfying the normalization condition $|c_1|^2 + |c_2|^2 = 1$. For a system initially prepared in the ground state, the population of the excited state undergoes Rabi oscillations. The probability of occupying the excited state is given by

$$|c_2(t)|^2 = \left(\frac{\Omega_R}{\Omega'}\right)^2 \sin^2\left(\frac{\Omega' t}{2}\right) \tag{1.33}$$

where $\Omega' = \sqrt{\Omega_R^2 + \delta^2}$ is the generalized Rabi frequency. At resonance ($\delta = 0$), the system oscillates at frequency Ω_R, and a complete population transfer can

be achieved by applying a π-pulse, meaning a pulse of duration $t = \pi/\Omega_R$. Away from resonance the transfer is never complete.

The coherent coupling between the two internal states introduces an additional contribution to the energy functional. Within the rotating-wave approximation, this term can be written as

$$E_{\rm cc} = -\frac{h\Omega_R(t)}{2}\int d\mathbf{r}\sqrt{n_1 n_2}cos(\phi_2-\phi_1) + \frac{\hbar\delta(t)}{2}\int d\mathbf{r}(n_2^2-n_1^2) \qquad (1.34)$$

where n_i and ϕ_i denote the density and phase of component i, respectively. This expression shows that the presence of the coherent coupling locks the relative phase $\phi = \phi_2 - \phi_1 = 0$ in order to minimize the energy. This locking of the phase reflects the symmetry breaking introduced by the presence of the coupling, since the particle numbers of the two states are no longer independently conserved.

By applying the variational principle to the full energy functional, one obtains a modified set of coupled GPEs

$$i\hbar\frac{\partial}{\partial t}\psi_1(\mathbf{r}) = \left(-\frac{\hbar^2\nabla^2}{2m} + V_{ext} + g_{11}|\psi_1(\mathbf{r})|^2 + g_{12}|\psi_2(\mathbf{r})|^2\right)\psi_1(\mathbf{r}) - \frac{\hbar\Omega_R(t)}{2}e^{i\delta t}\psi_2(\mathbf{r}) \qquad (1.35)$$

$$i\hbar\frac{\partial}{\partial t}\psi_2(\mathbf{r}) = \left(-\frac{\hbar^2\nabla^2}{2m} + V_{ext} + g_{22}|\psi_2(\mathbf{r})|^2 + g_{12}|\psi_1(\mathbf{r})|^2\right)\psi_2(\mathbf{r}) - \frac{\hbar\Omega_R(t)}{2}e^{-i\delta t}\psi_1(\mathbf{r}) \qquad (1.36)$$

These equations contain two terms, one due to the presence of the coherent coupling and one due to the interaction-induced mean-field effects. The two competing terms determine the ground-state properties of the system, and in particular lead to the emergence of a quantum phase transition, as discussed in the following.

.

1.3.3 Landau Lifshitz Model

The Landau-Lifshitz Equations (LLE) [48, 49] describe the evolution of the magnetization in ferromagnetic materials under the action of an effective magnetic field which includes contributions from the external magnetic field, the material anisotropy, and the magnetization of the system itself.

The dynamics of the system is simply given by a precession of the magnetization around the effective magnetic field on the Bloch sphere. However, the effective field is in general a non trivial function of the magnetization itself. Moreover, in real magnetic materials dissipation effects are present, which are

commonly modeled by a viscous damping term driving the magnetization toward alignment with the effective field, eventually suppressing the dynamics. In the following, it is shown that the dynamics of a two-component BEC mixture can be mapped onto undamped LLE. This equivalent formulation of the spin dynamics can be derived starting from the GPEs and writing the order parameter as a spinor complex field.

Reduction of the GPE to the LLE The dynamics of a two-component system in the presence of a coherent radiation field can be described, within the Rotating Wave Approximation (RWA) and neglecting decoherence and relaxation mechanism, by the Landau-Lifshitz Equation (LLE) derived from the two coupled GPEs through a separation of variables between the spin and the density degrees of freedom.

This derivation is carried out using the complex spinorial representation of the condensate wave function. It is a convenient formulation since it allows for a natural interpretation of the system as an effective spin system. The spinor field is defined as

$$\Psi = \begin{pmatrix} \psi_1(\mathbf{r}) \\ \psi_2(\mathbf{r}) \end{pmatrix} \tag{1.37}$$

with Hermitian conjugate

$$\Psi^+ = (\psi_1^*(\mathbf{r}), \psi_2^*(\mathbf{r})) \tag{1.38}$$

where $\psi_i = \sqrt{n_i} e^{i\phi_i}$ is the order parameter of the i-th component.

The system dynamics can be described in terms of the density matrix. In the following, all quantities depend on $\mathbf{r}$, although this dependence is omitted for readability. The density matrix is defined as

$$\rho = \Psi \times \Psi^+ = \begin{pmatrix} n_1 & \psi_1\psi_2^* \\ \psi_1^*\psi_2 & n_2 \end{pmatrix} \tag{1.39}$$

Exploiting the SU(2) algebra, the set of Pauli matrices σ_i (with i = 1,2,3) can be used as a basis to define the spin vector of the coupled BEC through the density matrix:

$$\vec{S} = Tr(\vec{\sigma}\rho) = (2\mathrm{Re}(\psi_1^*\psi_2), 2\mathrm{Im}(\psi_1^*\psi_2), n_2 - n_1) \tag{1.40}$$

this expression can be rewritten as

$$\vec{S} = n(\sqrt{1 - Z^2}\cos\phi, \sqrt{1 - Z^2}\sin\phi, Z) \tag{1.41}$$

defining the relative magnetization $Z(\mathbf{r}) = \frac{n_2(\mathbf{r}) - n_2(\mathbf{r})}{n_2(\mathbf{r}) + n_1(\mathbf{r})}$ and the relative phase between the two components $\phi = \phi_2 - \phi_1$.

Focusing on a one-dimensional case, one can define the 2×2 current-density matrix with elements

$$j_{ab} = \frac{i}{\hbar}[\psi_a \partial_x \psi_b^* - \psi_b \partial_x \psi_a^*] = j_{ba} \tag{1.42}$$

By combining this definition with the GPEs, one obtains the hydrodynamic equations governing both the density and the spin channels.

In the density channel, one recovers the continuity equation for the conservation of the total particle number

$$\dot{n} + \partial_x j_d = 0 \tag{1.43}$$

where $j_d = \mathrm{Tr}(j)$ which is associated with the $U(1)$ symmetry preserved in the density channel.

In the spin channel, the spin current density is defined as

$$\vec{j}_s = \frac{i\hbar}{2m}[(\partial_x \psi^+)\vec{\sigma}\psi - \psi^+(\partial_x \vec{\sigma}\psi)] \tag{1.44}$$

allowing the GPEs to be recast as a hydrodynamic equation for $\vec{S}$ which is formally equivalent to a non dissipative LLE.

$$\dot{\vec{S}} + \partial_x \vec{j}_s = -H(\vec{S}) \times \vec{S} \tag{1.45}$$

Where $H(\vec{S})$ is an effective magnetic field given by

$$\vec{H}(\vec{S}) = (\Omega, 0, \delta + n\Delta + \delta g n Z) \tag{1.46}$$

where $\Delta = \frac{g_{22}-g_{11}}{2\hbar}$ and $\hbar\delta g = \frac{g_{22}+g_{11}}{2} - g_{12}$.

This formulation explicitly shows that the magnetization dynamics of the coupled condensate is formally equivalent to that of a spin system subjected to an external magnetic field, as is discussed in more detail in the following section. In the zero dimensional limit, the current term vanishes since the spatial degrees of freedom are frozen. Experimental realizations of this regime are discussed in [50, 51]. Then, in the low density limit, $n \to 0$, the model reduces to that of a simple two-level atom driven by a coherent external magnetic field $\vec{H} = (\Omega, 0, \delta)$. For finite densities, the spin evolution depends on the spin vector itself through the term $\delta g n$, which introduces a coupling between the spin and the density channels. Furthermore, an imbalance between the two intra-component interaction strength introduces an additional detuning term proportional to the total density, as discussed in [52].

Reduction to 1 Dimension Typical experiments with ultracold atomic gases employ elongated, cigar-shaped samples, realized by harmonic trapping potentials whose frequencies in two directions are much larger than the one along the third direction. In the previous section, the LLE derivation was carried out under the assumption of a strictly one-dimensional condensate. Such an approximation is valid if the radial size of the system is much smaller than the healing length, ensuring that the transverse degrees of freedom are frozen into the Gaussian ground state of the harmonic confinement. However, this condition is extremely challenging to achieve experimentally.

For the purposes of this thesis, a strictly 1D regime is not required for the density degrees of freedom. Instead, it is sufficient to realize an effectively one-dimensional system for spin excitations, as we only focus on internal spin dynamics while neglecting spatial dynamics. This is a less strict request since the spin healing length ξ_s is larger than the density healing length ξ. Thus, when the radial size R_r is smaller than the minimum spatial excitation dictated by ξ_s ($\xi < R_r < \xi_s$) the system supports one-dimensional spin excitations along the axial direction x, provided that $\xi_s < R_x$. In this regime, it is possible to observe and investigate fluctuations and excitations in the spin channel [53, 54, 55]. Under this condition the system is effectively 1D for spin excitations even if it remains three dimensional for density ones. As a consequence, a uniform density profile in the radial direction cannot be assumed, and the transverse inhomogeneity have to be properly taken into account when integrating out the radial degrees of freedom. Following the derivation presented in [56], the dimensional reduction to an effective one-dimensional description leads to a renormalization of the coupling constant, yielding

$$\kappa n(x) = \frac{2}{3}\delta g n^{3D}(r_\perp, x) \tag{1.47}$$

here, the linear density $n(x)$ is given by

$$n(x) = \frac{n_2^{1D}(x)}{n_1^{1D}(x)} = \frac{2}{3} n_0^{3D} \left(1 - \frac{x^2}{R_x^2}\right) \tag{1.48}$$

where we have defined:

$$n_1^{1D}(x) = \int dr_\perp n^{3D}(r_\perp, x) = \frac{\pi R_\perp^2}{3} n_0^{3D} \left(1 - \frac{x^2}{R_x}\right)^2 \tag{1.49}$$

$$n_2^{1D}(x) = \int dr_\perp \left[n^{3D}(r_\perp, x)\right]^2 = \frac{\pi R_\perp^2}{3} (n_0^{3D})^2 \left(1 - \frac{x^2}{R_x}\right)^3 \tag{1.50}$$

Therefore, in the effective one-dimensional regime, the non linear term of the LLE retains the same functional form as in a strictly 1D system with

linear density $n(x)$. The only difference with respect to the ideal 1D case is the renormalization of the interaction strength $\delta g \to \kappa$.

Bloch sphere formalism Both the state of the system and its dynamical evolution can be represented within the Bloch sphere formalism. From the structure of the spinor wave function, one observes that, in principle, it is characterized by four parameters. However, the global phase is physically irrelevant and can be dropped, while the two amplitudes must obey to the normalization conditions $n_1 + n_2 = n$. As a result, the state of the system is completely determined by only two independent parameters. Introducing an angle θ such that the system magnetization can be expressed as $Z = \sin\theta$ the state of the system can be parametrized by two angles (θ, ϕ where $\phi = \phi_2 - \phi_1$ is the relative phase between the two spin components). This parametrization establishes a one-to-one correspondence between the physical state of the system and a point on the unit Bloch sphere. Within this representation, the south pole corresponds to the fully negatively polarized state, in which all atoms occupy the $|1\rangle$ state, while the north pole represents the $Z = +1$ state, where all the atoms are in the $|2\rangle$ state. The equatorial plane describes states with vanishing magnetization, characterized by equal populations in $|1\rangle$ and $|2\rangle$, but different relative phase ϕ.

The coupling between the two spin components can be expressed in terms of an effective magnetic field vector, and the time evolution of the system is then described by the procession of the Bloch state vector around this effective vector accordingly to the LLE.

1.3.4 Paramagnetic-Ferromagnetic Quantum Phase Transition

Phase transitions are characterized by a qualitative change in the macroscopic properties of a system induced by the variation of an external control parameter across a critical point. Above the critical point, the system typically is in a disordered phase, whereas below it enters in an ordered phase. Such changes in the ground-state properties are associated to a symmetry breaking and they are described by a macroscopic order parameter, which vanishes in the disordered phase and acquires a finite value in the ordered one. Phase transitions are classified as first order when the order parameter exhibits a discontinuous jump at the critical point, and as second order when the order parameter vanishes continuously at criticality, while its first derivative becomes discontinuous.

Phase transitions are associated with the divergence of the correlation length at the critical point, meaning that fluctuations develop over all length

and time scales. In this regime, the microscopic details of the Hamiltonian become irrelevant, and the critical exponents governing the divergence of thermodynamic quantities depend only on general features of the system rather than on its macroscopic structure. This allows the identification of universality classes, which are determined solely by the system dimensionality, the number of components of the order parameter, and the range of the interactions. Systems belonging to the same universality class share the same critical behavior.

A distinction can be made between classical and quantum phase transitions. Classical phase transitions occur in systems at finite temperature and are driven by thermal fluctuations, with temperature acting as control parameter. Quantum phase transitions, instead, take place at zero or near zero temperature, where quantum fluctuations dominate, and the critical point is reached by tuning a control parameter different from temperature [57, 7]. A typical example of phase transition is the paramagnetic-to-ferromagnetic phase transition, where the magnetization acts as the order parameter and the system can be described in terms of the Ising model [58]. In its quantum version, the transition arises from the competition between spin-spin interactions and the external transverse magnetic field.

Quantum Phase Transitions can be experimentally investigated in ultracold atomic systems which provide a highly controllable platform for exploring many-body quantum phenomena. Notable examples include the superfluid-to-Mott insulator transition [59], the parity symmetry-breaking transition in cavity-coupled systems [60], and the emergence of a magnetic phase in the spin-orbit coupled spinor gases [61]. In Sec. 1.3.3 showed that the two coupled GPE can be reduced to LLE describing the evolution of the spin dipole interacting with an effective external magnetic field $B_{\text{ext}} = (B_1, B_2, B_3)$ which undergoes a paramagnetic-to ferromagnetic quantum phase transition. We expect the same transition, belonging to the quantum Ising universality class to take place also in such spin mixture, as theoretically predicted in [62] within mean-field theory.

Mean Field Description The ground state of a coherently coupled two-component superfluid can be obtained by minimizing the energy functional. As anticipated in Sec. 1.3.2. in the presence of coherent coupling, for the ground state, the relative phase between the two components is locked to zero, so that the energy functional depends only on the system magnetization Z. It can be written as

$$E(Z) = -\left[\frac{1}{2}\kappa n Z^2 + \Omega_R\sqrt{1-Z^2} + (\delta - n\Delta)Z\right] \tag{1.51}$$

We focus on the case $\kappa < 0$, corresponding to a mixture with immiscible character in the absence of coherent coupling. The competition between interaction energy and coherent coupling is governed by the dimensionless ratio $|\kappa|n/\Omega_R$.

For the zero detuning case ($\delta - n\Delta = 0$), two regimes can be identified (Fig. 1.2). When $|\kappa|n \ll \Omega_R$, meaning that the coherent coupling dominates over interactions, the energy functional has a single minimum at $Z = 0$, corresponding to a paramagnetic phase in which, in general, the system undergoes simple Rabi oscillations with period $2\pi/\Omega_R$. In contrast, for $|\kappa|n \gg \Omega_R$, the energy develops two symmetric degenerate minima at

$$Z = \pm\sqrt{1 - \left(\frac{\Omega_R}{\kappa n}\right)^2} \tag{1.52}$$

In this case, the phase-space trajectories are distorted, and at lowest energies, the system is trapped in one of the two minima, corresponding to a ferromagnetic phase with finite magnetization. The transition from a single-well to a double-well energy landscape signals a second order quantum-phase transition.

In the presence of finite detuning, the behavior of the system depends on the phase. In the paramagnetic regime, the unique minimum of the energy functional is shifted to a finite Z, with the sign determined by the detuning. In the ferromagnetic phase, the degeneracy between the two minima is removed, one minimum becomes energetically favored over the other, again accordingly to the sign of the detuning, leading to metastable state and hysteresis. As a consequence, sweeping the detuning across zero at fixed $|\kappa|n/\Omega_R > 1$ induces a first order phase transition, characterized by a discontinuous jump of the magnetization. Increasing the magnitude of δ, the imbalance between the two minima grows, and above a critical field the metastable minimum disappears, corresponding to the saturated ferromagnetic phase.

Magnetic System A closely related description arises in a magnetic system described by a local spin vector $\vec{S} = (S_1, S_2, S_3)$, subject to spin-spin interactions (parametrized by the coupling constant K) and an external magnetic field $\vec{B}$ setting a preferential direction for the spin alignment.

At zero temperature, such a system is predicted to undergo a transverse-field Ising quantum phase transition [7].

A continuous version of the model is obtained by integrating the Ising Hamiltonian [63], leading to the following energy functional:

$$E(\vec{S}) \propto -\int \vec{B}\cdot\vec{S} - \frac{1}{2}\vec{S}\cdot\vec{K}\cdot\vec{S} - \frac{1}{2}|\nabla\vec{S}|^2 dV \tag{1.53}$$

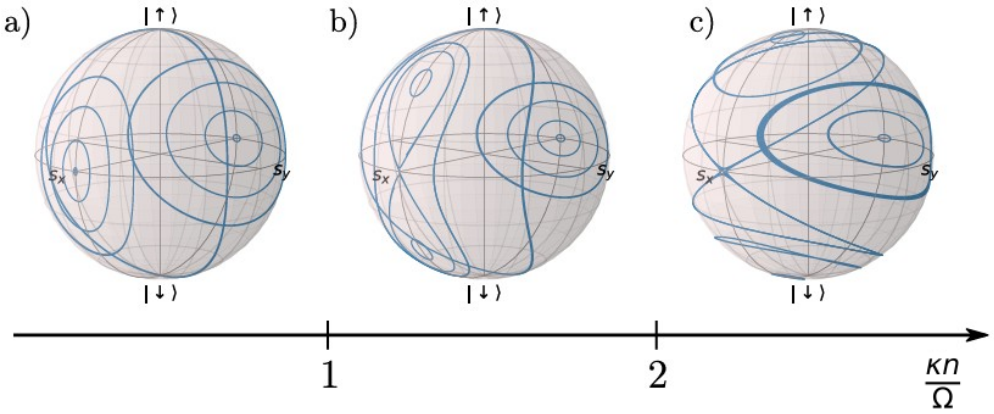

Figure 1.2: Spin vector orbits on the Bloch Sphere in the zero detuning case for different values of the dimensionless ratio $|\kappa|n/\Omega_R$, for $\kappa n < 0$ case. (a) $|\kappa|n/\Omega_R = 2/3$, (b) $|\kappa|n/\Omega_R = 4/3$, (c) $|\kappa|n/\Omega_R = 4$.

This functional contains three contributions. The first term describes the dipole interactions $\vec{\mu}\cdot\vec{B}$, favoring alignment of the spin with the external magnetic field. The second term accounts for anisotropic spin-spin interactions and determines the preferred self-alignment direction of the spins in the absence of a magnetic field, defining the so-called easy axis. The last term is the energetic cost due to the formation of magnetic domains arising from exchange energy between neighboring spins.

Neglecting dissipative effects, the dynamics of the system are governed by the Landau-Lifshitz equation (LLE) [48],

$$\partial_t \vec{S} = -\vec{H}_{\text{eff}} \times \vec{S} \tag{1.54}$$

where the effective magnetic field is defined as $H_{\text{eff}} = -\frac{\partial E}{\partial S}$.

To establish a connection with the atomic platform considered in this work, we focus on a system with fixed spin density $n = |\vec{S}|$, unaxial magnetic anisotropy, and an external magnetic field with both transverse and longitudinal components. In particular, we assume that the only non vanishing element of the anisotropy tensor is $K_{33} = \alpha < 0$, and that the magnetic field takes the form $\vec{B} = (B_1, 0, B_3)$, where B_1 is the transverse field while B_3 is the longitudinal field. Under these conditions, the effective field becomes

$$\vec{H}_{\text{eff}} = (B_1, 0, B_3 - \alpha S_3) \tag{1.55}$$

By introducing the relative magnetization $Z = S_3/n$ and the azimuthal

angle of the spin in the transverse plane, $\phi = \arctan(S_2/S_1)$, the state of the system is fully specified by these two variables. In terms of these parameters, the energy functional reduces to

$$E(Z,\phi) \propto -B_3 Z - \frac{|\alpha|n}{2} Z^2 - B_1\sqrt{1-Z^2}\cos\phi \tag{1.56}$$

For $B_1 > 0$, the minimum occurs at $\phi = 0$, reducing the problem to one dimensional minimization with respect to Z, and the ground state of the system is fully determined by the two dimensionless parameters B_3/B_1 and $|\alpha|n/B_1$.

The phase diagram of the system is represented in the central panel of Fig. 1.3, while the (A)-(H) panels show the energy profiles as a function of Z for representative points in parameter space. At $B_3 = 0$ (in the absence of longitudinal field) , a second order phase transition occurs at $|\alpha|n/B_1 = 1$, separating a paramagnetic phase with a single minimum at $Z = 0$ ($|\alpha|n/B_1 < 1$) from an ordered ferromagnetic phase with two degenerate minima at $\pm Z \neq 0$ ($|\alpha|n/B_1 > 1$). The magnetization of the ground state as a function of $|\alpha|n/B_1$ is shown in the bottom panel of Fig. 1.3. A finite longitudinal field shifts the single minimum of the paramagnetic phase to finite values of Z (as shown in the left panel of Fig. 1.3) while in the ferromagnetic phase lifts the degeneracy, giving rise to metastability, hysteresis and eventually to saturated ferromagnetic phase (as shown in the right panel of Fig. 1.3).

Atomic System The analogy between the two systems allows for a direct mapping between the coherently-coupled superfluid mixture and the magnetic model. The correspondence between the two systems is summarized in Tab. 1.1:

In this mapping, the longitudinal spin component $S_3 = n_\uparrow - n_\downarrow$, plays the role of the magnetization, while the transverse components S_1 and S_2 are associated with the intercomponent coherence. The transverse and the lon-

	Magnetic System	Atomic System
Anisotropic Interactions	αn	κn
Axial field	B_3	$\delta_{\text{eff}} = \delta_B + n\Delta$
Transverse field	B_1	Ω_{R}
Spin States	$\|\uparrow\rangle$	$\|2,-2\rangle$
	$\|\downarrow\rangle$	$\|1,-1\rangle$
Magnetization	$\mathbf{S}(\|\mathbf{S}\| = n)$	
Relative Magnetization	$Z = S_3/n$	

Table 1.1: Mapping between magnetic and atomic system.

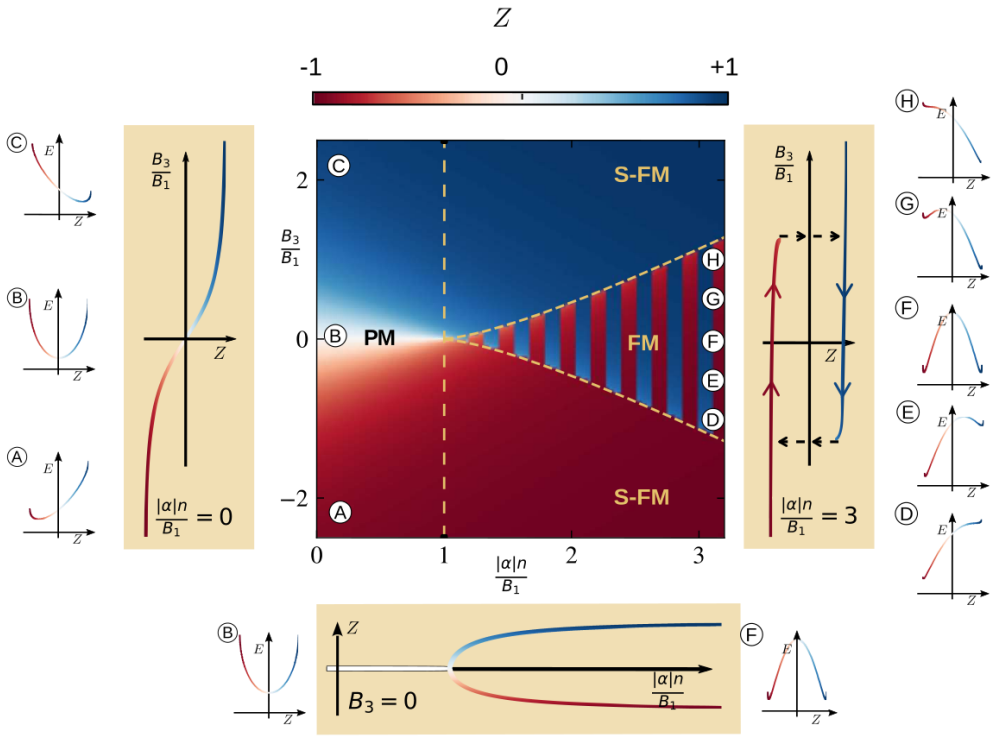

Figure 1.3: Phase diagram of the magnetic model. It shows the relative magnetization Z of the stationary states as a function of the longitudinal magnetic field strength and of the non linearity, both in units of the transverse field. Three phases can be recognized: the paramagnetic phase when $|\alpha|n < B_1$, the ferromagnetic phase if $|\alpha|n > B_1 \gg B_3$ and the saturated ferromagnetic phase if $|\alpha|n > B_1$ and $B_3 \gg B_1$. The panels (A)-(H) show the energy dependence on the relative magnetization Z in different points of the phase diagram. The three orange panels show the value of the magnetization at the energy minimum as a function of $|\alpha|n/B_1$ for $B_3 = 0$ (bottom), as a function of B_3/B_1 for $|\alpha|n/B_1$ (left) or $|\alpha|n/B_1 = 3$ (right)

gitudinal magnetic fields of the spin model are identified, respectively, with the Rabi frequency Ω_R and with the effective detuning δ of the coherent coupling. The detuning is defined as $\delta = \omega - \omega_0$, where ω is the frequency of the coupling field and ω_0 is the energy splitting between the two internal atomic states, including the linear Zeeman shift.

Spin-spin interactions in the magnetic model correspond, in the atomic system, to the difference between intra- and inter-component mean field in-

teraction energies. This contribution is quantified by the effective interaction strength κn, which plays the role of an anisotropic magnetic interaction along the longitudinal (S_3) direction.

Within this framework, the bifurcation of the system magnetization $Z = S_3/n$ at $\Omega_R = |\kappa|n$, with n the total density can be interpreted as a quantum phase transition. In the ferromagnetic phase, the magnetization grows as $Z \sim [-(\kappa n + \Omega_R)]^\beta$ with the typical mean field critical exponent $\beta = 1/2$ [62].

Finally, we recall that an imbalance between the two intercomponent interaction strengths induces an additional correction to the mean-field energy. Even for equal component densities, the two chemical potentials differ, leading to unequal energy shifts on the two atomic states coupled by the radiation field. As a result, the interaction-induced energy difference $n\Delta \propto n(g_{\downarrow\downarrow} - g_{\uparrow\uparrow})/\hbar$ must be compensated to achieve resonance. This motivates the definition of an effective detuning $\delta_{\text{eff}} = \delta_B + n\Delta$ which incorporates both the bare detuning δ_B and the density dependent collisional shift.

1.4 Spin-1 BEC

In spinor Bose Einstein condensates, interactions between atoms occupying different internal spin states give rise to a rich variety of magnetic phases. Remarkably, such phases can emerge even when the spin-dependent interactions are weak, due to the bosonic enhancement associated with condensation. As a consequence, spinor gases exhibit magnetic ordering below the condensation threshold. In particular, the interplay between spin-dependent interactions and the coupling to an external magnetic field can drive quantum phase transitions between distinct magnetic phases.

1.4.1 Graphical representation

To introduce the description of the spin 1 condensate, it can be useful to briefly recall the simpler case of a $S = 1/2$ system. A generic $S = 1/2$ state can be described by a two component spinorial wave function

$$\Psi_{1/2} = e^{i\theta} \begin{pmatrix} \sqrt{N_{+1/2}} e^{i\phi_L/2} \\ \sqrt{N_{-1/2}} e^{-i\phi_L/2} \end{pmatrix} \tag{1.57}$$

where $\phi_L = \phi_{+1/2} - \phi_{-1/2}$ is the relative phase between the two spin components, while θ is a global phase which can be dropped. The normalization condition $N_{1/2} + N_{-1/2} = 1$ implies that only two independent parameters are required to specify the state of the system. As a result, any $S = 1/2$ state can

be represented as a point on the Bloch sphere as already shown in the previous section.

Within this framework, any unitary transformation of the state corresponds to a rotation on the Bloch sphere and is described by the Lie Group $SU(2)$. Choosing the z-axis as the quantization direction, one introduces three Hermitian unitary operators: the Pauli matrices

$$\hat{\sigma}_x = \begin{pmatrix} 0 & 1 \\ 1 & 0 \end{pmatrix}, \quad \hat{\sigma}_y = \begin{pmatrix} 0 & -i \\ i & 0 \end{pmatrix}, \quad \hat{\sigma}_z = \begin{pmatrix} 1 & 0 \\ 0 & -1 \end{pmatrix} \tag{1.58}$$

The spin operators $\hat{S}_i = \hat{\sigma}_i/2$ with $i = x, y, z$ satisfy the Lie algebra

$$[S_i, S_j] = i\epsilon_{i,j,k} S_k \tag{1.59}$$

and act as the generators of $SU(2)$. Any rotation can therefore be written as $U = e^{-i\sum_{i=x,y,z} r_i S_i}$ and any state of the system is completely determined by the expectation values of these operators.

The situation is more involved for a $S = 1$ particle. In this case the quantum state is described by a three-component spinor wavefunction

$$|\Psi\rangle = r_{+1}e^{i\phi_L/2}|{+1}\rangle + r_0 e^{i\phi_S}|0\rangle + r_{-1}e^{-i\phi_L/2}|{-1}\rangle = \begin{pmatrix} r_{+1}e^{i\phi_L/2} \\ r_0 e^{i\phi_S} \\ r_{-1}e^{-i\phi_L/2} \end{pmatrix} \tag{1.60}$$

where $\phi_L = \phi_{+1} - \phi_{-1}$ and $\phi_S = \phi_0 - \frac{\phi_1+\phi_{-1}}{2}$ are the relative phases. As in the previous case the global phase can be dropped and the normalization condition $N_{+1}+N_0+N_{-1} = 1$ fixes one of the amplitudes. The state is therefore specified by four independent parameters resulting in a larger set of possible operations captured by the Lie Group $SU(3)$, which requires eight independent Hermitian generators.

Although three spin operators, satisfying the $SU(2)$ commutation rules, can still be defined for a $S = 1$ system,

$$\hat{S}_x = \frac{1}{\sqrt{2}}\begin{pmatrix} 0 & 1 & 0 \\ 1 & 0 & 1 \\ 0 & 1 & 0 \end{pmatrix}, \quad \hat{S}_y = \frac{i}{\sqrt{2}}\begin{pmatrix} 0 & -1 & 0 \\ 1 & 0 & -1 \\ 0 & 1 & 0 \end{pmatrix}, \quad \hat{S}_z = \begin{pmatrix} 1 & 0 & 0 \\ 0 & 0 & 0 \\ 0 & 0 & -1 \end{pmatrix} \tag{1.61}$$

their expectation values are not sufficient to fully characterize the state of the system since these operators do not form a complete basis for $SU(3)$.

A complete description is obtained by introducing the quadrupole operators defined in [64, 65]

$$\hat{Q}_{ij} = \hat{S}_i\hat{S}_j + \hat{S}_j\hat{S}_i - \frac{4}{3}\delta_{ij}\mathbb{I}_3 \tag{1.62}$$

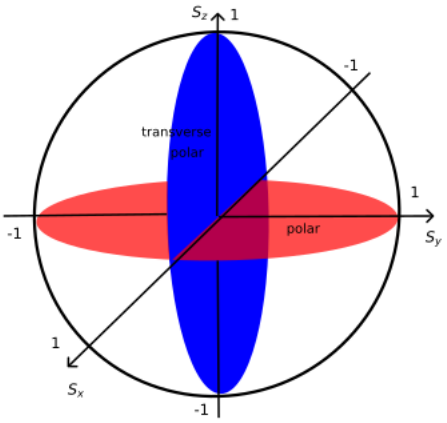

Figure 1.4: Representation of the ellipsoids centered around the expectation value and indicating the fluctuation planes of the polar state (red) and of the transverse polar state (blue).

whose expectation value quantifies spin fluctuations. The $\{\hat{S}_i, \hat{Q}_{ij}\}$ completely describe the system which is therefore determined by both the mean spin components $\langle \hat{S}_i \rangle$ and their fluctuations in the three directions

$$\Delta S_i = \sqrt{\langle \hat{S}_i \rangle^2 - \langle \hat{S}_i^2 \rangle} \tag{1.63}$$

Example A typical example illustrating the insufficiency of the spin operators alone in characterizing the state of the system is provided by the polar state $|0\rangle$ and the transverse polar state $|\Psi_{\mathrm{TP}}\rangle = \frac{1}{\sqrt{2}}(|+1\rangle - |-1\rangle)$. For both states, the expectation values of the spin operators vanish

$$\langle 0| \hat{S}_i |0\rangle = \langle \Psi_{TP}| \hat{S}_i |\Psi_{TP}\rangle = 0 \tag{1.64}$$

for $i = x, y, z$, while they differ in the expectation value of the quadrupolar operator $\hat{Q}_{zz}$. Consequently, a graphical representation based only on points on the Bloch sphere is inadequate. Instead, the state can be well represented by an ellipsoid centered at the spin expectation value, whose orientation and shape encode the direction and magnitude of spin fluctuations. For the polar state the ellipsoid lies in the S_x-S_y plane, whereas for the transverse polar state it lies in the S_z-S_x plane, as shown in Fig. 1.4. In this sense, the plane of maximal fluctuations, which is perpendicular to the state direction, completely specifies the orientation of the state. These states are eigenstates of the quadrupole operators.

1.4.2 Internal degrees of freedom and relevant energy scales

The internal structure of alkali atoms is characterized by a hierarchy of energy scales. At the electronic level, the fine structure originates from the spin–orbit coupling between the electronic spin **S** and the orbital angular momentum **L**, lifting the degeneracy between states with different total electronic angular momentum $\mathbf{J} = \mathbf{L} + \mathbf{S}$.

At lower energies, each fine-structure level is further split by the hyperfine interaction, which arises from the magnetic coupling between the electronic angular momentum and the nuclear spin **I**. The resulting eigenstates are labeled by the total angular momentum $\mathbf{F} = \mathbf{J} + \mathbf{I}$. In the absence of external magnetic fields, a hyperfine manifold with total angular momentum F consists of $2F+1$ degenerate Zeeman sublevels labeled by the magnetic quantum number m_F. For sodium atoms, the electronic ground state is $3^2S_{1/2}$ characterized by orbital angular momentum $L = 0$ and total electronic angular momentum $J = 1/2$. The first excited states belong to $3^2P_{1/2}$ and $3^3P_{3/2}$, with $L = 1$ and $J = 1/2$ and $J = 3/2$ respectively. Since the nuclear spin of sodium is $I = 3/2$, the $J = 1/2$ levels split into $F = 1$ and $F = 2$, while $J = 3/2$ is split in $F = 1, 2, 3$.

1.4.3 Zeeman effect and low-field expansion

In the presence of a finite magnetic field defining a quantization axis, the degeneracy of the Zeeman sublevels is removed. The corresponding energy shifts are described by the Breit-Rabi formula [66, 67] which holds for $J = 1/2$ resulting in $F = I \pm 1/2$

$$E_{F=I\pm1/2} = -\frac{\Delta E_{\text{hfs}}}{2(2I+1)} + \mu_N g_I m_F B \pm \frac{\Delta E_{\text{hfs}}}{2}\sqrt{1 + \frac{2m_F x}{I+1/2} + x^2} \qquad (1.65)$$

where $x = (\mu_B g_J - \mu_N g_I)B/\Delta E_{\text{hfs}}$, ΔE_{hfs} is the hyperfine energy shift, μ_N is the nuclear magneton, μ_B is the Bohr magneton, g_I is the nuclear Landé factor and g_J is the electronic Landé factor and B is the magnetic field.

For magnetic fields sufficiently weak (typically up to a few gauss) the Zeeman energy is much smaller than the hyperfine splitting. Under this condition, the Breit-Rabi formula can be expanded up to second order in the magnetic field. Moreover, the nuclear Landé factor can be neglected in comparison with respect to the electronic one. Within these approximations, a simplified expression for the hyperfine energies is obtained:

$$E_{F=I\pm1/2} = -\frac{1}{8}\Delta E_{\text{hfs}} + \frac{1}{2}\Delta E_{\text{hfs}} + \mu_B g_F m_F B \pm \frac{\mu_B^2 g_F^2 m_F^2}{\Delta E_{\text{hfs}}} B^2 \mp \frac{(2I+1)^2 \mu_B^2 g_F^2}{4\Delta E_{\text{hfs}}} \tag{1.66}$$

here, the first term represents a global energy offset, while the second corresponds to the hyperfine splitting. The third term describes the linear Zeeman shift, proportional to the magnetic field B and to m_F. The fourth term accounts for the quadratic Zeeman contribution, scaling as B^2 and explicitly depending on m_F^2. The last term is a magnetic-field-dependent but m_F-independent correction; therefore, it produces a common shift of all Zeeman sublevels within a given hyperfine manifold and does not affect their relative spacing.

For sodium atoms, having nuclear spin $I = 3/2$, the sublevels energies in the $F = 1$ manifold can be written in a compact form

$$E_{m_F} = m_F p + m_F^2 q \tag{1.67}$$

where $p = g_F \mu_B B$ is the linear Zeeman coefficient and $q = \frac{(g_F \mu_B B)^2}{\Delta E_{hfs}}$ is the quadratic Zeeman coefficient. For the hyperfine manifold considered here, $g_F = -1/2$.

1.4.4 Two-body interactions in $F = 1$ Bose Gases

As discussed above, collisions in ultracold and dilute atomic gases are dominated by low-energy s-wave scattering. Within the weak-coupling approximation, the orbital and internal degrees of freedom do not couple during the collision process, implying conservation of the total spin of the colliding pair. For $F = 1$ bosons, symmetry constraints restrict the allowed scattering channel to total spin $\mathbf{F} = 0$ and $\mathbf{F} = 2$.

Under these conditions, the interaction can be modeled by a Fermi contact potential of the form

$$\hat{V} = \delta(\mathbf{r}_1 - \mathbf{r}_2) \times \sum_{\mathbf{F}=0,2} \frac{4\pi\hbar^2 a_{\mathbf{F}}}{m} \hat{P}_{\mathbf{F}} \tag{1.68}$$

where $a_{\mathbf{F}}$ denotes the s-wave scattering lengths in the total spin $\mathbf{F}$ channel and $\hat{P}_{\mathbf{F}}$ is the corresponding projector operator.

It is convenient to reformulate the interaction in terms of spin operators [18]. To this end, we first consider the squared total spin of the two-atom system,

$$(\hat{S}_1 + \hat{S}_2)^2 = \hat{S}_1^2 + \hat{S}_2^2 + 2\hat{S}_1 \cdot \hat{S}_2 = \sum_{\mathbf{F}} \mathbf{F}(\mathbf{F}+1)\hat{P}_{\mathbf{F}} \tag{1.69}$$

Since only the $\mathbf{F} = 0$ and $\mathbf{F} = 2$ channels are allowed, one obtains

$$\sum_{\mathbf{F}} \mathbf{F}(\mathbf{F}+1)\hat{P}_{\mathbf{F}} = 6\hat{P}_2 \tag{1.70}$$

Introducing the identity operators $\hat{I}_1$ and $\hat{I}_2$ in the internal Hilbert spaces of particles 1 and 2, and using

$$\hat{I}_1 \times \hat{I}_2 = \hat{P}_0 + \hat{P}_2 \tag{1.71}$$

the projector can be expressed as

$$\hat{P}_0 = \frac{\hat{I}_1 \times \hat{I}_2 - \hat{S}_1 \cdot \hat{S}_2}{3} \quad \hat{P}_2 = \frac{2\hat{I}_1 \times I_2 + \hat{S}_1 \cdot \hat{S}_2}{3} \tag{1.72}$$

Substituting (1.72) into (1.68) leads to a compact representation of the spin-dependent two-body interaction,

$$\hat{V} = c_0 \hat{I}_1 \times \hat{I}_2 + c_2 \hat{S}_1 \times \hat{S}_2 \tag{1.73}$$

here, $c_0 = \frac{4\pi\hbar^2}{m}\bar{a}$ is the spin independent interaction constant with $\bar{a} = \frac{a_0+2a_2}{3}$ and $c_2 = \frac{4\pi\hbar^2}{m}a_s$ is the spin dependent interaction constant with $a_s = \frac{a_2-a_0}{3}$ [68]. The sign of c_2 determines whether the system exhibits ferromagnetic or antiferromagnetic interactions.

For $F = 1$ sodium the accurate values of the scattering lengths are determined in [69] and result to be $\bar{a} \approx 2.79(2)$ nm $a_S \approx 0.1(2)$ nm resulting in an antiferromagnetic material. Moreover, the ratio $\frac{a_S}{\bar{a}} = 0.036$ [42] indicates that the spin-dependent interaction strength is much smaller than the spin independent one.

1.4.5 Many-body Interaction Hamiltonian

Within the second quantization framework, the interaction Hamiltonian of a $F = 1$ spinor condensate can be decomposed into a spin-independent and a spin-dependent contributions,

$$\hat{H}_{\text{int}} = \hat{H} + \hat{H}_{\text{s}} \tag{1.74}$$

with

$$\hat{H} = \frac{c_0}{2} \sum_{ij} \int d\mathbf{r} \psi_i^+(\mathbf{r}) \psi_j^+(\mathbf{r}) \psi_i(\mathbf{r}) \psi_j(\mathbf{r}) \tag{1.75}$$

	$m_F=+1$	$m_F=0$	$m_F=-1$
$m_F=+1$	a_2	a_2	$(a_2+2a_0)/3$
$m_F=0$	a_2	$(2a_2+a_0)/3$	a_2
$m_F=+1$	$(a_2+2a_0)/3$	a_2	a_2

Table 1.2: Scattering lengths in the $F=1$ spinor condensates.

$$\hat{H}_{\rm s}=\frac{c_2}{2}\sum_{ijkl}\int d\mathbf{r}S_{ik}S_{jl}\psi_i^+(\mathbf{r})\psi_j^+(\mathbf{r})\psi_k(\mathbf{r})\psi_l(\mathbf{r}) \tag{1.76}$$

here $\hat{\psi}_i^\dagger(\mathbf{r})$ creates a particle at position $\mathbf{r}$ in the Zeeman state $|F=1,m_F=i\rangle$, while S_{ij} denotes the (i,j) components of the spin-1 operator $\hat{S}$ such that $S_{ij}=((S_x)_{ij},(S_y)_{ij},(S_z)_{ij})^T$ with $\hat{S}_x,\hat{S}_y,\hat{S}_z$ defined in Sec. 1.4.1. Carrying out the summations yields the explicit form of the interaction Hamiltonian, consisting in density-density (elastic terms) and spin-exchange (inelastic) contributions.

$$\begin{aligned}\hat{H}_{\rm int}=\frac{1}{2}\int d\mathbf{r}&(c_0+c_2)\psi_+^+(\mathbf{r})\psi_+^+(\mathbf{r})\psi_+(\mathbf{r})\psi_+(\mathbf{r})+c_0\psi_0^+(\mathbf{r})\psi_0^+(\mathbf{r})\psi_0(\mathbf{r})\psi_0(\mathbf{r})+\\ &2(c_0+c_2)\psi_+^+(\mathbf{r})\psi_0^+(\mathbf{r})\psi_+(\mathbf{r})\psi_0(\mathbf{r})+(c_0+c_2)\psi_-^+(\mathbf{r})\psi_0^+(\mathbf{r})\psi_-(\mathbf{r})\psi_0(\mathbf{r})+\\ &(c_0-c_2)\psi_+^+(\mathbf{r})\psi_-^+(\mathbf{r})\psi_+(\mathbf{r})\psi_-(\mathbf{r})+\\ &c_2(\psi_+^+(\mathbf{r})\psi_-^+(\mathbf{r})\psi_0(\mathbf{r})\psi_0(\mathbf{r})+(\psi_0^+(\mathbf{r})\psi_0^+(\mathbf{r})\psi_+(\mathbf{r})\psi_-(\mathbf{r}))\end{aligned} \tag{1.77}$$

the first five terms (three rows) correspond to elastic collisions and results in mean-field energy shifts of the Zeeman components. The last two terms describe spin-changing collisions of the form $|1,+1\rangle|1,-1\rangle\leftrightarrow|1,0\rangle|1,0\rangle$ which are the only allowed spin changing collisions. These processes conserve the longitudinal magnetization, defined as the population difference between the $|m_F=+1\rangle$ and $|m_F=-1\rangle$ states. Conservation of longitudinal magnetization is a fundamental symmetry of the system and underlies many observable effects associated with spin-dependent interactions. The spin-dependent interaction also determines the miscibility properties of the Zeeman components. Moreover, by comparing Eq. 1.77 with the interaction energy obtained integrating Eq. 1.20 and expressing the coupling constant in terms of the scattering lengths a_0 and a_2, one obtains the effective inter- and intra-component scattering lengths for the $F=1$ manifold (which are reported in Tab. 1.2).

For sodium, the miscibility condition discussed in Sec. 1.2.3, implies that the $|m_F=\pm1\rangle$ are mutually miscible, whereas each of them is immiscible with the $|m_F=0\rangle$ state.

1.4.6 Competition Between Magnetic Field and Spin-Dependent Interactions

For a typical BEC of ^{23}Na with density of about 10^{20} atoms/m^3, the mean-field spin interaction energy is of the order of $h \times 1$ kHz. This energy scale is much smaller than linear energy shift produced even by very weak magnetic fields. Consequently, when the magnetization is free to evolve Zeeman energy always dominates over the spin interaction energy and the system minimizes its energy by populating the Zeeman sublevel with the lowest linear Zeeman energy.

However, as already discussed in Sec. 1.4.5, the longitudinal magnetization is conserved and the linear Zeeman term is fixed, hence it provides an overall energy offset which does not affect the ground state properties and it can be dropped from the Hamiltonian. Then the magnetic field contribution is given only by the smaller quadratic Zeeman term.

Since the quadratic Zeeman coefficient q is positive in $F = 1$ sodium atoms, the $|m_F = \pm 1\rangle$ states are shifted upward in energy, while $|m_F = 0\rangle$ is energetically favored. The effects of the linear and quadratic Zeeman contributions are shown in Fig. 1.5 in the left and right panel, respectively. The energy scales of the two plots are different since the quadratic Zeeman shift is much smaller than the linear one.

By arbitrarily taking one of the two $|m_F = \pm 1\rangle$ states as the reference level for the quadratic Zeeman energy shift, the Zeeman contribution to the Hamiltonian can be expressed as

$$H_{\mathrm{ZE}} = -q\hat{N}_0 \tag{1.78}$$

here $\hat{N}_0$ is the number operator of the $|m_F = 0\rangle$ state. This term breaks the rotational symmetry of the Hamiltonian by selecting the quantization axis defined by the external magnetic field direction.

1.4.7 Mean field theory and single mode approximation

In the previous sections, two competing contributions to the energy of a $F = 1$ Bose Einstein Condensate have been identified: the spin-dependent interaction energy and the Zeeman energy associated with an external magnetic field. The interplay between these terms determines the ground state properties of the system. In order to obtain an analytic description of the ground state, it is convenient to introduce two widely used approximations: the mean-field approximation (MFA) and the single-mode approximation (SMA).

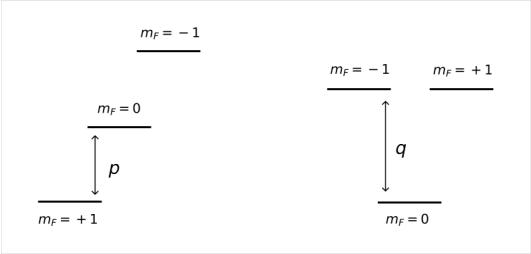

Figure 1.5: Effects of the linear (left) and quadratic (right) Zeeman shifts induced by a homogeneous external magnetic field on the $F = 1$ manifold. The two contributions are shown on different energy scales, since the linear Zeeman coefficient p is much larger than the quadratic Zeeman coefficient q.

Mean field Approximation Within the mean field framework, quantum fluctuations are neglected and field operators are replaced by their expectation values. All atoms are assumed to occupy the same single-particle state

$$\phi = (\phi_{+1}, \phi_0, \phi_{-1})^T, \tag{1.79}$$

so that the many-body wavefunction of an N-particle system can be written as

$$|\Psi\rangle_N = \frac{1}{N!}(a_\phi^\dagger)^N |0\rangle \tag{1.80}$$

where $a_\phi^\dagger$ creates a particle in the single particle state ϕ.

By evaluating the expectation value of the total Hamiltonian on this state, the total energy functional reads

$$\begin{aligned} E_{\text{tot}} = \sum_i \frac{\hbar^2}{2m} \int |\nabla \phi_i|^2 + \int V_{\text{ext}} |\phi_i|^2 + \frac{c_0}{2} \int |\phi_i|^4 \\ + \frac{c_2}{2} \int (|\phi_+|^2 - |\phi_-|^2)^2 + 2|\phi_0|^2(|\phi_+|^2 + |\phi_-|^2) + 2(\phi_0^2 \phi_+^* \phi_-^* + cc) \\ + \sum_{m_F} E_i \int |\phi_i|^2 \end{aligned} \tag{1.81}$$

The first line is the spin-independent contribution, the second line the spin-dependent interaction energy, and the last term the Zeeman energy.

The ground state is obtained by minimizing the functional

$$E_{\text{tot}} - \mu\langle N \rangle - \eta\langle S_z \rangle, \tag{1.82}$$

where μ and η are the Lagrange multipliers enforcing conservation of the total number of particles and magnetization, respectively. The procedure yields three coupled Gross-Pitaevskii equations:

$$(\mu+\eta)\phi_{+1} = (H + E_{+1} + c_2(n_{+1} + n_0 - n_{-1}))\phi_{+1} + c_2\phi_0^2\phi_{-1}^* \tag{1.83}$$

$$\mu\phi_0 = (H + E_0 + c_2(n_{+1} + n_{-1}))\phi_0 + 2c_2\phi_0^*\phi_{+1}\phi_{-1} \tag{1.84}$$

$$(\mu-\eta)\phi_{-1} = (H + E_{-1} + c_2(n_{-1} + n_0 - n_{+1}))\phi_{-1} + c_2\phi_0^2\phi_{+1}^* \tag{1.85}$$

with

$$H = -\frac{\hbar^2\nabla^2}{2m} + V_{\text{ext}}(\mathbf{r}) + c_0 n_{\text{tot}} \tag{1.86}$$

The spin-exchange terms are responsible for the redistribution of population among the three Zeeman components while preserving the total magnetization.

Single Mode Approximation In the presence of a magnetic field, the spin-dependent part of the Hamiltonian can be written as

$$\hat{H}_{\text{s}} = \frac{c_2}{2}\int d\mathbf{r}\hat{S}^2(\mathbf{r}) - q\hat{N}_0 \tag{1.87}$$

which couples the orbital and internal degrees of freedom. This coupling makes very difficult to compute the exact ground state of the system. The single mode approximation provides a substantial simplification by assuming that all spin components share the same spatial wavefunction reducing the problem to a purely spin problem.

$$\psi(\mathbf{r}) \propto \phi_+(\mathbf{r}) \propto \phi_0(\mathbf{r}) \propto \phi_-(\mathbf{r}) \tag{1.88}$$

the common mode $\psi(\mathbf{r})$ satisfies the spin-independent GPE:

$$\left(-\frac{\hbar^2\nabla^2}{2m} + V_{\text{ext}}(\mathbf{r}) + c_0 N|\psi(\mathbf{r})|^2\right)\psi(\mathbf{r}) = \mu\psi(\mathbf{r}) \tag{1.89}$$

Under this approximation, orbital and internal degrees of freedom are decoupled, and all the ground state properties are determined by the minimization of the spin-dependent energy

$$\hat{H}_{\text{s}} = \frac{\tilde{c_2}}{2N}\hat{S}^2 - q\hat{N}_0 \tag{1.90}$$

where

$$\tilde{c_2} = Nc_2\int d\bar{r}|\psi(\bar{r})|^4 \tag{1.91}$$

In the antiferromagnetic case ($c_2 > 0$), the interaction term favors states with minimal total spin, while the quadratic Zeeman effect favors the occupation of $|m_F = 0\rangle$ state, under the constraint that total magnetization is conserved.

Mean-field theory within the single-mode approximation Combining the MFA with the SMA, the single particle wavefunction can be factorized as

$$|\phi(\mathbf{r})\rangle = \psi(\mathbf{r})\,|\xi\rangle\,, \tag{1.92}$$

where $|\xi\rangle$ describes the spin degree of freedom. In the standard basis,

$$|\xi\rangle = \begin{pmatrix} \sqrt{n_{+1}}e^{i\theta_{+1}} \\ \sqrt{n_0}e^{i\theta_0} \\ \sqrt{n_{-1}}e^{i\theta_{-1}} \end{pmatrix} \tag{1.93}$$

Using normalization and removing the global phase, the spinor can be parametrized by four real variables:

$$x = n_{+1}+n_{-1}, \qquad m_z = n_{+1}-n_{-1}, \qquad \Theta = \theta_{+1}+\theta_{-1}-2\theta_0, \qquad \alpha = \theta_{+1}-\theta_{-1} \tag{1.94}$$

with $0 \leq x \leq 1$ imposed by the state normalization and $|m_z| \leq x$. The spinor wave function takes the form

$$|\xi\rangle = \begin{pmatrix} \sqrt{(x+m_z)/2}e^{i(\theta+\alpha)/2} \\ \sqrt{1-x} \\ \sqrt{(x-m_z)/2}e^{i(\theta-\alpha)/2} \end{pmatrix} \tag{1.95}$$

Substituting this expression into the mean-field Hamiltonian gives the spin energy per particle [18]:

$$\frac{E_{\text{spin}}}{N\tilde{c}_2} = \frac{1}{2}\left(m_z^2 + 2x(1-x) + 2\cos\theta(1-x)\sqrt{x^2-m_z^2}\right) + \tilde{q}x, \qquad \tilde{q} = \frac{q}{\tilde{c}_2} \tag{1.96}$$

For fixed magnetization m_z and quadratic Zeeman shift $\tilde{q}$, the energy minimization depends on the two free parameters x and θ. In the antiferromagnetic case ($\tilde{c}_2 > 0$), the energy is always minimized for $\theta = \pi$, and the ground state is determined by minimizing the energy with respect to x.

Phase transition The ground state of a spin-1 condensate within the mean-field and single mode approximation is determined by minimizing the spin energy as function of quadratic Zeeman shift q, under the constraint of fixed magnetization m_z. The analysis shows the occurrence of a quantum phase transition in the occupation number of the $|m_F = 0\rangle$ state, with the magnetic field magnitude as control parameter.

We first consider the simplest situation of vanishing longitudinal magnetization. In this case the spin energy functional takes the simple form

$$E_{\mathrm{s}} = Nqx \tag{1.97}$$

where $x = n_{+1} + n_{-1}$ denotes the total population in the $m_F = \pm 1$ states. Two distinct regimes can be identified:

- **Finite magnetic field ($q > 0$).** The energy is minimized for $x = 0$, implying that all the atoms tend to occupy the $|m_F = 0\rangle$ Zeeman state. The quadratic Zeeman effect favors a polar state aligned with the external magnetic field.

- **Zero magnetic field ($q = 0$).** The Hamiltonian is rotationally invariant. As a consequence, the energy becomes independent on x resulting in a family of degenerate ground states satisfying $n_{+1} = n_{-1}$. These states correspond to spin configurations with vanishing magnetization along an arbitrary spatial direction. Thus, they can be interpreted as global rotations of the spinor state $|m_F = 0\rangle^{\otimes N}$ and they are known as polar states.

The case of systems with a finite longitudinal magnetization is more complex. In this case, a critical value of the quadratic Zeeman shift

$$q_c = \tilde{c_2}(1 - \sqrt{1 - m_z^2}) \tag{1.98}$$

discriminates two qualitatively different ground-state phases.

- **Low-field regime** $q \leq q_c$. The spin energy is minimized for $x = 1$, corresponding to a vanishing population of the $|m_F = 0\rangle$ state but all the atoms are distributed between the $|m_F = \pm 1\rangle$ states in a way they satisfy the magnetization constraint. In this regime, the spin-dependent interaction dominates over the quadratic Zeeman effect: the magnetic field is not strong enough to overcome the energetic cost associated with populating the $|m_F = 0\rangle$ state. The ground state spinor takes the form

$$|\xi_{\mathrm{GS}}\rangle = \begin{pmatrix} \sqrt{(1+m_z)/2}e^{i\phi} \\ 0 \\ \sqrt{(1-m_z)/2}e^{-i\phi} \end{pmatrix} \tag{1.99}$$

and the system is said to be in the antiferromagnetic phase.

- **High-field regime** ($q > q_c$). For sufficiently large quadratic Zeeman shift, it becomes energetically favorable to populate the $|m_F = 0\rangle$ state. In this case, the gain in Zeeman energy exceeds the cost associated to interaction energy arising when mixing the Zeeman components and the system enters in the so called broken-axisymmetry phase, characterized by a nonzero population of all the three Zeeman sublevels. In the limit of very large q, the ground state is obtained by minimizing the Zeeman term alone leading $x \to m_z$ or equivalently, $n_0 \to 1 - m_z$

The transition occurring at $q = q_c$ is a second order phase transition. As the quadratic Zeeman shift is increased beyond the critical value the population of the $m_F = 0$ state grows continuously from zero, showing no discontinuity at critical point but with a qualitative change in the properties of the ground state.

1.4.8 Nematic order parameter

Since the mean-field analysis predicts a second-order phase transition an order parameter must be introduced to distinguish between different magnetic phases. In $F = 1$ systems, this role is played not by the average spin alone (which is not sufficient to fully characterize the state as shown previously), but by a nematic quadrupolar order parameter capturing the spin fluctuations anisotropy.

Within the mean-field and single mode approximations, the ground state of N-particle system is described by the product of N identical single-particle spinors which phase θ is locked to π. The phase locking is a signal of the emergence of spin nematic order.

In the previous Section the competition between spin-dependent interactions and the quadratic Zeeman effect has been interpreted in terms of population redistribution among different Zeeman sublevels. However, it can be equivalently understood as a competition between different types of spin anisotropy. Spin-dependent interactions favor nematic order (alignment without orientation), whereas the quadratic Zeeman effect favors transverse spin polarization.

This anisotropy can be characterized through the spin quadrupolar tensor Q_{ij} fully characterizing the spin alignment. A system with nonzero average spin is known as orientated state, whereas a system with a nonzero quadrupole tensor is known as aligned state.

For a mean-field condensate of N spin 1 atoms, the total quadrupolar tensor scales linearly with N and maintain the same structure of the single

particle tensor. Its eigenvalues quantify the anisotropy of the spin state. By conveniently expressing the quadrupolar tensor in the cartesian basis and considering the normalization constraints, a single scalar parameter $\chi \in [0, 1]$ is sufficient to characterize this anisotropy. From χ parameter one defines the nematic order parameter

$$\mathcal{N} = 2\chi - 1 \tag{1.100}$$

satisfying $|\mathcal{N}| \leq 1$. Nematic states are characterized by $|\mathcal{N}| = 1$, while fully polarized state to $\mathcal{N} = 0$

This formalism allows for a classification of the mean field ground states. Polar (nematic) states which are obtained by rotations of $|m_F = 0\rangle$ state, have vanishing average spin but maximal quadrupolar order, breaking spin rotational symmetry. Conversely, polarized states exhibits maximal spin orientation and reduced nematic order.

In summary, the nematic tensor provides a natural order parameter for the antiferromagnetic $S = 1$ condensate, enabling a clear distinction between the nematic and polarized phases and offering a unified description of the magnetic-field-driven transition.

1.4.9 Beyond Mean-Field Effect

The mean-field theory developed so far provides an accurate description of $F = 1$ Bose-Einstein condensates ground state in the presence of interactions and magnetic fields. However, it fails to account for the large spin-population fluctuations observed experimentally for low atom number systems [18] in the regime of zero magnetization and weak magnetic fields. These fluctuations originate from the high rotational symmetry of the spin Hamiltonian at vanishing quadratic Zeeman shift, where the exact many-body ground state becomes fragmented. A theoretical framework to describe beyond mean field effects is therefore required.

According to the Penrose-Onsager criterion [70], fragmentation refers to the macroscopic occupation of more than one single-particle state and emerges from the exact diagonalization of spin Hamiltonian. A paradigmatic example is provided by multicomponent bosonic systems with a degenerate many-body ground state. Let us consider a system of N bosons with two degenerate single-particle states, $|1\rangle$ and $|2\rangle$. We assume that particles in different internal states interact via a coupling constant g, resulting in an interaction energy

$$E = (g/2)N_1N_2 \tag{1.101}$$

where N_1 and N_2 denote the occupation numbers of the two states. For attractive intercomponent interactions ($g < 0$), the energy is minimized when the

populations are equally distributed between the two states. The many-body ground state is then the Fock state

$$|GS\rangle = \frac{1}{N!}\hat{a}_1^{\dagger N/2}\hat{a}_2^{\dagger N/2}\,|0\rangle \tag{1.102}$$

where $\hat{a}_i^\dagger$ creates a particle in the state $|i\rangle$ with $i = 1, 2$. The corresponding single particle matrix reads

$$\hat{\rho}^{(1)} = \frac{N}{2}\begin{pmatrix} 1 & 0 \\ 0 & 1 \end{pmatrix} \tag{1.103}$$

the two eigenvalues are equal to $N/2$, thus the condensate is fragmented. In contrast, for repulsive interactions ($g > 0$), the energy is minimized when all atoms occupy the same internal state. The system then exhibits two different many-body ground states, $|N_1 = N, N_2 = 0\rangle$ and $|N_1 = 0, N_2 = N\rangle$. If the ground state is described as an equal statistical mixture of these two states, the resulting single particle density matrix coincides with that obtained in the attractive case. The system is therefore again fragmented. In this example the way fragmentation occurs crucially depends on the sign of the interaction parameter resulting in very different many-body states. The two different states correspond to identical single particle density matrices; however, they differ in their higher-order correlations. In particular, the number fluctuations distinguish the two situations: they vanish for the Fock state ($\Delta N_i = 0$), while for the statistical mixture one finds $\Delta N_i = N^2/4$, despite the fact that in both cases $\langle N_i\rangle = N/2$ with $i = 1, 2$. This example demonstrates that fragmentation cannot be fully characterized by one-body observables alone but requires access to higher-order correlation functions to completely determine the nature of the many-body state.

In antiferromagnetic $F = 1$ condensate at zero magnetic field, the spin Hamiltonian within the single mode approximation is rotationally invariant and its ground state is a singlet state which must share this symmetry. This state exhibits isotropic spin populations and super-Poissonian fluctuations scaling as N^2 [71], which are a clear signature of fragmentation. The corresponding single-particle density matrix displays three equal macroscopic eigenvalues, reflecting the absence of a preferred spin direction. As the magnetic field increases, the quadratic Zeeman shift lifts the rotational degeneracy driving the system towards a smooth crossover from a fragmented singlet to a symmetry breaking nematic mean-field condensate with suppressed spin fluctuations. At fixed temperature, the collapse of spin fluctuations occurs on a characteristic scale $q_c \sim 1/N$, corresponding to a magnetic field $B_c \sim 1/\sqrt{N}$. In the thermodynamic limit $B_c \to 0$, so that an infinitesimally small magnetic

field is sufficient to select a symmetry-broken mean-field state. This transition has already been observed for small atom numbers in the zero spatial mode approximation [18], with a transition field between 30 and 100 mG depending on the temperature of the sample. However, we have a spatially extended sample with an atom number of the order of 10^6, thus we expect the transition to take place at a much lower value of the magnetic field of the order of tens of μG.

At finite temperature, the small energy spacing between low-lying spin states prevents the preparation of the pure singlet ground state. Nevertheless, fragmentation persists: low-energy eigenstates exhibit quasi-isotropic populations and large spin fluctuations, remaining essentially identical to those of the zero-temperature singlet state. Increasing the quadratic Zeeman field again suppresses fluctuations and restores a mean-field description.

For experimentally relevant atom numbers, the exact diagonalization of the Hamiltonian becomes impractical and an efficient alternative is required. It is provided by the broken-symmetry approach, in which the exact symmetric state is represented as an isotropic statistical mixture of symmetry-breaking mean-field states. It is possible to show [72] that in the large particle number limit, the two descriptions are equivalent since the expectation values of few-body observables computed within the broken-symmetry framework coincide with those computed on the exact many-body state up to corrections of order $1/N$. The picture provides an intuitive interpretation of spin fragmentation: in each experimental realization the system condenses into a single nematic state, breaking rotational symmetry, while the orientation of nematic axis fluctuates uniformly from shot to shot restoring symmetry on average and producing large spin fluctuations. The resulting delocalization over spin space explains both the isotropic average population and the large spin fluctuations characteristic of the fragmented singlet state.

To extend this description to finite temperature and finite magnetization, the broken-symmetry framework can be generalized using $SU(3)$ coherent states since the nematic states are not sufficient given they always satisfy $\langle \hat{S} \rangle = 0$. These states form an overcomplete basis for the $S = 1$ Hilbert space and become quasi-orthogonal in the thermodynamic limit, allowing for a simple and accurate description of thermal states as statistical mixtures weighted by their Boltzmann factors [18].

Overall, spin fragmentation in spinor Bose-Einstein condensate is a direct consequence of the rotational symmetry of the Hamiltonian and the presence of thin spectrum of low energy states. Its sensitivity to weak magnetic fields and persistence at finite temperature reflects the fundamental mechanism of spontaneous symmetry breaking, which emerges from the non-commutativity

of the thermodynamic and zero-field limits.

Chapter 2

Experimental Apparatus

This Chapter contains a description of the current status of the experimental apparatus required in order to work with atomic mixtures, in a stable magnetic field environment obtained thanks to the presence of a magnetic shield surrounding the science chamber. The installation of such a shield is necessary in order to minimize magnetic noise (at the level of μG) ensuring stability of the level energy shifts on the order of few Hz. This results in a long coherence time under the action of an external coherent coupling field which allows for the manipulation of magnetic mixtures. Beyond an highly stable magnetic field, other key requirements are the use of a state independent trapping potential, obtained by means of an Optical Dipole Trap (ODT) operating at a detuning much greater than the fine splitting of Sodium atoms, and a system for the generation of RF and microwave fields to manipulate the internal state of the sample. The Chapter is divided in four Sections. The first Section contains an overview of the primary components. The second Section contains a brief description of the experimental steps required for the realization of the condensed sample. The third Section describes the imaging techniques and, the last Section, presents a protocol for magnetic field characterization.

2.1 Experimental set up

This Section contains a description of the instrumentation present in the experimental apparatus which is compatible with the presence of the magnetic shield.

2.1.1 Magnetic Shield

We have seen that coherently-coupled quantum mixtures can be realized using different hyperfine states. These systems are described by the GPE, which is derived under the assumption that we know the time dependence of both the Rabi coupling strength Ω_R and the detuning δ. However, this is not the case of experimental systems. In particular, the detuning δ is affected by magnetic field fluctuations via the Zeeman shift. In our laboratory, we typically observe field fluctuations of several milligauss due to electric line noise or moving magnetized objects [73] which are well above the few μG required. Two possible approaches can be used for magnetic field stabilization with respect to environmental noise.

An active approach, in which the magnetic field is continuously monitored by a magnetometer placed in the region where field stability is required [74, 75]. The magnetometer is surrounded by electromagnets, the current circulating in the electromagnets is controlled by a feedback loop stabilizing the value read by the magnetometer. Although this approach can suppress external noise by several order of magnitude, its effectiveness decreases with distance between the magnetometer and the region where the magnetic field should be stabilized. In our setup the presence of the vacuum chamber prevents placing the magnetometer sufficiently close to the atomic sample, making the method unpractical. An alternative more efficient approach is the implementation of passive shielding. In this case the experiment is surrounded by a material with high magnetic permeability, such as a μ-material. However, the shielding performance decreases with the size of the enclosed volume, and beyond a certain size the material cannot sustain the required shielding. For this reason in our setup the shield encloses only the science chamber. It is known that, the performance of the shield can be increased by building a multilayer shield. In Trento we opted for this solution, whose design is described in [76] and its implementation in [73, 77].

In summary, the shield has a cylindrical geometry composed of four layers of high-permeability materials, each of them made of two half-cylinders cut normally with respect to their symmetry axis. The three outer layers are made of μ-material, an alloy with $\mu_r = 4.7 \times 10^5$ and $B_{\text{sat}} = 0.75$ T ensuring a high shielding efficiency. However during the Magneto Optic Trap (MOT) stage in the innermost layer the magnetic field reaches values close to B_{sat} of the μ-material, for this reason the innermost layer is made of SUPRA-50, an alloy characterized by $\mu_r = 2.5 \times 10^5$ but a larger value of $B_{\text{sat}} = 1.5$ T. A scheme of the shield is reported in Fig. 2.1. The design of the shield should guarantee the optical access for the laser beams required for laser cooling, along three orthogonal directions. It must also provide horizontal access for the Optical

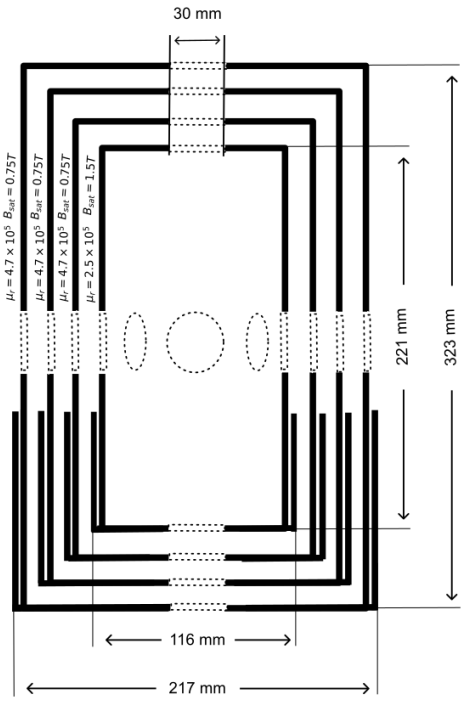

Figure 2.1: Schematic representation of the magnetic shield.

dipole trap (ODT) beam at 1064 nm. All beams have been assumed to have a diameter of 1". The access is guaranteed by 10 apertures of diameter $d =$ 30 mm. Eight of them are on the side of the shield, aligned with the central horizontal plane, but only seven are used for the optical access of the beams, while the other two are on the opposite faces of the cylinder. At the end such a shield configuration results in a suppression factor of 5/6 orders of magnitude of the external magnetic field [78].

2.1.2 Vacuum system

The Vacuum system represented in Fig. 2.2 is composed of two chambers of stainless-steel tubes which are connected by a differential pumping stage. The first chamber is a high vacuum (HV) chamber containing a metallic source of ^{23}Na which is heated in an oven at 250 °C for the production of the atomic hot vapor that serves as the atomic source of the experiment. The pressure inside this chamber is approximately $P \sim 2{\times}10^{-9}$ mbar thanks to a combined effect of a non-evaporative getter and an ion pump (NEXTorr D200-5). Optical access to this chamber is provided by glass windows with an anti-reflection coating

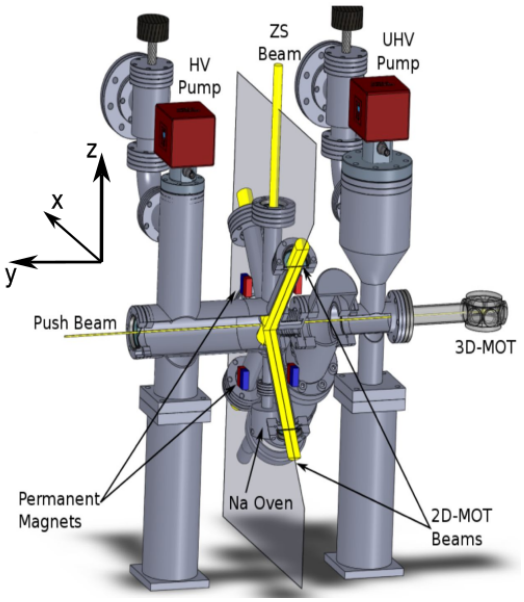

Figure 2.2: Vacuum chambers and science chamber. The magnetic shield, which is not represented in figure, is positioned around the science chamber.

optimized for 589 nm light. The HV chamber is connected to the ultra-high vacuum chamber (UHV) through a differential pumping channel with a 2 mm diameter and 22.8 mm length. The pressure in the UHV chamber is maintained at approximately $P \sim 1 \times 10^{-11}$ by means of the combined effect of a combined vacuum pump (NEXTtorr D500-5) and two gate valves. The UHV chamber includes the science chamber which is an octagonal fused-silica cell connected to the UHV by a 65 mm long glass tube. Here the cold atomic sample is prepared. The optical access to the sample is provided by two windows with a 50.8 mm diameter along the vertical direction (z), and seven windows with 22.9 mm diameter in the horizontal (x, y) plane. All window surfaces are treated with a Random Anti-Reflection Coating, a nano-textured treatment reducing the reflection to 0.3% for wavelengths between 532 and 1064 nm in order to minimize undesired effects such as interference fringes in the imaging [77].

2.1.3 Laser Source

Two independent laser sources at $\lambda = 589$ nm are used for cooling and imaging the atomic sample. One emits close to ^{23}Na D2 line ($3^2S_{1/2} \rightarrow 3^2P_{3/2}$) and the other operates close to ^{23}Na D1 line ($3^2S_{1/2} \rightarrow 3^2P_{1/2}$). Both of them are generated by frequency doubling 1178 nm IR light produced by two Cou-

pling Distributed Feedback (DFB) laser diodes (Innolume DFB-1178-YY-50) amplified and then frequency doubled in resonant optical cavities.

Each laser is frequency-locked to the desired atomic resonance by means of saturated absorption spectroscopy. The stabilized laser beams are then split in different optical paths [77] to implement various actions.

The primary cooling light, used for Zeeman Slower, 2D-MOT, 3D-MOT, Dark Spot, Imaging, repumper and push beam is locked to $|F = 2\rangle \rightarrow |F' = 3\rangle$ D2 line (cooling transition). Dark Spot and repumper are used to recapture atoms which can escape from the cooling transition populating the $|F = 1\rangle$ manifold. These atoms are optically pumped back to $|F = 2\rangle$ using the $|F = 1\rangle \rightarrow |F' = 2\rangle$ (repumper transition) transition of the D2 line generated applying a frequency shift to the cooling laser. The other laser source is locked to the $|F = 2\rangle \rightarrow |F' = 2\rangle$ transition of the D1 line (molasses transition) and it is used for the gray molasses cooling [79]. Fig. 2.3 represents the energy levels scheme and highlights the exploited transitions.

2.1.4 Magnetic Coils

Controllable magnetic fields are generated through pairs of magnetic coils. Each of them is made by several turns of copper wire, designed to maximize the field uniformity, and to minimize interactions with the magnetic shield, preventing its permanent magnetization. The coils are placed on a 3D-printed support structure placed inside the innermost layer of the magnetic shield, surrounding the science chamber. The first set of coils consists of circular coils which are used to generate the quadrupole magnetic field required for magneto-optical trap (MOT) and for magnetic levitation. Each of these coils is made of six turns of square copper tubing of 3 mm width, wrapped in fiberglass for electric insulation. These coils produce a magnetic field along z-axis with a strength of $|B|$=1.34 G/A and an associated gradient ΔB = 0.433 G/(cm A). The heat produced from currents during the MOT stage (up to 50 A) is dissipated through cooling water circulating in the tube. The cooling circuits exits the magnetic shield through two small holes, one on the top and one at the bottom. Two other pairs of square coils are mounted out from the support structure and are used to compensate both the magnetic field and its gradient along x and y directions. These coils are the closest to the magnetic shield, meaning that their generated field can be slightly distorted by the proximity of the shield. However, since these compensation fields are relatively weak, their inhomogeneity is not critical. Each of these pair of coils generates a magnetic field of $|B|$=0.50 G/A with an associated gradient of $\frac{\partial B}{\partial e_i}$= 0.19 G/(cm A) where e_i indicates the axial direction of the coils. Finally, two pairs of coils generate the highly stable vertical magnetic field along the z-axis. Both these

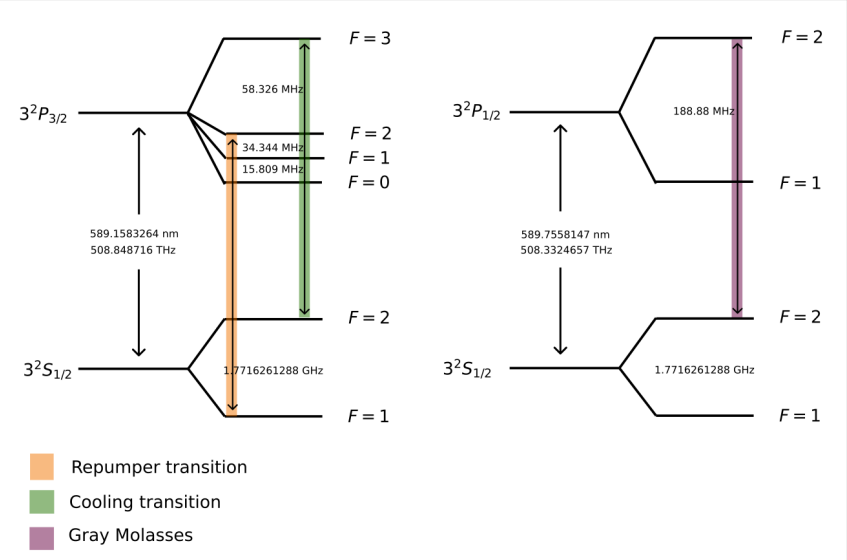

Figure 2.3: Hyperfine structure of the sodium D_2 (left) and D_1 (right) transitions. The frequency splittings between the energy levels are calculated using the ground state energy values reported in [80]. For the excited states, the energy values were taken from [81] for the D_2 line and from [82] for the D_1 line. The colored arrows highlight the transitions employed in the experiment: the orange bar denotes the repumping transition $|F = 1\rangle \rightarrow |F' = 2\rangle$; the green bar indicates the main cooling transition $|F = 2\rangle \rightarrow |F' = 3\rangle$, used for the Zeeman slower, the 2DMOT, the 3DMOT, the dark spot (DS) and the absorption imaging; the purple bar marks the $|F = 1\rangle \rightarrow |F' = 2\rangle$ transition exploited during the gray molasses cooling stage.

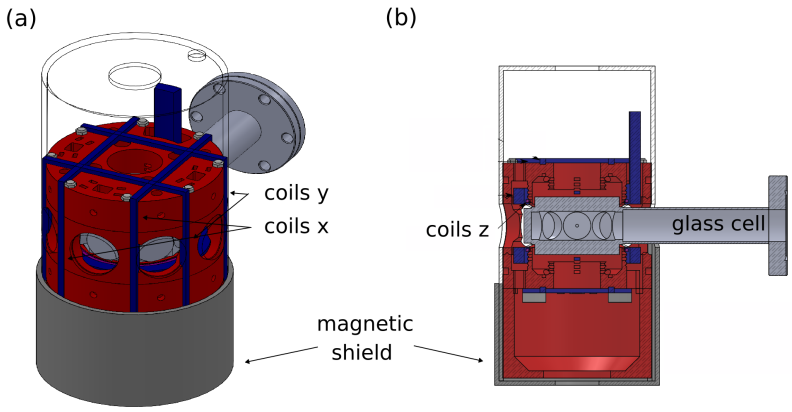

Figure 2.4: Schematics of the core setup. (a) The innermost layer of the magnetic shield (dark gray and transparent) contains a 3D-printed plastic support structure for the coils (red), the coils themselves (blue), and the glass cell (light gray). (b) $y-z$ section of the apparatus.

pair of coils can be used for generating the bias field setting the quantization axis. They are made to minimize field inhomogeneity across the atomic sample, thus they are mounted as close as possible to the science chamber, far from the magnetic shield walls. The first pair of coils (BCompZ-coarse) are arranged in Helmholtz configuration, producing a magnetic field whose modulus is $|B| =$ 2.6 G / A and an associated gradient of $\frac{\partial B}{\partial z} = 0.9$ G/(cm A). The second pair of coils (BCompZ-fine) generates a field whose modulus is $|B|=$ 1.05 G/A and an associated gradient of $\frac{\partial B}{\partial z}=$ 0.37 G/(cmA).

The conversion factors between the current flowing into the coils and the magnetic field generated for the coils along x and y axes has been calibrated with the procedure explained in Sec. 2.4. .

2.1.5 Current Sources

Once the environmental magnetic noise has been reduced by means of the magnetic shield, it is fundamental to produce a very stable magnetic field inside the shield. To achieve this, we use highly stable and low noise current generators minimizing the current noise injected into the bias coils. For the decay time measurements involving the ferromagnetic mixture we need a stable bias field along z-direction. For this purpose we employ a highly stable Laser-Diode Controller (SRS LDC-501), capable of delivering currents up to 500 mA with an RMS noise of 1.5 μA and a long-term drift of 15 ppm over 24

h [83]. This generator is set to supply a constant current of about 50 mA to BCompZ-fine coils, resulting in a bias magnetic field of 130 mG. The current is then modulated by a floating Digital Analog Converter (DAC), which prevents the introduction of electronic noise due to ground loops. The modulation range is ± 10 mA, allowing the bias field to be finely tuned in a range of approximately ± 20 mG. The output current from the driver is controlled by a switching circuit enabling fast turn-on and turn-off of the magnetic field via a TTL signal.

For the experiment involving $S = 1$ mixture for magnetic field characterization, the experimental sequence was initially developed using the current sources available in the laboratory. The longitudinal magnetic field is generated using a Stanford Research System (SRS) LDC501 current controller, while the transverse fields are supplied by Delta Elektronica ES 015-10 power supplies equipped with 10:1 current dividers.

Since the SRS LDC501 is a unipolar current source, it cannot directly generate magnetic-field ramps crossing zero. However, the experimental protocol requires the longitudinal field to be swept continuously from positive to negative values within a single experimental run. This is achieved by connecting two unipolar current sources in parallel with opposite polarities. One SRS acts as a master supply, providing a constant current of 100 mA (corresponding to approximately 245 mG), while a second SRS delivers an adjustable current in the opposite direction, enabling controlled tuning of the net longitudinal field.

Then, the generators just described have been substituted by very stable bipolar current generators. The magnetic fields along the x, y and z axes are

Name	Axis	$\|B\|$(G)	$\frac{\partial B}{\partial i}$(G/cm)	N	M	d (mm)	r (mm)
MOT	z	1.34	0.433	3	2	30	36
BCompZ-fine	z	1.05	0.373	2	2	32	33
BCompZ-coarse	z	2.606	0.898	3	3	32	32
BGradZ	z	0.50	0.186	2	1	32	32
BCompX	x	**0.50**	0.19	2	2	47	86
BCompY	y	**0.50**	0.19	2	2	47	86
BGradX	x	0.5	0.19	2	2	47	86
BGradY	y	0.5	0.19	2	2	47	86

Table 2.1: Coils mounted in the experimental apparatus. The values for $|B|$ are obtained at the atm position driving the coils with a current I = 1A. The value $\frac{\partial B}{\partial i}$ is the gradient along the axial direction i at the atom position obtained for a current of 1A. Values in boldface were measured while the others have been taken from [73].

produced using PROLAN BCS 002/10 current generators, which are capable to provide currents in the range ±20 mA with a stability of 0.1μA. The magnetic field gradient along the x axis is generated by a PROLAN BCS 1/1, capable of delivering currents in the range $\pm 1A$ and a stability of $10\mu A$. Both systems are modulated by grounded DACs and controlled by a TTL switching circuits. Tab. 2.2 summarizes the maximal value and the modulation range of the DAC voltages, the generated currents, the corresponding magnetic fields and their resolution for each pair of coils, taking into account the DAC voltage resolution, the current to magnetic field conversion factor of each pair of coils, and the stability of the current generators. Overall, this result in a field stability at the level of the fraction of a μG for the magnetic field along each of the three axes, and of 10^{-2}mG/mm for the magnetic field gradient along x-axis.

2.1.6 Microwave System

A high-precision apparatus for generating radio-frequency (RF) and microwave fields is required to explore the energy landscape of the hyperfine Zeeman sublevels. For sodium atoms the energy difference between the two hyperfine manifolds is $\Delta E_{F=1\to F=2} \approx 1771.6$ MHz, while the splitting between Zeeman sublevels within the same manifold is $\Delta E_{|F,m_F\rangle\to|F,m'_F\rangle} \sim 700$ kHz/G.

For the False Vacuum Decay measurements, microwave fields are used both for imaging and for coherent manipulation of the atomic states. The main requirements for this system are to have a fast and controllable switching time (< 1 μs), a high frequency stability over a wide power range, and a controllable phase.

A key component of the system is a microwave synthesizer (Marconi Instruments 2024) producing a carrier at 1.67 GHz. The output is controlled by a TTL switch signal with a switching time of about 20 ns.

A direct digital synthesis emitter (DDS) based on the Analog Devices AD9958 chip, can generate a tone tunable in frequency and amplitude, with

	Input Control Voltage		I		B	
	Max. (V)	Res. (μV)	Max. (mA)	Res. (μA)	Max. (mG)	Res. (μG)
B_x	2	66	4	0.13	2	0.06
B_y	2	66	4	0.13	2	0.06
B_z	0.4	13	0.8	0.1	2	0.25
∇B_x	1	0.03	100	10	100/mm	10/mm

Table 2.2: Operational range and resolution of the DAC voltage and current outputs, and the resulting magnetic fields along the x-, y- and z-axes, including the magnetic field gradient along the x-axes.

a 0.1 Hz frequency resolution and $2\pi \cdot 2^{-14}$ rad phase resolution. This tone is mixed with the 1.67 GHz carrier, acting as a local oscillator, using a high-frequency mixer (Mini-Circuits ZEM-4300+). This process up-converts the signal from the DDS to the desired target frequency near 1.77 GHz, producing a phase coherent microwave fields with tunable frequency and amplitude. The DDS system can be remotely controlled with a response time of about 30μs, allowing fast and precise manipulation of the internal states of the atoms.

The output of the mixer contains several components, there is a higher sideband around 1.771 GHz, a lower sideband around 1.571 GHz and a carrier leak. Since only the higher sideband is resonant with the atomic transition we suppress the unwanted spectral components through a band-pass filter (Mini-circuits VHF-1760+ high-pass filter and VLF-1500+ low-pass filter) minimizing power losses.

The filtered signal is then amplified by a 100 W RF power amplifier (Mini-circuits ZHL-100W-272+). At the amplifier output there is a multi-stub tuner (Maury Microwave Tripple-stub 1819A) used to match the impedance between the amplifier and the transmission antenna that radiates the sample. To minimize power losses (about 2 dB/m), introduced by the RG-174 coaxial cable to the antenna, the amplifier is mounted as close as possible to the vacuum apparatus.

Several antennas are installed around the science chamber, each with different geometries and orientations, in the innermost layer of the magnetic shield. These antennas radiate the microwave field to the atomic sample and are fed through short RG-174 coaxial cables.

2.1.7 Imaging System

The density distribution of the ultra-cold atomic sample is reconstructed through absorption imaging. In our setup, it is possible to image the sample along the two orthogonal directions x and z, thus obtaining two-dimensional column densities in which information along the imaging axis is integrated.

For the horizontal imaging (along x-axis) there are two CCD cameras (Stingray F-201B). One is dedicated to high-resolution imaging of the BEC. Inside the magnetic shield, a lens with focal length f = 50 mm is positioned with the focal plane on the atoms. A second lens with the same focal length is used to form a telescope with unitary magnification. The second camera aligned along the same axis is mainly used for the imaging of thermal atoms during the MOT stage. It is placed 45 cm farther away from the atoms with respect to the other camera. The initial part of the optical path is shared with the first system, namely the telescope formed by the two f = 50 mm lenses. Then an additional lens with focal length f = 100 mm is introduced. The

lens is positioned 40 cm from the telescope and 12 cm from the camera. The resulting configuration produces an overall demagnification of approximately a factor 3, which is suitable for imaging the larger spatial extent of the thermal cloud during the MOT phase. The high power 1064 nm optical dipole trap beam also propagates in this direction. To isolate the imaging light from the infrared ODT beam, the two paths are separated by a dichroic mirror, followed by an interference filter removing the residual infrared radiation before the imaging beam reaches the camera.

The vertical imaging (along z-axis) is performed using a fast CMOS camera (Hamamatsu Orca Flash 4.0) having a resolution of 2048 $\times$ 2048 pixels and a dynamic range of 37000:1. The probe light is circularly polarized and resonant with the $|F = 2\rangle \rightarrow |F' = 3\rangle$ transition of sodium. Along the imaging path, the first optical element is an objective composed of two lenses, an achromatic one with $f = 75$ mm (Thorlabs AC254-075-A) and a spherical lens with $f = 300$ mm (Thorlabs LA1484-A) in a doublet configuration necessary to avoid optical aberrations arising from the finite spatial extent of the condensate. This doublet forms an effective focal length of 60.8 mm and it is mounted such that the atoms are in its imaging plane. After the doublet, a mirror, a $f = 60$ mm lens and a quarter-wave plate, used for MOT and the gray molasses (GM) beams, which also enter the chamber from this direction, are mounted on a movable support allowing to temporarily remove the optical assembly after the cooling stages to allow the probe light reaching the camera during the absorption imaging.

Then, a quarter wave-plate converts the transmitted light from circular to linear polarization, and it is relayed to the camera through a $f = 400$ mm spherical lens (Thorlabs LB1862-A), resulting in a total magnification factor of 6.5x. This configuration results in a spatial resolution of 1 μm/px, as each camera pixel has a size of 6.5 μm. The imaging optical paths are shown in Fig. 2.5.

2.1.8 Optical Dipole Trap

Since we work with mixtures of hyperfine states, it is necessary to implement a trapping potential which is not spin-selective. Magnetic potentials only confine low field seeking states; therefore, a solution consists in using a far detuned optical trap. Off-resonant optical dipole traps are, in general, sensitive to spin state depending on their polarization and on the orientation of bias magnetic field [84]. However they provide a spin independent potential when the light is linearly polarized and parallel to the bias magnetic field.

In particular, we use an infrared (IR) laser beam both for evaporative cooling and for trapping the BEC mixture. In the limit where the detuning

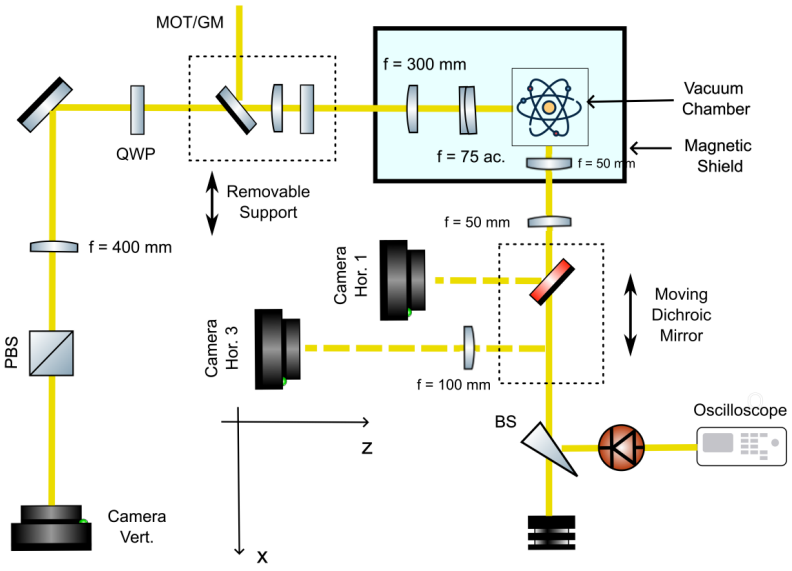

Figure 2.5: Schematic representation of the imaging system. BS: beam splitter; PBS: polarizing beam splitter; QWP: quarter-wave plate.

from the center of the D-line doublet is much larger than the fine-structure splitting, the optical dipole potential for alkaline atoms is given by

$$U_{\mathrm{dip}}(r) = \frac{3\pi c^2}{2\omega_0^3}\frac{\Gamma}{\Delta}\left(1 + \frac{1}{3}Pg_F m_F \frac{\Delta'_{\mathrm{FS}}}{\Delta}\right) I(r) \tag{2.1}$$

where g_F is the Landé factor, ω_0 is the optical resonance frequency, P is the beam polarization and $I(r)$ is the the spatial intensity profile of the light beam. When the light is linearly polarized with respect to the bias magnetic field, the spin dependent term is suppressed, ensuring a spin insensitive potential. The sign of Δ determines if the potential is attractive ($\Delta < 0$) or repulsive ($\Delta > 0$).

Our optical source is a CW fiber laser (Azur Light Systems ALS-1064-50-I-SF) producing 40W of IR light at 1064 nm.

A Second Harmonic Generation (SHG) crystal placed in a focus of the beam converts part of the IR light into green light of 532 nm, with a conversion efficiency up to 20%.

The majority of the remaining IR light is used for the beam entering in the main chamber along the x-direction. Its maximum power is 7 W and it is focused on the sample to a waist of 18 μm through an $f = 200$ mm lens, resulting in a cigar-shaped atomic distribution elongated along the x-axis.

All beams are delivered to the science chamber through large mode area

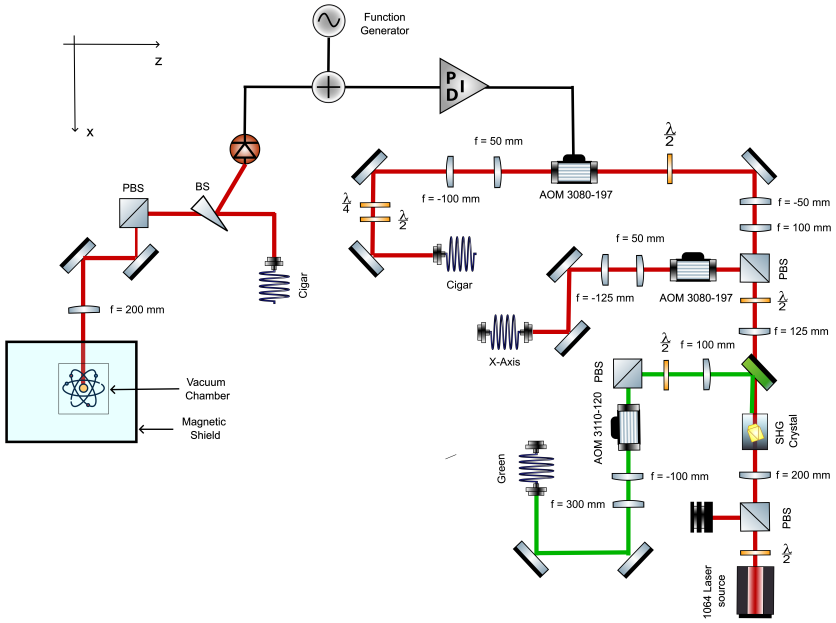

Figure 2.6: Optical path for IR beam. Cigar beam is the only beam used in the experiment. On top, the electronic circuit used fro modulation of the Cigar s represented, with the signal coming from a function generator summed to the setpoint of the ID input to ensure the correct locking during the modulation. Green lines refer to teh path of 532 nm light shined on the DMD while red ones to IR light.

photonic crystal optical fibers (NKT Photonics LMA-PM-10). High power acusto-optic modulators (AOMs) are installed before each fiber. They are used as fast optical switches and to stabilize the beam intensity using a PID controller (SRS SIM960). The error signal is sampled after the fiber, where a beam sampler diverts a small portion of the beam to a photodiode which is connected to a Proportional-Integral-Derivative (PID) controller and the PID setpoint is controlled remotely via a DAC, enabling precise and rapid modulation of the optical power. Then, a fast photodiode (Thorlabs DET36A/M) is placed at the output of the science chamber to monitor the frequency, the amplitude and phase of the modulated signal capturing the intensity of the Cigar beam. The optical path of the IR beam is shown in Fig. 2.6.

2.2 Production of condensate sample

This section describes the experimental protocol used to produce the Bose-Einstein condensate.

2.2.1 Cold atom source

The Zeeman slowering is the first cooling stage taking place in the HV chamber. Metallic sodium is heated at 250 °C in an oven to evaporate atoms generating an atomic vapor. It is slowed down in the vertical direction by a 12 cm long Zeeman slower (ZS). The slowing is achieved using four permanent magnets in a quadrupolar configuration producing the magnetic field, together with an optical radiation propagating against the direction of the effusive flow of the atoms and circularly polarized. It is a 1" laser beam with an intensity of I = 160 mW/cm^2. Its frequency is red-detuned by 330 MHz from the $|F = 2\rangle \rightarrow |F' = 3\rangle$ D2 transition, and an EOM generates sidebands such that 50% of the total power is used for cooling, 25% for the repumper transition, and the remaining 25% stays out from resonance.

2D-MOT is the second cooling stage taking place in the cold atom source, it confines the atoms in in the x-z directions [85, 86]. The 2D-MOT is created exploiting the same permanent magnets used for ZS to generate the magnetic field, together with a laser radiation of intensity $I = 10$ mW/cm^2. The light consists of two orthogonal, circularly polarized beams propagating along the x-z plane, rotated by 45 degrees with respect to the Cartesian axes and retroreflected. The radiation has the same spectral structure of the one used for the ZS, except that the carrier is red-detuned by 13 MHz with respect to the $|F = 2\rangle \rightarrow |F' = 3\rangle$ D2 transition. The atomic vapor trapped in the 2D-MOT is then pushed by a low intensity push beam, resonant with the D2 line and propagating along the y direction, into the UHV chamber through the differential pumping channel and subsequently in the science chamber.

2.2.2 3D-MOT

After the 2D-MOT stage, the atoms are pushed into the science chamber, where they are captured by the Dark-Spot 3D-MOT (DS-MOT) [87]. The trap is realized using cooling light detuned 18 MHz to the red of the $|F = 2\rangle \rightarrow |F' = 3\rangle$ D2 transition, and splitting it into three pairs of counter-propagating beams with opposite circular polarizations (σ^+ and σ^-) propagating along the three orthogonal directions: the vertical direction, coinciding with the z-axis, and two horizontal directions oriented at 45° with respect to the x and y axes.

The beam along the z-axis is delivered to the atoms via a motorized mirror placed below the magnetic shield and removed at the end of the MOT stage because its optical path overlaps with the vertical imaging path. In our DS-MOT the repumper beam is obtained through an axicon, which moves the intensity of the beam at the edges, and a circular obstacle which blocks the central part of the beam resulting into a high intensity hollow-core beam. The obstacle is imaged on the atoms through an $f = 150$ mm spherical lens. Such a configuration solves the issue that a fraction of atoms can decay in the $|F = 1\rangle$ state, which is a dark state for the cooling transition, due to the small 58 MHz splitting between the $|F' = 3\rangle$ and the $|F' = 2\rangle$ states [88]. Our repumper beam, resonant with the $|F = 1\rangle \rightarrow |F' = 2\rangle$ transition, returns these atoms to the cooling cycle. Because of the hollow-beam geometry, only atoms in the outer region of the MOT are repumped in the cooling cycle, reducing light assisted collisions and photon reabsorption in the trap center where the cold atoms accumulate. At the end of this cooling stage, we obtain a sample of approximately 2×10^9 atoms at a temperature of 300 μK, which is slightly above the Doppler temperature for sodium ($\sim 255\mu$K).

2.2.3 Gray Molasses

This is a sub-Doppler cooling technique based on the gray molasses (GM) scheme, demonstrated for sodium atoms using the $|F = 2\rangle \rightarrow |F' = 2\rangle$ D1 transition in [79]. This scheme is highly efficient because it transfers the slowest atoms into a dark state, where they no longer interact with the cooling light, thereby reducing the reheating due to photon scattering. During the GM stage, all magnetic fields are switched off, and we apply a 0.5 ms pulse of blue-detuned light, 40 MHz above resonance, with an intensity I/I_{sat}=150 mW/cm^2. After this stage, the sample reaches a temperature of $T \sim 25$ μK with nearly unity capture efficiency. Then, a second GM stage follows, in which we first quench the detuning to 100 MHz and then linearly reduce the laser intensity to zero over 5 ms.

In this way we reach a final temperature of 13 μK, which for sodium is just one order of magnitude above the singe-photon recoil temperature $T_{\text{rec}} = \hbar^2 k^2 / m k_B = 2.4$ μK.

2.2.4 Hybrid Trap

After the GM cooling stage, we perform the evaporative cooling to reach Bose-Einstein Condensation [89]. The evaporation takes place in an optical dipole trap [90], where we obtain a BEC of about 2 million atoms in the hyperfine state $|1, -1\rangle$. The atoms are loaded into the optical dipole trap using a hybrid

trapping configuration. This consists of a horizontal cigar-shaped trapping beam at full power (7W), corresponding to a trap depth of $k_B 440\ \mu$K, combined with a magnetic quadrupole field with gradient $\partial B/\partial z = 13$ G/cm. The optical dipole trap is positioned approximately 1 mm below the center of the quadrupole field. The loading efficiency into the optical potential is enhanced by an adiabatic compression of the quadrupole gradient to 22 G/m over 500 ms, allowing for the accumulations of roughly 3×10^7 atoms in the optical trap. The atoms which are not collected by the optical trap are let escape by ramping the quadrupole gradient to 7.7 G/cm, slightly below the gravity compensation value of 8.1 G/cm. Under this condition, atoms confined solely by the quadrupole reservoir are no longer supported against gravity and are therefore allowed to escape, leaving only the atoms trapped in the optical dipole potential.

Evaporative Cooling It takes place in two subsequent steps. The first step is obtained by linearly reducing the trap depth to $k_B \times 53\mu K$ over 2s. Afterwards, we turn on a uniform bias field of 130 mG along z-axis and adiabatically switch off all the other magnetic fields. Then a second evaporation stage is obtained applying an exponential ramp over 1s, reaching a final trap depth of $k_B \times 3.5\mu$K with 2×10^6 atoms and negligible thermal component. The trap is then adiabatically recompressed in 500 ms to a variable final depth setting the desired trap frequencies. At the end of this stage, a cigar-shaped condensate elongated along the x-directions is obtained. For the measurements involving the ferromagnetic mixture, the final trapping frequencies are $(\omega_x,\omega_r)/2\pi =$ (15,2020) Hz [91] and corresponding Thomas-Fermi radii $(R_x,R_\perp) \sim$ (250,2) μm. For the measurements performed with $S = 1$ mixture, the final trap depth is reduced such that the trapping frequencies are a factor of two smaller than in the previous experiment. The recompression to higher trapping frequencies introduces additional heating, increasing the thermal fraction and reducing the final number of atoms in BEC to approximately 1×10^6.

2.3 Imaging Techniques

Absorption imaging is used to extract the atomic column density distribution along the two imaging axes shown in Fig 2.7: the horizontal x-axis and the vertical z-axis. Since our experiments involve mixtures of hyperfine states, spin-selective imaging is required.

Horizontal imaging For horizontal imaging, the different spin states are distinguished through Stern-Gerlach (SG) separation. After the sample manip-

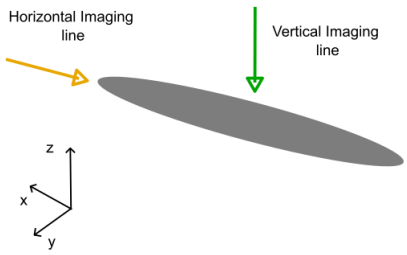

Figure 2.7: Imaging axes with respect to the condensate geometry. (Orange) Horizontal imaging, probing the condensate in the radial direction. (Green) Vertical imaging, probing the condensate in the axial direction.

ulation, the trap is switched off and the cloud expands to avoid optical-density saturation. A magnetic quadrupole field is then applied, introducing a gradient of 8 G/cm, which exactly compensates gravity for the $|F = 1, m_F = -1\rangle$ state, while the other spin components experience either an upward or a downward force, depending on the sign of $g_F m_F$. Once the spin states are spatially separated, absorption imaging is performed. The atoms are first transferred to the $|F = 2\rangle$ manifold via a short repumper pulse, followed by a probe beam propagating along x-direction and resonant with the $|F = 2\rangle \rightarrow |F' = 3\rangle$ transition. The probe beam has to be circularly polarized for a correct atom-number determination [92]. The magnetic field gradient is switched off just before the probe pulse, and a small bias field along x is turned on to ensure the proper probe polarization. Imaging along this direction integrates over the condensate's long axis; thus, it does not allow for the characterization of spatial spin structures. However, it is useful for characterizing the global sample response. For instance, it is used for Rabi frequency measurements, magnetic field calibration and temperature measurements.

Vertical imaging It allows for observation of the axial profile of the condensate. Along this direction, spin-selective imaging is implemented via microwave transitions. A separate image is taken for each m_F state, separated by 1 ms. This multiple image acquisition is allowed by the fast acquisition rate of the CMOS camera [93].

Due to the high density of the sample, a direct in-situ measure is not feasible since the optical density is too high and no light reaches the camera. The issue is solved by combining a short time of flight (TOF) of 1 ms before imaging with Partial Transfer Absorption Imaging (PTAI) technique [94, 95]. In PTAI, only a small fraction of the sample is transferred to a state resonant with the

probe light, preventing saturation and allowing for quasi-in-situ imaging. The probe light is resonant with the stretched state $|2,-2\rangle$.

For the experiment involving the ferromagnetic mixture, the state $|2,-2\rangle$ is populated from the mixture itself. Thus, the first image is taken directly by probing the state $|2,-2\rangle$ 1 ms after the trap release. One millisecond later, a microwave π-pulse (applied using the same antenna used for coherent coupling) transfers the atoms from $|1,-1\rangle$ to the imaging bright state. The Rabi frequency of the pulse is about 25 kHz, well above any other energy scales thus it is robust against fluctuations of the resonant frequency. After the transfer the second probe pulse is sent. Because of the tight radial confinement ($\omega_\perp/2\pi \approx 2$kHz), the radial size of the cloud in the second image is about twice that of the first while the axial size is approximately unchanged. Since the cloud size evolves as [96]

$$\frac{R_\perp(t)}{R_\perp(0)} = \sqrt{1+\omega^2 t^2} \tag{2.2}$$

a TOF of 1 ms before the first image acquisition is sufficient to avoid imaging saturation while leaving the dynamics along the axial direction unchanged. The amount of transferred population is controlled by the microwave-pulse duration, which is typically 21.3 μs to obtain a full π-pulse.

2.4 Magnetic field characterization

As previously mentioned, achieving a sufficiently long coherence time to perform the experiments requires a well-defined and stable magnetic field. In our case, field stability at the level of 5 μG is required both over long time scales, on the order of several hours of experimental runs, and over the shorter time scales of sample dynamics. This level of stability for the magnetic field translates into controlling the energy levels with precision on the order of 10 Hz. In this Section, we describe the protocol used to characterize the magnetic field and its stability, exploiting the atoms themselves as a magnetometer. The use of spin systems as sensitive magnetometer has been discussed, for example, in [97]. In particular, we perform spectroscopic measurements, at first to accurately determine the detuning between the microwave frequency and the atomic resonance between the Zeeman sublevels, thereby calibrating the resonance condition.

Two level system We have already mentioned that transitions between two different Zeeman sublevels driven by a near-resonant electromagnetic field can be described as a two-level system, with populations evolving according to

the Bloch equations. The coupling induced by the magnetic field $\vec{B}$ of the radiation is characterized by the Rabi frequency

$$\Omega_R = \frac{\langle 2| \vec{\mu} \cdot \vec{B} |1\rangle}{2} \tag{2.3}$$

where $\vec{\mu}$ is the magnetic dipole operator, and by the detuning δ. For magnetic dipole transition between sublevels of the electronic ground state, spontaneous emission rate is negligible and the evolution remains coherent. Within this two-level treatment, the magnetic field, at the position of the sample, can be determined with high precision measuring the transition frequency ω_0 between the sublevels. The Bloch equations give the population transferred to state $|2\rangle$ from the initial state $|1\rangle$ after a time t:

$$n_{22} = \frac{\Omega_R^2}{\Omega_R^2 + \delta^2} \sin^2 \left(\frac{\sqrt{\Omega_R^2 + \delta^2}}{2} t \right) \tag{2.4}$$

The excitation probability can be obtained from the measured population in the two states, giving the characteristic sinc-shaped spectroscopy curve when applying a pulse of duration π/Ω_R (a π-pulse) while changing detuning δ. The population transfer can also be expressed in terms of magnetization:

$$Z = (N_2 - N_1)/(N_1 + N_2) = 2n_{22} - 1 \tag{2.5}$$

which is therefore a function of Ω_R, δ and t.

Resonance conditions To create spin mixture, it is fundamental to match the resonance condition with high precision. This can be achieved either by finely tuning the transition frequency or by adjusting the magnetic field. A spectroscopic measurement is performed by applying squared pulse of duration π/Ω_R at a given Rabi frequency Ω_R, for different values of detuning δ. The detuning is varied by applying small corrections to the bias magnetic field around the reference value of 130 mG, while keeping the microwave frequency fixed. After each pulse, we perform spin sensitive horizontal imaging so that the two internal states are separated via a SG measurement, and their respective populations are detected through an absorption imaging. The magnetization measured after the π-pulse as a function of the detuning is then fitted through the expression:

$$Z(\delta) = -\frac{\delta^2 + \Omega_R^2 \cos(\Omega_R^2 + \delta^2)t}{\Omega_R^2 + \delta^2} \tag{2.6}$$

Where δ is the fitting parameter. The expression has been obtained by inserting Eq. 2.4 in Eq. 2.5. The width of the resulting sinc-shaped spectrum

is proportional to the value of the Rabi frequency. Therefore, to measure the resonance condition precisely, it is advantageous to work with relatively small values of Ω_R. In general, for our measurements we employ Rabi frequencies of a few hundred Hz. However, such low Rabi frequencies, prevent us from working with a BEC because density-related shifts would appear. To circumvent the issue, we use a diluite thermal cloud in order to suppress atom-atom collisions and mean field frequency shifts. An example of measurement is reported in Fig. 2.8, where the green dots are the experimental data and the gray line is the fitted response function 2.6.

Once the field correction required to match the resonance condition is known, a similar measure can be performed to measure the Rabi frequency, by applying pulses of variable duration at zero detuning. In this case, the expression above reduces to the usual cosine dependence expected for on-resonance Rabi oscillations. An example of measure is reported in Fig. 2.9 where Rabi frequency is estimated to be $\Omega_R = 150$ Hz.

Magnetic coils calibration A spectroscopic measurement is also used to calibrate with high precision the magnetic fields applied along the x and the y directions. This procedure allows us to determine the conversion factor between the current flowing through each pair of coils, which is controlled via software, and the corresponding generated magnetic field (values reported in Tab. 2.1). This calibration is essential for the experiment described in Chapter 4, where a precise knowledge and control of the transverse magnetic fields are required. The calibration is performed by applying a π-pulse while scanning the μ-wave frequency, in the presence of a fixed and well defined current in one of the transverse coil pairs. This current sets a magnetic field of constant magnitude along the selected axis. For each frequency value, the excitation probability is measured. The maximum of the resulting sinc-shaped Rabi spectrum identifies the resonance condition, corresponding to the transition frequency between the two hyperfine states.

The shift of the resonance frequency with respect to the zero-field transition frequency provides a direct measurement of the Zeeman shift. By applying the Breit-Rabi formula [88], this shift is converted into the absolute value of the magnetic field, $|B|$. The experimental protocol is illustrated in Fig. 2.10.

Since a well defined field along the longitudinal direction is required during the condensation and imaging stages, whereas a well defined transverse field is necessary for the spectroscopic measurement, magnetic field ramps are implement before and after the μ-pulse. These ramps ensure the establishment of the desired field configuration in each stage and guarantee an adiabatic rotation of the atomic spin state when switching between longitudinal and transverse

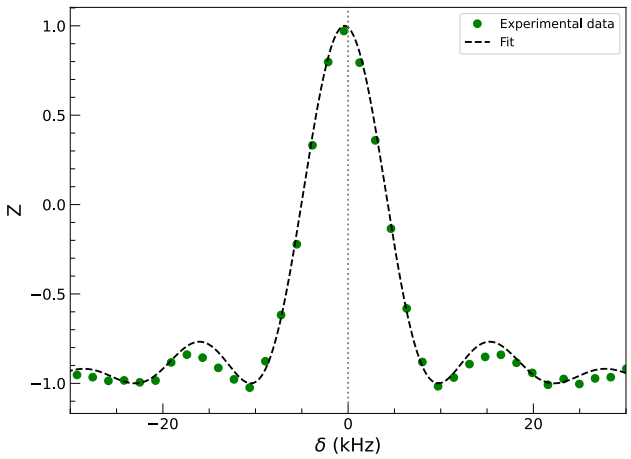

Figure 2.8: Spectroscopic measurement of the resonance condition at $\Omega_R = 580$ kHz. At the bias magnetic field of B = 0.13 G the transition frequency results to be $\omega_0 = 1771352865$Hz, form this spectroscopy we obtain a frequency shift of 0.38 kHz corresponding to a shift in the magnetic field of 0.19 mG.

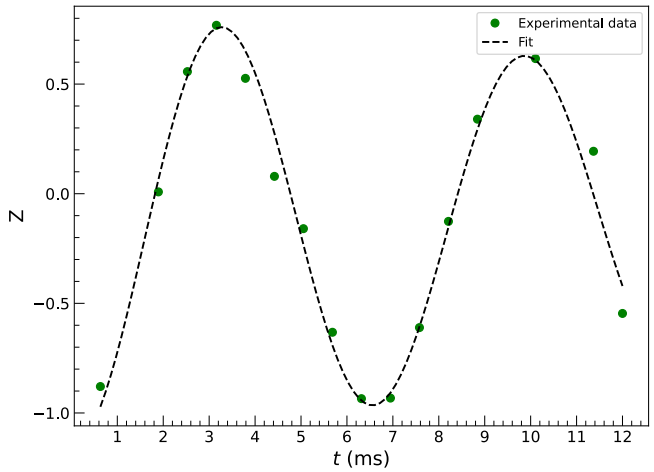

Figure 2.9: Example of the Rabi frequency calibration performed through a scan in the pulse duration, once the resonance condition is known.

directions.

The measurement is repeated for three different current values for each axis. The corresponding values of the magnetic field are extracted from the Breit-Rabi fits for x and y axes, respectively. Then, the experimental data are fitted with a linear function, yielding an angular coefficient: $m_x = 0.526$ G/A and $m_y = 0.523$ G/A giving the conversion factor between the applied current and the generated magnetic field.

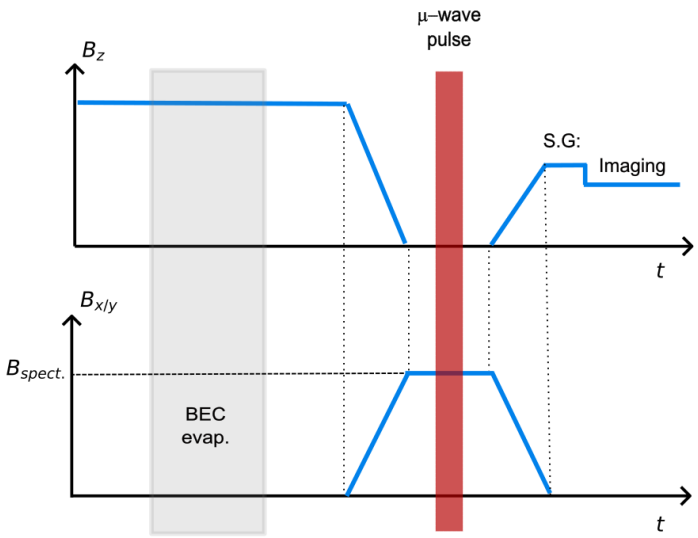

Figure 2.10: Experimental protocol for magnetic coil calibration. Magnetic field modulus along z-axis (upper panel) and along the transverse axis being calibrated (lower panel) as function of time.

Chapter 3

False Vacuum Decay in Ferromagnetic BECs

Metastability is a common feature of systems undergoing a first-order phase transition. It arises when the system remains trapped in a local minimum of the free-energy landscape different from the absolute minimum. Such a situation is ubiquitous in classical many-body systems and in chemical processes. A typical example is superheated water, where the liquid-to-gas transition takes place via stochastic nucleation of vapor bubbles around nucleation spot such that microscopic impurities or surface defects. A nucleated bubble is energetically favorable only when its size is sufficiently large that the bulk free-energy gain compensates the surface-tension cost.

In classical systems, decay from a metastable state occurs when thermal fluctuations or structural inhomogeneities drive the system to jump above the energy barrier separating the metastable and the stable minima. The process can be generalized to quantum fields and plays an important role in cosmology, due to its consequences on the stability of Higgs bosons [98, 99] and to its applications to inflationary models describing the early universe [100, 101, 102].

Within the double minimum picture, differently from the single particle case, the system can be described by a spatially dependent macroscopic field which can decay from a local to the absolute minimum. This decay mechanism is a macroscopic process known as False Vacuum Decay (FVD) in which the field describing the system changes configuration. The system described by the field is initially in the metastable configuration (the false vacuum) and decays to the stable minimum (the true vacuum) via field tunneling across the energy barrier of the effective double well potential (Panel (a) of Fig. 3.1). In an energy conserving system the transition proceeds through the stochastic nucleation of spatially localized resonant bubbles of true vacuum. A bubble can

survive only if its initial size satisfies the balance between surface energy cost due to created domain walls and volume energy gain. Once formed, the bubble grows into the surrounding false-vacuum region driving the entire system to the fundamental state, with the excess energy released as excitations around the true vacuum.

A key difference with the classical relaxation case is that the quantum decay rate depends on the Euclidean action associated with the barrier [10], rather than on the barrier height itself. In the zero-temperature limit, decay is exclusively driven by quantum fluctuations as described by Coleman's instanton formalism [10, 103]. Finite temperatures, however, enhance nucleation via thermal fluctuations as discussed by Linde [104] who extended the previous formalism to the finite temperature case.

A complete theoretical characterization of FVD requires the determination of both the nucleation rate and the bubble dynamics after its creation. In our experiment we focused only on the first aspect. In practice, analytical predictions of the tunneling time are challenging due to the strongly non-perturbative nature of the process. The semiclassical calculations based on the instanton solution provide the leading approximations and predict an exponentially suppressed nucleation rate with system parameters making both numerical and experimental studies very difficult due to the challenging time scales for the characterization of the decay process.

A platform suitable for FVD observation must satisfy some requirements. It must support a macroscopic coherent field description; it should allow precise control of external parameters; it must present a nonlinear interaction term generating an effective potential barrier at mean field level; it must be spatially extended to support bubble nucleation and the characteristic timescales must be experimentally resolvable across several orders of magnitude to catch the exponential dependence of the decay time on the action across the potential barrier.

Extended superfluid mixtures can meet all these criteria. They are characterized by long-range coherence, high stability and broad tunability of the experimental parameters in an isolated environment [105, 106]. The first proposals, such as quantum spin chains [107] or non polarized binary BEC mixtures in the presence of a periodically modulated coherent coupling [105], suffer from some limitations concerning spatial discretization, for the first solution, or competing dynamical instabilities with the same timescale of bubble nucleation, for the second solution.

A particularly promising candidate for experimentally characterizing the FVD is provided by coherently coupled polarized BEC mixtures. In Chapter 1 we have shown that by properly choosing the hyperfine states, the system

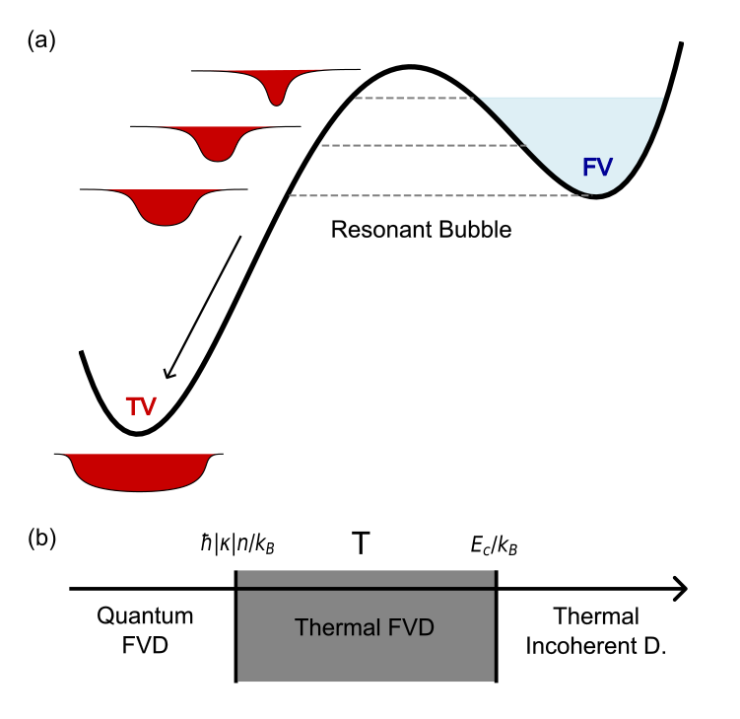

Figure 3.1: Panel (a): FVD process in the 1+1 ϕ^4-theory. Fluctuations trigger the nucleation of resonant bubbles, after the creation they expands rapidly. For the finite temperature case we have to consider also the contribution of all the excited state above the false vacuum state (shaded blue area) with a weight given by the Boltzmann factor. Panel (b) Relevant regimes in the FVD. When temperature si smaller that the one associated to interactions ($\hbar|\kappa|n/k_B$), quantum fluctuations dominate in the FVD process. If temperature is higher than E_c/k_B, where E_c is the instanton energy, the decay is an incoherent process. For temperatures in between these two regimes FVD is driven by thermal fluctuations.

undergoes a paramagnetic-to-ferromagnetic phase transition. Describing the system in terms of its magnetization, the ferromagnetic phase is characterized by a double well potential. Ref. [12] reports the experimental observation of finite-temperature false vacuum decay in isolated and coherently coupled atomic superfluids, observations also supported by numerical simulations. The study demonstrates quantitative agreement between observations and instanton theoretical predictions based on a reduced energy functional for the magnetization. In particular, this study confirms the expected exponential dependence of the nucleation rate on the effective energy barrier. These results establish Bose-Einstein condensate mixtures as a versatile and well-controlled platform for investigating out-of-equilibrium quantum field theory phenomena. In [12], the dependence of the decay time on the Rabi frequency Ω_R is also investigated. In contrast, the temperature dependence is not explored, as a method to vary the sample temperature in a controlled manner has not been developed; consequently, the temperature remains constant within experimental uncertainties.

The temperature dependence of the decay time in FVD is the topic of this Chapter. Temperature acts as a control parameter for metastable decay, as it modifies the relative weight of thermal versus quantum activation. Here the aim is to experimentally validate the scaling behavior predicted by the finite temperature extension of instanton theory [11, 104]. The Chapter is organized into four Sections. The first Section provides an overview of the instanton theory used to describe tunneling processes in quantum field theory. The second Section introduces the experimental system, discussing the applicability of instanton theory to superfluid analog platforms and the implications of having an harmonic trapping potential, which results in an inhomogeneous density sample. The third Section describes the experimental protocol, including the procedure used to tune and characterize the sample temperature, the preparation of the system in the metastable state, and the methodology employed to extract the decay time τ. The final Section presents the experimental results which are also published in [91].

3.1 Instanton theory

In this Section, we review the essential elements of False Vacuum Decay theory. I begin recalling the standard tunneling mechanism for a quantum particle at zero temperature and then I extend the formalism to quantum field theory. Let us consider a unitary mass particle initially at rest in the metastable minimum of a tilted double-well potential, of the shape $U(x) = \lambda/a^2(x^2 - a^2)^2 + \epsilon a x$ where $U(a) = U_0 > 0$ represented in Fig. 3.2.

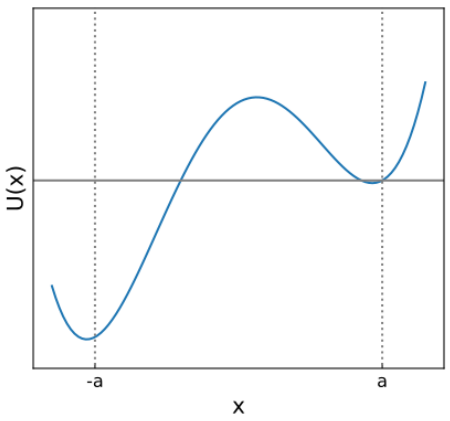

Figure 3.2: Tilted double well potential $U(x)$, with a matestable local minimum at $x = a$ and an absolute ground state at $x = -a$.

Even though it is classically confined, the particle has a finite probability to tunnel through the potential barrier reaching the absolute ground state. This tunneling mechanism is a purely quantum phenomenon. The tunneling probability is given by:

$$P = \langle -a | \, e^{i\hat{H}t/\hbar} \, | a \rangle \tag{3.1}$$

whose characteristic decay width defines the decay rate of the metastable state [108]. Within the semiclassical approximation [109], the rate takes the standard Wentzel-Kramers-Brillouin (WKB) form

$$\Gamma = A\, e^{-B}, \qquad B = \frac{2}{\hbar} \int_{-a}^{a} dx \, \sqrt{2\,[U(x) - U_0]} \tag{3.2}$$

where B corresponds to the Euclidean action accumulated along the classically forbidden trajectory under the barrier.

This framework can be extended to the quantum field case, where the key difference is that now the field itself undergoes tunneling process through the potential barrier, after which it evolves classically. During this process, the system passes from a homogeneous to a non-homogeneous field configuration, implying, for instance, the formation of domain walls.

The following paragraphs present the generalization of a field decay, based on the works of Coleman [10, 103] and its extension to finite temperatures [11, 104], where thermal fluctuations assist the tunneling mechanism and accordingly modify the decay rate.

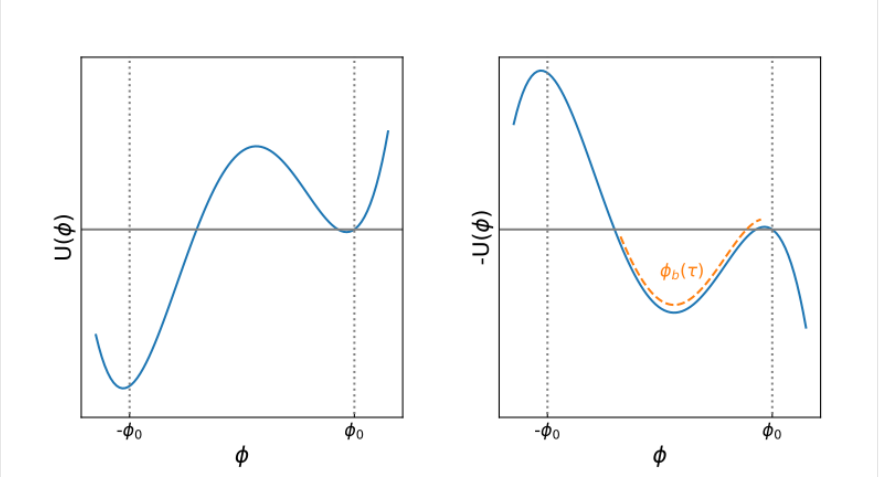

Figure 3.3: (Left panel) Tilted double well potential U(ϕ) with a metastable minimum at $\phi = \phi_0$. (Right panel) Inverted potential after Wick rotation. The orange curve denotes the bounce (instanton) solution $\phi_b(\tau)$.

3.1.1 Zero Temperature Case

In quantum field theory, decay rates can in principle be computed exactly as transition amplitudes from the false vacuum (FV) to a bubble configuration through the path integral formalism. However, the calculation is greatly simplified by performing a Wick rotation to Euclidean time ($it \to \tau$), resulting in a change of the sign of the potential $U(\phi) \to -U(\phi)$, which now depends on the field. Under this transformation the FV is no longer a local minimum of $U(\phi)$, but it becomes an unstable maximum of the inverted potential, as illustrated in Fig. 3.3.

In the Euclidean picture, there exists a classical trajectory (orange dotted line in Fig. 3.3) connecting the FV configuration to a resonant bubble state. This trajectory is the solution of the Euler-Lagrange equation which extremizes the Euclidean action of the inverted potential and it is called the instanton (or bounce) solution. Consequently, the path integral can be approximated with its most relevant contribution, which is the classical trajectory minimizing the Euclidean action.

The instanton solution ϕ_b is obtained by solving the Euclidean Euler-Lagrange equation:

$$\left(\frac{\partial^2}{\partial\tau^2} + \frac{\partial^2}{\partial x^2}\right)\phi_b = U'(\phi_b) \tag{3.3}$$

and the corresponding decay rate acquires the general semiclassical form:

$$\Gamma = Ae^{-(S_E[\phi_b]-S_E[\phi_0])/\hbar} \tag{3.4}$$

where A is a prefactor, typically unknown, which accounts for the leading quantum corrections to the classical instanton solution [103] and the Euclidean action S_E is defined as

$$S_E = \int d\tau dx \left[\frac{1}{2}\left(\frac{\partial\phi}{\partial\tau}\right)^2 + \frac{1}{2}\left(\frac{\partial\phi}{\partial x}\right)^2 + U(\phi)\right] \tag{3.5}$$

The shape of ϕ_b strongly depends on the dimensionality of the system and on the specific form of the potential $U(\phi)$ and, in general, it cannot be computed analytically. However, in the case of 1+1 ϕ^4 theory, with the shape of the potential $U(\phi) = \lambda/(\phi^2 - \phi_0^2)^2 - \epsilon\phi_0\phi$, in the thin wall approximation $\epsilon \to 0$ the instanton solution ϕ_b reduces to a kink-antikink pair shape [110].

$$\phi_b(x) = \tanh(x - b) - \tanh(x + b) \tag{3.6}$$

where $\pm b$ define the spatial boundaries of the bubble.

The spatial gradient of the bounce solution gives a positive contribution in the evaluation of the Euclidean action associated with the energy of the bubble walls. This surface tension term is central in the nucleation mechanism: quantum fluctuations nucleate bubbles of true vacuum, however they are reabsorbed unless the bulk energy gain inside the bubble compensates the cost of wall formation. This requirement sets a critical bubble size. For a small imbalance between the two minima (or for a high potential energy barrier), the critical bubble size increases, and the decay rate becomes exponentially suppressed.

3.1.2 Instanton theory at finite Temperature

The framework discussed so far applies to the zero temperature case. However, in any realistic physical system, the temperature is finite, and thermal fluctuations must be taken into account in the bubble nucleation process. The extension of false vacuum decay to finite temperature was developed by A.D. Linde [111, 11, 104]. Within this formulation, temperature enters the path integral by substituting the Euclidean time with the effective time $\beta = 1/k_B T$. As a consequence, the Euclidean action reduces to $S_E \to \beta S_1$, with

$$S_1 = \int dx \left[\frac{1}{2}\left(\frac{\partial\phi}{\partial x}\right)^2 + U(\phi)\right] \tag{3.7}$$

and the decay rate takes the form

$$\Gamma = A(\beta S_1)^{1/2} e^{-\beta S_1} \tag{3.8}$$

This expression is formally equivalent to integrating the zero-temperature decay rate over all the initial excited states of energy $\epsilon > 0$ above the false vacuum, each state weighted by the Boltzmann factor $e^{-\beta\epsilon}$.

The finite-temperature description is valid as long as thermal fluctuations are significantly larger than quantum fluctuations, but until these fluctuations remain smaller than the instanton energy scale (Panel (b) of Fig. 3.1). In this intermediate regime, bubble nucleation is thermally assisted but still retains a quantum origin. At temperatures higher than the energy associated to the instanton solution bubble formation becomes a purely thermal incoherent process. Conversely, when the temperature is much lower than the interaction energy scale, tunneling is dominated by quantum fluctuations and the decay is well described by the zero temperature instanton formalism.

In all these regimes, the decay rate remains exponentially suppressed as a function of the relevant system parameters.

3.2 Experimental Platform

As anticipated, our experimental platform consists of a coherently-coupled two-component superfluid BEC mixture. In particular, we employ the two hyperfine states $|F = 1, m_F = -1\rangle$ and $|F = 2, m_F = -2\rangle$ of atomic sodium which is robust against spin-exchange collisions and features an immiscible character, leading the system to experience the paramagnetic-to-ferromagnetic quantum phase transition [8]. In the first part of this Section we discuss how the theoretical framework of false-vacuum decay can be generalized to coherently-coupled superfluid mixtures. In the second part, we analyze the spatial inhomogeneity of the condensate phase arising from harmonic confinement, which induces a nonuniform density profile across the cloud and consequently affects the local dynamical parameters governing the decay process.

3.2.1 FVD in ferromagnetic BECs

Instanton theory was introduced to evaluate false vacuum decay rates in cosmological contexts. However, since its derivation does not rely on the relativistic nature of the Lagrangian, the same framework can be also applied to non-relativistic quantum fluids, including BECs. In this context, the calculations become more involved due to the intrinsically non-relativistic nature of the BEC Lagrangian and to the presence of two coupled dynamical fields; the magnetization Z and the relative phase ϕ, rather than a single scalar degree of

freedom. As a result, several approximations are required in order to obtain a tractable expression for the decay rate.

To obtain the effective model for the finite temperature FVD regime discussed above, we begin from the energy functional of the coherently coupled mixture:

$$E = \int \left[\frac{n}{2} \frac{\hbar^2}{4m} \left[\frac{(\nabla Z)^2}{1-Z^2} + (1-Z^2)(\nabla\phi)^2 \right] + \frac{\kappa n}{2} Z^2 - \delta_{\text{eff}} Z - \Omega_R \sqrt{1-Z^2} \cos\phi \right] dx \tag{3.9}$$

here, we have included the kinetic-energy contributions arising from the relative phase and the magnetization gradients, which were omitted in Chapter 1 when discussing the static properties of the mixture. Bubble nucleation, however, necessarily involves the formation of domain walls, and therefore gradient terms provide a non-negligible energy cost, which is absent in the local density approximation (LDA).

The expression above is obtained under the assumption that the total density varies smoothly in space on length scales much larger than density healing length ξ, and that there is no background flow so that the global phase remains spatially uniform. In addition, we have replaced δg with κ to average the transverse inhomogeneity of the experimental sample as discussed in Sec. 1.3.3 when we perform the reduction to one effective dimension.

Within the finite-temperature instanton framework, the decay rate for thermally-activated bubble nucleation takes the form:

$$\Gamma = 1/\tau = A \left(\frac{E_c}{k_B T} \right)^{1/2} e^{-E_c/k_B T} \tag{3.10}$$

where E_c is the energy gain of the field with respect to the potential value in the FV.

To compute E_c, we use the approximation of a spatially constant relative phase $\phi = 0$, leading to an effective single-field theory for the magnetization, where the potential U only depends on magnetization $U(Z, \phi = 0) = U(Z)$. The corresponding expression for the bubble energy reads [12]

$$E_c = \int \frac{n}{2} \left[\frac{\hbar^2}{4m} \frac{(\nabla Z)^2}{1-Z^2} + [U(Z) - U(Z_{FV})] \right] dx \tag{3.11}$$

then we can introduce the dimensionless barrier energy:

$$\hat{E}_c = \frac{E_c}{\hbar n^2 \xi_s |\kappa|} \tag{3.12}$$

where $\xi_s = \hbar/\sqrt{m|\kappa|n}$, and κ is the renormalized interaction strength defined in Sec. 1.3.3.

The spatial profile of the bubble can be obtained by solving the Euler-Lagrange equation in imaginary time for the magnetization field

$$\frac{1}{2}\frac{(\nabla Z)^2}{1-Z^2} = U(Z) - U(Z_{FV}) \tag{3.13}$$

which can be rewritten as

$$\frac{dZ}{dx} = \left[\frac{2(U(Z) - U(Z_{FV}))}{\kappa n}\right]^{1/2} (1-Z^2)^{1/2} \tag{3.14}$$

the corresponding expression for the barrier energy is then

$$\hat{E}_c = \frac{1}{4} 2 \int_{Z_{TP}}^{Z_{FV}} \left[\frac{2(U(Z) - U(Z_{FV}))}{|\kappa| n}\right]^{1/2} \frac{dZ}{\sqrt{1-Z^2}} \tag{3.15}$$

whose analytical expression is in general nontrivial to obtain.

Two opposite limiting regimes are possible in our experimental system. The small detuning regime, in this case the two minima of the potential are nearly degenerate, and the action, thus the decay time, is extremely sensitive to the ratio $\Omega_R/\kappa n$. In this regime the decay time becomes exponentially large, requiring very long coherence times that are difficult to achieve experimentally. The small barrier regime (detuning near the critical value δ_c at which the metastable minimum disappears), where the potential is strongly tilted and the action becomes essentially independent of the ratio $\Omega_R/(\kappa n)$. Moreover, in the small barrier regime, decay times are significantly shorter, making the nucleation process experimentally accessible. In the small-barrier limit, an analytic expression for the instanton energy, only depending on the control parameters, can be derived by expanding the potential to cubic order around the inflection point

$$Z_c = \left(1 - \frac{\Omega_R}{|\kappa| n}\right)^{1/2}, \qquad \delta_{\text{eff}} = \delta_c \tag{3.16}$$

where δ_c is the critical detuning below which the metastable minimum disappears. Then one obtains the scaling law

$$\hat{E}_c \sim 1.77 \left(\frac{\delta_f - \delta_c}{|\kappa| n}\right)^{5/4} \left(\frac{\Omega_R}{|\kappa| n}\right)^{1/6} \left(\frac{|\delta_c|}{|\kappa| n}\right)^{-1/4} \tag{3.17}$$

Note that although the decay rate takes an Arrhenius-like form, the process is not classical. The fluctuations responsible for nucleation are thermal

fluctuations of a quantum field and the barrier energy E_c corresponds to the instanton action, determined by the many-body interaction at $T = 0$. Thus, the temperature enters only through the Boltzmann prefactor, while the underlying mechanism maintains its quantum field nature.

3.2.2 Harmonic Confining Potential

Since our experimental sample is confined in a harmonic trapping potential, its density is inhomogeneous $n \to n(x)$. As a consequence, both the longitudinal and the transverse components of the effective field (both depending on density) acquire a spatial dependence.

Within the Local Density Approximation (LDA), each position x can be associated with a distinct point of the phase diagram, resulting in a spatially varying energetic landscape and, correspondingly, a position-dependent bubble-nucleation rate.

In our experiment, the harmonically trapped condensate exhibits a parabolic integrated density profile shown in upper panel of Fig. 3.4;

$$n(x) = n_0 \left(1 - \frac{x^2}{R_x^2}\right) \tag{3.18}$$

where the effective 1D peak density is $n_0 \sim 4000\ \mu\text{m}^{-1}$ and the Thomas-Fermi radius is $R_x \sim 200\ \mu$m. For sodium, the interaction constants are such that $\Delta = \kappa < 0$ (where we use the definition of $\Delta = \frac{g_{22}-g_{11}}{2}$ introduced in Sec. 1.3.3), implying that the effective detuning felt by the atoms ($\delta_{\text{eff}} = \delta_B + n\Delta$) is reduced with respect to the externally applied one. The coherent coupling, on the other hand, is uniform throughout the cloud, so that both Ω_R and δ are spatially constant. As a result, each point along the axial direction of the condensate corresponds to a different point in the phase diagram shown in the lower panel of Fig. 3.4, in particular the spatially extended superfluid sample is represented as a line with slope $-\Delta/\kappa = -1$ on such a diagram (green line). Varying the external detuning in time, shifts this line vertically, thereby allowing one to span the whole phase diagram [8].

This implies that, by properly choosing the value of Ω and δ, the three relevant phases, paramagnetic, ferromagnetic and saturated-ferromagnetic, can coexist within the same sample as shown in Fig. 3.4 where the sample density profile (only the right half since the other can be obtained for symmetry) and the corresponding free energy at different positions in the cloud are represented. The low-density tails satisfy $\kappa n/\Omega_R < 1$ and are therefore paramagnetic, while the high density central region satisfies $\kappa n/\Omega_R > 1$, giving rise to ferromagnetic core. These two regions are separated by a narrow saturated-ferromagnetic region, defined by ($\kappa n/\Omega_R > 1$ and $|\delta - \Delta n| > |\delta_c|$). The ferromagnetic phase

is characterized by two minima that are not degenerate in the case of finite detuning.

The system occupies the absolute minima when the magnetization has the same sign of the effective detuning. In this case the extended superfluid forms two domain walls at the positions where the effective detuning crosses zero. Conversely, the system is in its metastable minimum (false-vacuum) when the detuning favors a negative magnetization but the condensate occupies the positive-magnetization minimum. In this false-vacuum configuration, domain walls are absent. This absence is the key feature to observe bubble nucleation. If domain walls were present, the system would relax to the true vacuum simply through their motion, preventing the nucleation of isolated bubbles [106].

A further relevant aspect concerns the spatial dependence of the bubble nucleation probability also originating from the inhomogeneous density profile, $n = n(x)$, which affects both the effective detuning δ_{eff} and the ferromagnetic interaction term $\kappa n/\Omega$: for a fixed external detuning, the energy barrier $\hat{E}_c$ becomes position dependent. In particular, the barrier is lower at the center of the trap, where the density is maximal, and increases towards the edges. This spatial variation favors tunneling processes in the central region. As a result, the bubble nucleation probability is peaked around $x = 0$ and exhibits an approximately Gaussian spatial profile whose width decreases by decreasing temperature [9].

3.3 Experimental Protocol

In this Section we describe the experimental protocol used to create the system in the metastable state and to study the relaxation process. In particular, we are interested in the scaling of the decay time τ with the two parameters, the detuning δ, setting the height of the barrier, and the temperature T of the sample in order to decouple the contribution to τ coming from β and E_c, at fixed Rabi frequency Ω. The protocol is similar to the one used in [12], however this work is focused on addressing the model for FVD at finite temperature.

Our protocol is composed of three steps. The first one is the preparation of a partially Bose-condensed sample at a fixed temperature, then, the system is prepared in the metastable ferromagnetic state, and finally we study the relaxation dynamics.

Sample preparation In Chapter 2 all the cooling steps to create the BEC are explained. At the end of the process the atoms in the $|F = 1, m_F = -1\rangle = |\downarrow\rangle$ at a temperature of about $\sim 10\mu K$ are trapped in an elongated optical dipole trap where they experience the last evaporative cooling bringing the

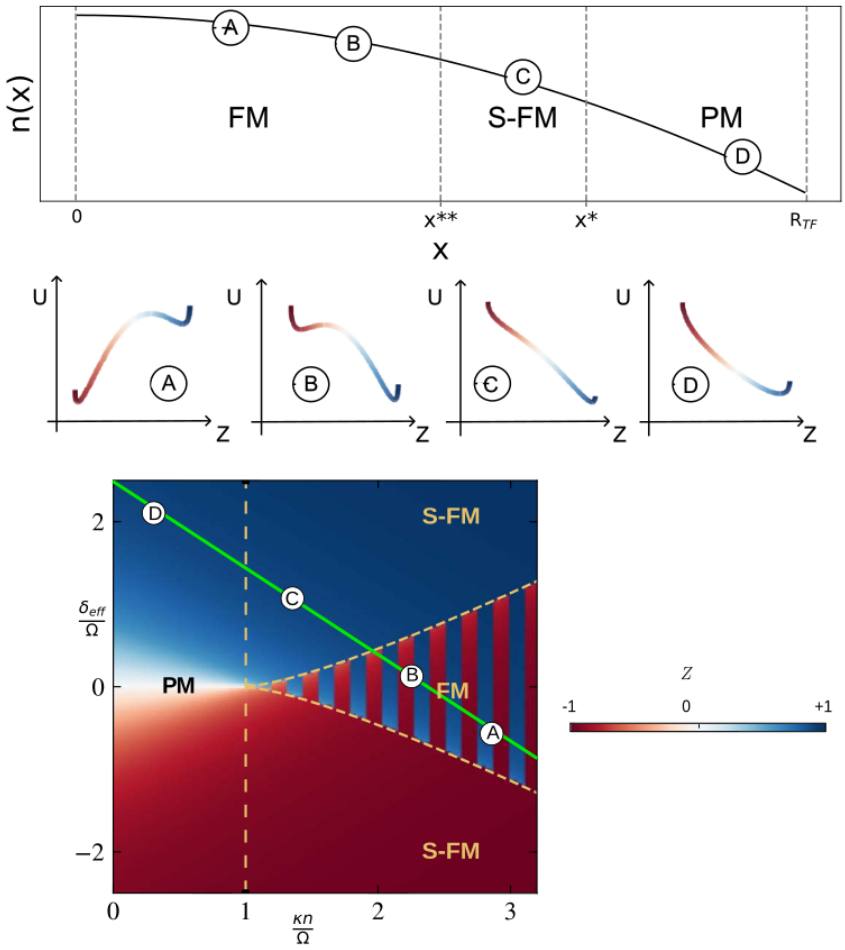

Figure 3.4: (Upper panel) Position-dependent density profile (only one half shown due to symmetry). The point x^* denotes the position at which $\kappa n/\Omega_R = 1$, marking the boundary between the paramagnetic and ferromagnetic phases. The point x^{**} identifies the position such that the effective detuning $\delta_{\text{eff}} = \delta_c$ separating the ferromagnetic region from the saturated-ferromagnetic one (Middle panel) Corresponding position-dependent energy profiles $U(Z)$ for the high density ferromagnetic central part (A,B), saturated ferromagnetic region (C) and low density paramagnetic tail (D), (Lower panel) Magnetic phase diagram. The green line represents an harmonically trapped cloud.

atoms below the threshold temperature required for condensation. The evaporation is obtained by exponentially reducing the optical potential U down to a minimum U_{evap}. After a thermalization of 500 ms the cloud is partially condensed and at thermal equilibrium at T_{exp} which depends on the value of U_{evap}, thus, it is possible to tune the temperature of the sample by varying the final intensity of the optical trap. Then the intensity of the optical trap is ramped to a fixed value $U \sim k_B \times 45\mu\text{K}$ in 500 ms corresponding to an elongated harmonic trap with trapping frequencies in the longitudinal and transverse directions $\{\omega_x, \omega_r\}/(2\pi) = \{15, 2020\}$ Hz. This ensures that the system is always confined in the same optical trap independently from the temperature, with harmonic frequencies such that the system can be considered one dimensional in the spinor degrees of freedom [8, 12, 112]. At the end of this preparation procedure the sample contains about 10^6 atoms in the hyperfine state $|\downarrow\rangle$ at temperatures ranging from 1 to 2.5 μK. These temperatures are larger than the energy scale associated to quantum fluctuations $\hbar|\kappa|n/k_B \sim 50$ nK and an order of magnitude lower than E_c/k_B ($\sim$ few tens of μK mainly due to the energy cost for introducing domain walls delimiting the bubbles in the system). Thus, the decay mechanism is well described by the finite temperature FVD.

Preparation of the metastable ferromagnetic system Once the condensate is prepared at a given temperature T, the magnetization is rotated in the metastable state of the ferromagnetic phase. At first all the atoms are transferred in the $|F = 2, m_F = -2\rangle = |\uparrow\rangle$ state via a resonant 20-μs-long μ-wave π-pulse at $\Omega = 2\pi \times 25$ kHz, which does not introduce any spurious heating. Then, the effective detuning ($\delta_{\text{eff}} = \delta_B + \Delta n$) is tuned to a large positive value $\sim 2\pi \times 4.4$ kHz to reach the saturated ferromagnetic state in the central region of the cloud upon ramping Ω_R to $2\pi \times 300$ Hz in 5 ms. Then we adiabatically ramp down the detuning to a negative final value $\delta_f < 0$ at a rate of 54 Hz/ms. Now the initial state with positive magnetization becomes metastable and the FVD may occur. The left panel of Fig. 3.5 represents the experimental protocol, schematizing the detuning and the Rabi frequency as a function of time, while the right panel of Fig. 3.5 shows the potential profiles as a function of system magnetization in the center of the trap during the ramp in the detuning and the corresponding state of the system.

FVD observation For a given temperature and final detuning δ_f we look at the system evolution by performing spin-selective absorption imaging at variable waiting time t and computing the magnetization. Since bubble nucleation is a stochastic process, many independent measurements are taken for any time t, from which it is possible to extract the probability of bubble nucleation at a

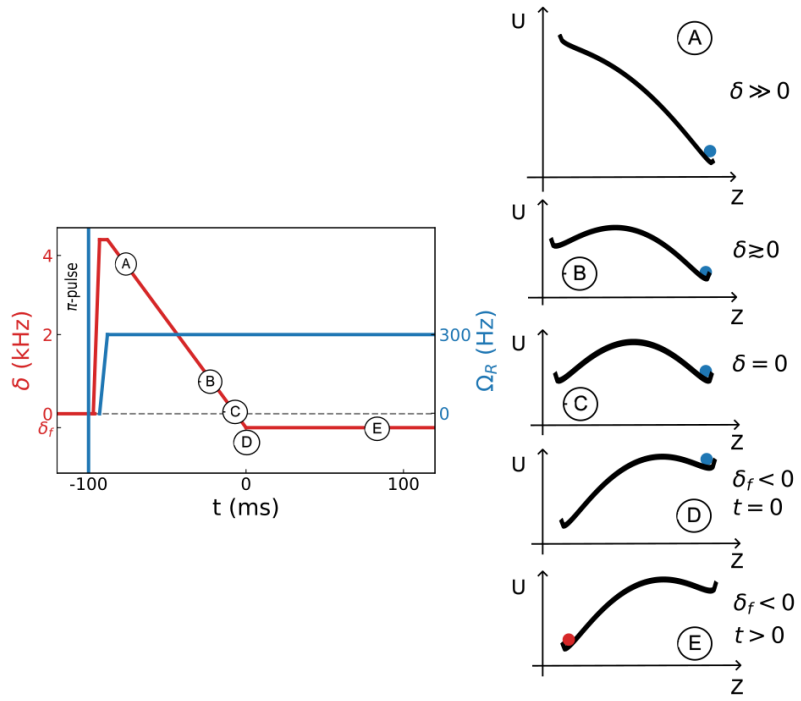

Figure 3.5: (Left) Experimental protocol for the creation of the ferromagnetic metastable state in the center of the cloud and for the observation of the decay towards the ground state. Here, the plot of detuning (red line) and Rabi frequency (blue line) vs time are shown. The detuning is initially ramped to $\sim 2\pi \times 4.4$ kHz, then it is ramped down to a negative final value $\delta_f < 0$. (Right) Potential profiles and system magnetization in the center of the trap, for different values of detuning and waiting time.

given time and the decay time τ. The experiment is then repeated for different final detunings at a fixed temperature and then the same measurements are performed preparing the system at different temperatures.

3.4 Data Analysis

3.4.1 Image acquisition and analysis

The images of the two states are taken along the vertical direction through absorption imaging as explained in Sec. 2.3. Due to the different time of flight and the tight radial confinement, the radial distributions of the two spin states are different, the one for the $|\uparrow\rangle$ component is narrower than the one for the $|\downarrow\rangle$ component. This effect is accounted for in postprocessing by stretching the radial direction of the optical density (OD) of $|\uparrow\rangle$ to match the radial distribution of the $|\downarrow\rangle$ (Panels (a) and (b) of Fig. 3.6). The expansion in the longitudinal direction can instead be neglected since the axial dynamics during the time of flight is negligible when compared to the typical spatial magnetic structure along the axial direction. Moreover, the acquired OD contains information about both the condensate and the thermal fraction; however, the spin dynamics of the thermal gas is different from that of the superfluid mixture; thus, it is fundamental to remove the thermal component and include only the condensate contribution for the calculation of the magnetization. This is done by first fitting the total OD with a 2D bimodal function containing both the condensate and the thermal components:

$$n_{0,B}(x,y) = n_{0,B}\max\left\{\left[1-\left(\frac{x-x_{0,B}}{R_x}\right)^2-\left(\frac{y-y_{0,B}}{R_y}\right)^2\right]^{3/2},0\right\} \tag{3.19}$$

$$n_{0,th}(x,y) = n_{0,th}g_2\left\{\exp\left[-\frac{1}{2}\left(\left(\frac{x-x_{0,th}}{\sigma_x}\right)^2+\left(\frac{y-y_{0,th}}{\sigma_y}\right)^2\right)\right]\right\} \tag{3.20}$$

From Eqs. 3.19 and 3.20 it is possible to identify the region occupied by the condensate which is delimitated by the Thomas-Fermi radii R_x, R_y. Then we treat differently the thermal component inside and outside the condensate region (Panel (c) of Fig. 3.6). The component outside the condensate is identified by fitting for each spin state the thermal component $n_{\rm th}(x,y)$ to the OD in the region outside the ellipse delimitated by R_x and R_y. While inside the ellipsoide occupied by the BEC, the thermal component is depleted and

its integration along the line of sight provides a flat contribution [8]. Given the different locations of the centers of the thermal and the condensed parts (arising from fluctuations of the trapping beam focal position which causes the condensate to oscillate in the trap, due to its superfluid nature, whereas the thermal component does not follow this motion) we consider the inner thermal component as a plane tilted along the x-axis, which interpolate between the values of Bose function n_{th} at $(x, y) = (x_{0,B} \pm R_x, 0)$. The reconstructed thermal profiles in the outer and inner regions are then separately subtracted from the ODs of the two states , allowing us to obtain the BEC densities $n_\downarrow$ and $n_\uparrow$. From them we can obtain the total density $n(x) = n_\uparrow + n_\downarrow$ and the magnetization $Z(x) = (n_\uparrow - n_\downarrow)/(n_\uparrow + n_\downarrow)$, after integration of $n_\downarrow$ and $n_\uparrow$ along the y direction. Panel (d) of Fig. 3.6 shows the integrated total density, where the thermal component is highlighted in orange. Panel (e) of Fig. 3.6 shows the total condensed distribution obtained subtracting the thermal contribution from the total integrated density.

The integrated density is fitted through a 1D Thomas-Fermi profile

$$n(x) = n_{1D}(1 - (x - x_0)^2/R_x^2)^2 \tag{3.21}$$

Whose fitting parameters can be used to calculate the spin interaction energy

$$\kappa n(x) = \frac{2}{3}\left(\frac{g_{\downarrow\downarrow} + g_{\uparrow\uparrow} - 2g_{\uparrow\downarrow}}{2\hbar}\right) n_0^{3D}\left(1 - \frac{x^2}{R_x^2}\right) \tag{3.22}$$

with g_{ij} the interaction constants between the states $|i\rangle$ and $|j\rangle$ and $n_0^{3D} = 15N/(8\pi R_x R_r^2)$ the 3D peak density of a sample of N atoms. This expression implies that κn is proportional to the 3D peak density of the condensate even if it is distributed as a 1D Thomas-Fermi profile. This is the consequence of dimensionality reduction, under the assumption of spin radial dynamics suppression, as discussed in Sec 1.3.3. The result is $|\kappa|n \approx 1$ kHz.

This value for κn has been obtained by extracting the N value from the fit result, exploiting the expression

$$n_{1D} = \frac{15}{16}\frac{N}{R_x} \tag{3.23}$$

coming from the integration of the density of a 3D condensate along two orthogonal lines of sight, and independently measuring the two trapping frequencies, in order to obtain the trap aspect ratio as $\omega_x/\omega_r = 0.0075$. The information can be used to obtain $R_r = R_x\omega_r/\omega_x$ which is not directly measurable within the optical resolution of our imaging system.

Then, the value of κn can be used to calculate the spin healing length,

$$\xi_s = \sqrt{\frac{\hbar}{2m|\kappa|n}} \tag{3.24}$$

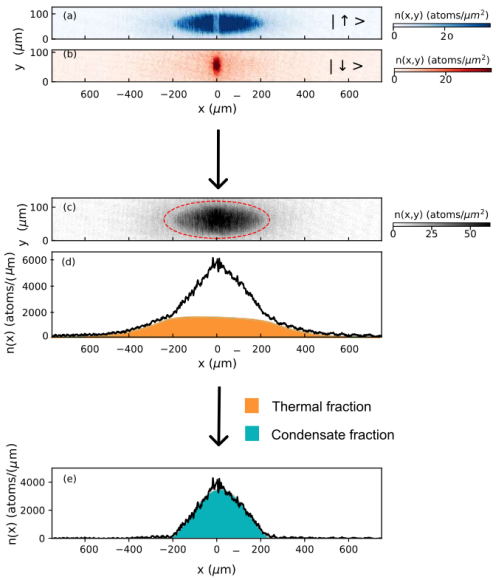

Figure 3.6: Two dimensional optical densities (ODs) of the $|\uparrow\rangle$ state (a) and $|\downarrow\rangle$ state (b). Panel (c) shows the total two-dimensional OD, obtained as the sum of the two contributions and fitted with a 2D bimodal function. The red dashed line indicates the boundary between the inner Bose.Einstein condensate (BEC) region and the outer thermal component, as determined from the fit. Panel (d) shows the radially integrated total OD, $n(x)$, extracted from the two-dimensional density distribution shown in (c); the thermal component obtained from the fit is highlighted in orange. Panel (e) shows the total density after the thermal part has been removed.

In our system $\xi_s \approx 0.5$ μm, yielding $\xi_s \lesssim R_r$. Therefore, although the spin profile is effectively one-dimensional, the system cannot be regarded as an ideal one-dimensional system. As already reported in [8], the experimental results are in qualitative agreement with 1D theoretical predictions, however, a quantitative mismatch persists.

Uncertainties on $|\kappa|n$, n_{1D} and ξ_s are determined a posteriori from the standard deviations over the different experimental realizations at fixed δ_f and Ω_R where no bubble is detected.

3.4.2 Decay time determination

Information on the decay time τ can be extracted from the magnetization of the system by averaging over multiple realizations at fixed values of T_{exp} and δ_f, thereby identifying the emergence of spin bubbles at a given time t. In particular, τ is extracted by evaluating the FV survival probability [107]

$$F_t = (\langle Z \rangle_t - Z_{TV})/(\langle Z \rangle_0 - Z_{TV}) \tag{3.25}$$

Where $\langle Z \rangle_t$ is the magnetization spatial average in the central 60 μm over several realizations at time t while Z_{TV} is the magnetization of the true vacuum state. Due to decoherence and the magnetic excitations injected in the system upon relaxation, the exact value of Z_{TV} does not corresponds to the theoretical one. However, under the assumption that the system is well initialized in the FV state: $\langle Z \rangle_0 = \langle Z \rangle_{FV}$, and that the false and the true vacuum correspond to opposite magnetization, $Z_{TV} = -\langle Z \rangle_0$, we introduce the observable

$$F_t = \frac{1}{2}\left(1 + \frac{\langle Z(x) \rangle_t}{\langle Z(x) \rangle_0}\right) \tag{3.26}$$

which we fit with the phenomenological function

$$F_t^{\text{fit}} = \frac{1-\epsilon}{\sqrt{1 + (e^{t/\tau} - 1)^2}} + \epsilon \tag{3.27}$$

where the parameter ϵ is introduced to take into account the minimum magnetization observable in the experiment.

The magnetization is then averaged for each set of $(\delta_f - \delta_c)$ and temperature T_{exp} by grouping the experimental realizations in 10 equally spaced intervals. For each pair of values δ_f and T_{exp}, $\langle Z \rangle_0$ is obtained from the average magnetization over all experimental realization without bubbles.

3.4.3 Calibrations

Temperature measurements Single-shot absorption images provide information on both thermodynamic and interaction properties of the system. In particular, the density profiles allow to extract the experimental temperature $T_{\rm exp}$ and the interaction energy scale $|\kappa|n \sim 2\pi \times 1$ kHz for each experimental realization. The latter is determined from the condensate density and then used to evaluate the critical detuning $\delta_{\rm c}$, whereas the temperature is obtained by analyzing the thermal component of the atomic cloud.

Temperature estimation is performed independently for each data set acquired at fixed $(\delta_f - \delta_{\rm c})$. Only images showing no signature of bubbles nucleation are included in the analysis. For a given realization, the total optical density along the radial direction y is evaluated at three axial positions located just outside the Thomas-fermi radius of the condensate, namely at $x_T/R_x = 1.02, 1.10, 1.15$ as shown in the upper panels of Fig. 3.7. At each position, the resulting one-dimensional density profile is fitted with an integrated Bose distribution, yielding the width $\sigma(x_T)$ of the thermal cloud. Since the axial confinement is not uniform along the axial direction, the corresponding local radial trapping frequency $\omega_r(x_T)$ is computed by modeling the Gaussian propagation of the optical trapping beam.

The temperature $T_{{\rm exp},i}$ associated with the i-th experimental realization is then obtained by averaging the three local temperature estimates,

$$T_{{\rm exp},i} = \frac{1}{3}\sum_{x_T} \frac{m\sigma^2(x_T)}{k_B} \frac{\omega_r^2(x_T)}{1+\omega_r^2(x_T)t_{\rm tof}^2} \tag{3.28}$$

where $T_{\rm tof}$ denotes the time of flight between trap release and image acquisition.

For a given decay time τ, the reported temperature $T_{\rm exp}$ is calculated as the mean of the corresponding set of $T_{{\rm exp},i}$, while the associated uncertainty is quantified by their standard deviation.

Since the system is prepared through an adiabatic ramp, density and magnetization fluctuations are expected to equilibrate during the preparation stage. Under this assumption, the same temperature can be assigned to both degrees of freedom. Experimentally, this picture is supported by the observation that the measured temperature remains unchanged as a function of the waiting time, as long as the system does not undergo decay from the false vacuum state, as it is shown in the lower panel of 3.7, where the estimated temperature is plotted as a function of the waiting time for two different experimental sequences with different values of the bottom of the trap.

This single-shot thermometry is consistent with standard TOF expansion measurements, avoiding the need for additional calibration runs or independent thermometric procedures.

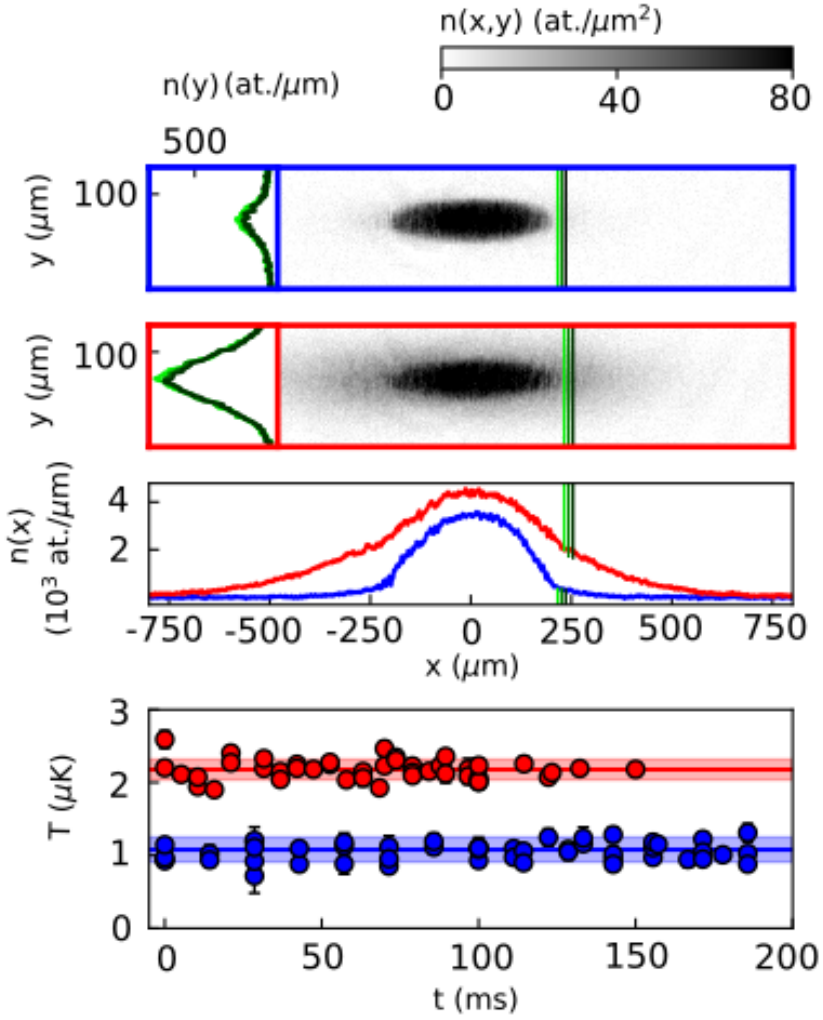

Figure 3.7: Extraction of the sample temperature. (Upper panels) absorption images of a cold (blue) and hot (red) atomic clouds prepared in the $|2,-2\rangle$ internal state, together with the corresponding vertical atomic density distributions evaluated at three axial positions located beyond the Thomas-Fermi radius (indicated by green lines). At each position thermal tails are fitted with a Bose distribution, yielding three independent temperature estimates that are subsequently averaged to obtain T_{exp} for a single experimental realization. (Lower panel) time evolution of the normalized sample temperature for two datasets characterized by sufficiently long decay times τ. The extracted average temperatures are 1.1(2) μK for the blue data points and 2.2(1) μK for the red data points.

Critical detuning Bubble nucleation provides the mechanism through which the metastable ferromagnetic mixture relaxes towards the true vacuum. The characteristic decay timescale depends on the separation between the final detuning δ_f and the critical detuning δ_c. An accurate analysis of the decay dynamics therefore requires an accurate determination of both the zero detuning condition and the location of the critical point.

The critical detuning δ_c cannot be obtained from theoretical predictions derived for ideal one-dimensional systems, giving the exact dependence of the critical point on $|\kappa|n$ and the Rabi coupling Ω_R, since such a description is not valid to a quasi-one-dimensional condensate as shown in [8]. For this reason δ_c is identified empirically as the detuning at which the local metastable minimum of the effective potential $V(Z)$ disappears resulting in the immediate appearance of the $|\downarrow\rangle$ component of the spin distribution.

To locate this threshold, the longitudinal magnetization $Z(x)$ is probed immediately after the state preparation, using the same detection protocol employed in the decay measurements, repeating the measurement for several values of the final detuning δ_f. An example of measurement is shown in Fig. 3.8, where each row of the plot corresponds to the measured 2D magnetization integrated along the y direction for a specific value of the detuning. The scale color goes from dark red when all the atoms are in the $|\downarrow\rangle$ state ($Z = -1$) to dark blue, when al the atoms are in the $|\uparrow\rangle$ state ($Z = +1$). Here δ_c denotes the value of the detuning for which we can observe the appearance of a bubble of true vacuum even at zero waiting time.

Averaging over tens of such experimental realizations, a clear linear scaling of the critical point with the interaction energy $|\kappa|n$ within the experimentally accessible range is revealed. For a fixed Rabi coupling $\Omega = 2\pi \times 300$ Hz, the data are well described by

$$\delta_c = 0.35|\kappa|n + 2\pi \times 28\text{Hz} \tag{3.29}$$

This experimentally determined relation allows δ_c to be determined for each false vacuum decay (FVD) measurement, based on the corresponding value of $|\kappa|n$ extracted from the density profiles (as explained in Sec. 3.4.1). No systematic variation of δ_c with the sample temperature T_{exp} is observed.

The absolute zero of detuning of the non interacting atoms is established independently via Rabi spectroscopy performed on a thermal cloud. This calibration procedure is carried out both before and after each experimental sequence to compensate for slow temporal drifts. Once the reference is set, the final detuning δ_f is adjusted to explore different regimes of the decay dynamics. The uncertainty on δ_f is dominated by the finite resolution of the Rabi spectroscopy, approximately $2\pi \times 5$ Hz, together with residual magnetic

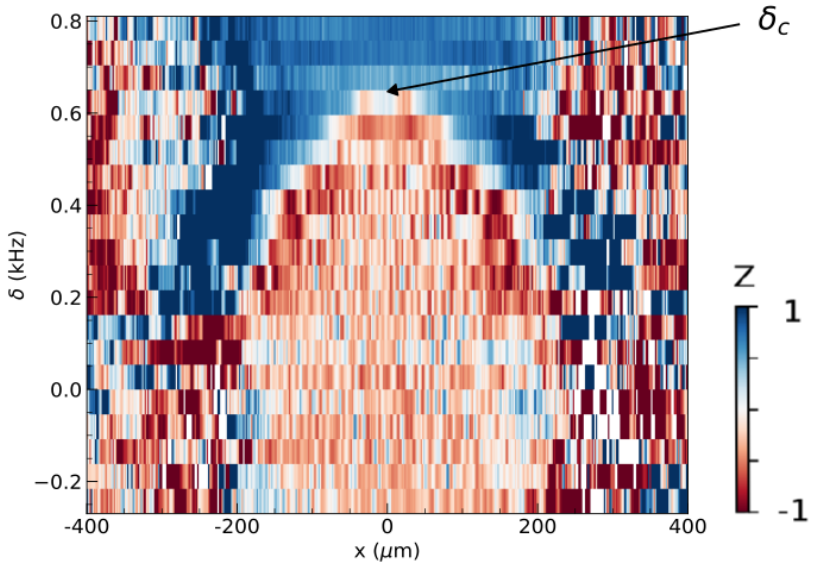

Figure 3.8: Critical detuning measurement δ_c. Each line of the plot corresponds to the integrated profile of the magnetization $Z(x)$ acquired at a certain value of the final detuning with zero waiting time after the end of the ramp. The measurement is performed at a Rabi frequency of $\Omega_R = 2\pi \times 300$ Hz over a condensate at a temperature around 2 μK. The arrow points the value of the detuning at which the first bubble with negative magnetization is observed.

field fluctuations of comparable magnitude.

Taking all contributions into account, the uncertainty on the effective detuning distance from criticality $\delta_f - \delta_c$ is estimated to be of order $2\pi \times 20$ Hz .

3.5 Results

3.5.1 Measurement of Decay Time

The decay time of the metastable configuration is extracted from the temporal evolution of the system magnetization measured after the end of the ramp. Two representative examples of the experimental data are shown in the two upper panels of Fig. 3.9, where the 1D system magnetization is reported for increasing waiting time t after the end of the detuning ramp. Each of these panels refers to a different temperature regimes while the control parameter is kept approximately constant at $(\delta_f - \delta_c)/2\pi = 60$ Hz. In particular, the left panel corresponds to a colder sample with $T_{\rm exp} \simeq 1.4$ μK, whereas the right panel shows data obtained at a higher temperature, $T_{\rm exp} \simeq 2.3$ μK.

The procedure employed to determine the decay time τ is illustrated in the lower panel of Fig. 3.9. For each magnetization profile displayed in the upper panels, the survival probability F_t of the ferromagnetic vacuum state is computed. The resulting values are shown as discrete data points, with blue and red markers corresponding to the colder and hotter samples, respectively. The experimental data are then fitted using the empirical functional form (3.28), and the corresponding fit curves are represented by dotted lines.

A clear dependence of the decay dynamics on temperature emerges from this analysis. In particular, increasing the temperature leads to a faster reduction of the survival probability, indicating an earlier formation of $|\downarrow\rangle$ domains (bubble) within the system. This behavior translates in a shorter decay time τ for the higher- temperature datasets, highlighting the role of thermal effects in accelerating the decay of the ferromagnetic metastable configuration.

3.5.2 Temperature dependence of FVD

The analysis procedure described above has been systematically applied to the full set of experimental measurements, allowing us to extract the decay time τ as a function of both the control parameter $(\delta_f - \delta_c)$ and the experimental temperature $T_{\rm exp}$. The data have been grouped into seven distinct clusters corresponding to different temperature intervals. The resulting temperature distribution is shown in the histogram reported in the upper panel of Fig.

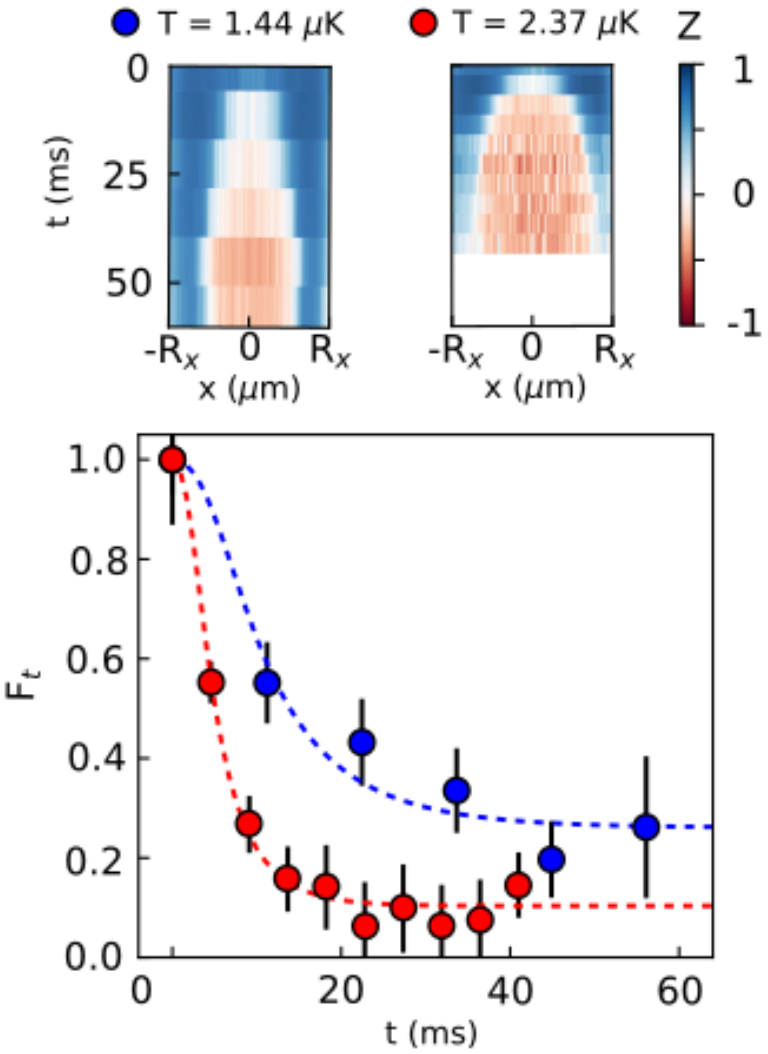

Figure 3.9: Upper panels: time evolution of the system average magnetization $\langle Z(x)\rangle$ for increasing waiting times after the end of the detuning ramp. Two temperature regimes are shown at comparable values of the control parameter, $(\delta_f - \delta_c)/2\pi \simeq 60$ Hz, with $T_{\rm exp} = 1.4(1)$ μK (left) and 2.3(1) μK (right). Lower panel: survival probability F_t of the ferromagnetic vacuum state extracted from the corresponding magnetization profiles. Dots indicate experimental data, while dotted lines show fits to the empirical decay model. Error bars denote the standard error of the mean magnetization.

3.10, where a color scale ranging from dark blue (coldest sample) to dark red (hottest sample) is used to label each cluster.

The corresponding decay times τ are shown in the lower panel of Fig. 3.10 as a function of the normalized control parameter $(\delta_f - \delta_c)/|\kappa|n$. For all temperature clusters, the decay time is observed to rapidly increase as $(\delta_f - \delta_c)/|\kappa|n$ grows, reflecting the progressive reduction of the energy imbalance between the two competing vacua. In addition, a clear temperature dependence emerges: colder samples exhibit a steeper increase of τ compared to hotter ones. This behavior is consistent with the expectation that higher temperatures, associated with stronger thermal fluctuations, enhance the ferromagnetic vacuum decay (FVD) mechanism and therefore lead to shorter decay times as predicted by Eqs. 3.9 and 3.11.

It is now convenient to rewrite the expression for the instanton energy E_c in the form

$$E_c = (\hbar|\kappa|n)(n_{1D}\xi_s)\left(\frac{\delta_f - \delta_c}{|\kappa|n}\right)^{5/4}\left(\frac{\delta_c}{|\kappa|n}\right)^{-1/4}\mathcal{G} \tag{3.30}$$

where $n_{1D} \simeq 5 \times 10^9$ atoms/cm is the one-dimensional atomic density at the center of the trap, $\xi_s = \sqrt{\hbar/2m|\kappa|n} \approx 0,5\mu$m is the spin healing length, m the atomic mass and $\mathcal{G} = \mathcal{G}(\Omega/|\kappa|n)$ is a dimensionless function of the ratio between the Rabi frequency and the interaction energy scale.

The explicit functional form of $\mathcal{G}$ is not accurately known, as discussed in [12] where the precise dependence of the decay time τ on the ratio $\Omega/|\kappa|n$ was found to be inconsistent among numerical simulations, experimental observations and instanton-based theoretical predictions. In the present experiment, however, the Rabi frequency Ω_R is kept fixed, and the parameter $|\kappa|n$ does not exhibit a significant dependence on the sample temperature. Under these conditions, the contribution of $\mathcal{G}$ can be factorized by introducing the reduced instanton energy $\epsilon_c = E_c/\mathcal{G}$, which can be analytically computed from the experimental parameters. In terms of the reduced energy, the decay time can be expressed through a relation formally analogous to Eq. 3.11

$$\tau = A\frac{e^{b\epsilon_c}}{\sqrt{b\epsilon_c}} \tag{3.31}$$

where $b = \mathcal{G}/k_BT$. Since $\mathcal{G}$ does not depend on temperature under our experimental conditions, $1/b$ is expected to scale linearly with T.

Fig. 3.11 shows the decay times τ, extracted for each temperature cluster as a function of the reduced instanton energy ϵ_c. In the evaluation of ϵ_c the residual variation of $|\kappa|n$ is properly taken into account.

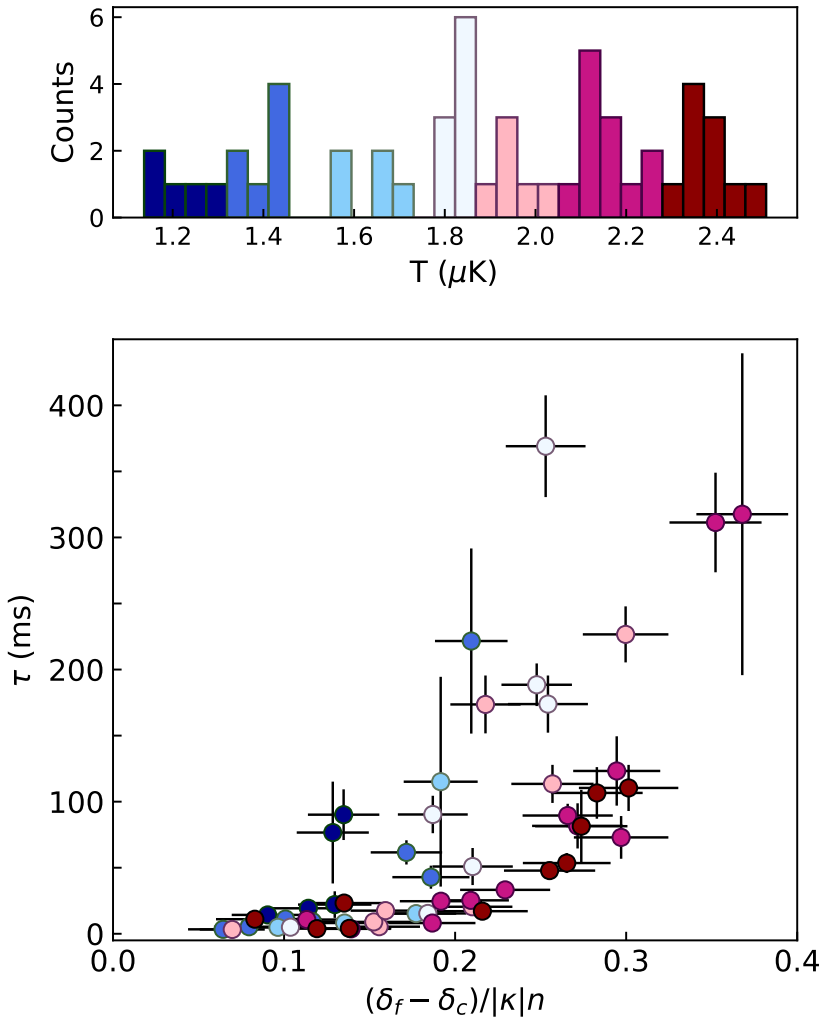

Figure 3.10: Upper panel: histogram of the seven temperature clusters used in the analysis, with colors ranging from dark blue (coldest samples) to dark red (hottest samples). Lower panel: Measured decay time τ as a function of the normalized control parameter $(\delta_f - \delta_c)/|\kappa|n$. Colors indicate the temperature cluster associated with each data point. Each point is obtained from approximately one hundred experimental realizations. Error bars include experimental uncertainties on $(\delta_f - \delta_c)$ and $|\kappa|n$ as well as fitting uncertainties on τ.

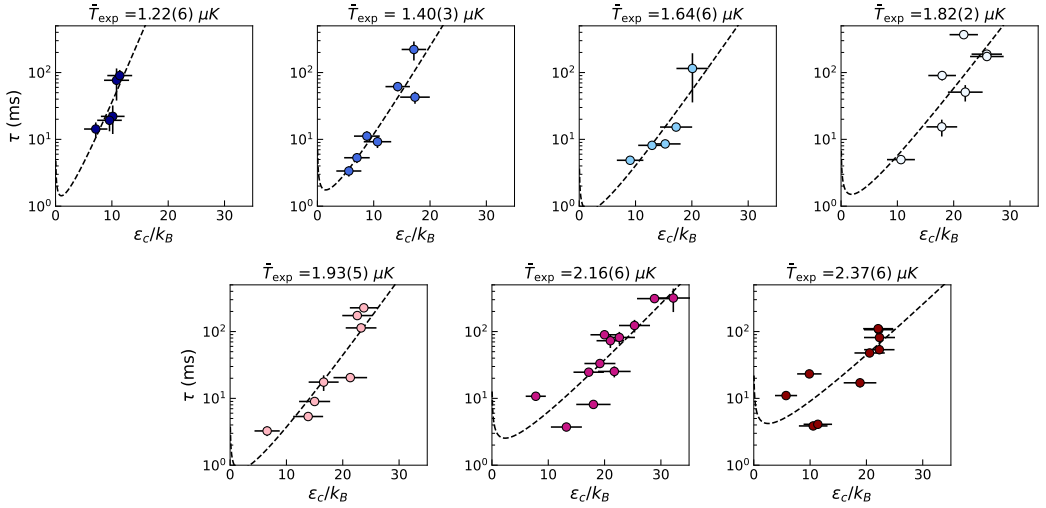

Figure 3.11: Measurement of the FV decay time τ as a function of the rescaled instanton energy, expressed in units of k_B for different experimental temperatures (indicated in each panel). Dashed lines represent fits to the data based on the instanton model.

The experimental data are fitted using a logarithmic form equivalent to Eq. 3.31

$$\ln(\tau) = b\epsilon_c + \ln(a) - \frac{1}{2}\ln(b\epsilon_c) \tag{3.32}$$

where a and b the only fitting parameters.

3.5.3 Temperature dependence of a and b

In principle, the procedure introduced in Sec. 3.5.2 allows us to determine the temperature dependence of the fitting parameters a and b.

When data of Fig. 3.11 are displayed on a linear-logarithmic scale, both the experimental points and the corresponding fit curves exhibit an approximately linear trend at large values of ϵ_c/k_B. The slope of such a linear behavior decreases sistematically while increasing the temperature of the sample $T_{\rm exp}$. This trend is consistent with the definition of τ: in the regime of large βE_c, the exponential contribution dominates over the denominator, leading to the observed quasi-linear behavior in the lin-log representation.

The quantity $1/bk_B$ extracted from the fits is plotted as a function of the measured temperature $T_{\rm exp}$ in the upper panel of Fig. 3.12. The data display a clear linear dependence, in agreement with theoretical expectations that the

thermally activated FVD rate increases exponentially with temperature. A linear fit yields

$$1/bk_B = 2.02(7) \times T_{\text{exp}} \tag{3.33}$$

providing quantitative confirmation of the predicted thermal scaling [11, 104].

In contrast, the prefactor a shows no significant dependence on temperature. As reported in the lower panel of Fig. 3.12, the fitted values are compatible, within experimental uncertainties, with a constant value $a = 0.8(4)$ ms.

The robustness of this approach was tested by repeating the analysis by varying the number of temperature clusters used in the fitting procedure from six to eight. In all cases, the linear dependence of $1/(bk_B)$ on T_{exp} and the temperature independence of a were preserved within uncertainties.

The absence of any additional temperature dependence in the prefactor a indicates that the decay time τ data collapse onto a single curve if plotted as a function of $\epsilon_c/k_B T_{\text{exp}}$ as shown in Fig. 3.13.

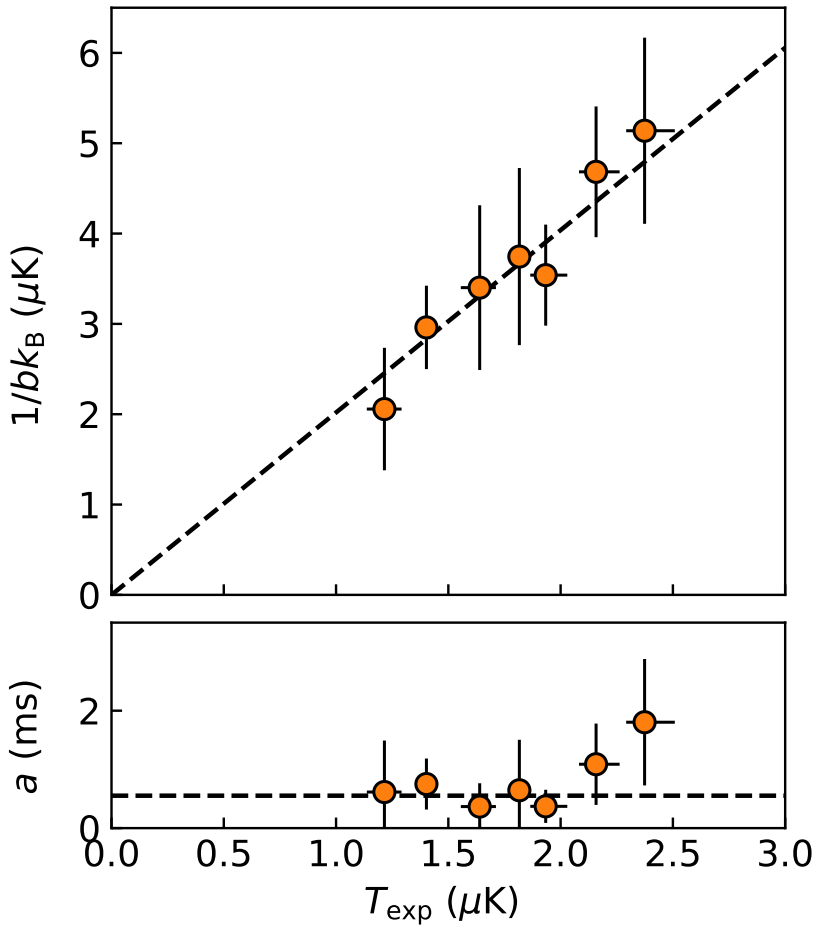

Figure 3.12: Upper panel: Values of $1/bk_B$ extracted from the fits as a function of the measured atomic temperature T_{exp}, showing a clear linear dependence. The horizontal error bars correspond to the minimum and maximum temperatures within each cluster, while the vertical error bars arise from the fitting uncertainty on b. Each point is centered at the mean value of T_{exp} within the corresponding cluster. The solid black line represents the linear fit. Lower panel: Fitted values of prefactor a as a function of T_{exp}. Within experimental uncertainties, no systematic temperature dependence is observed: the data are compatible with a constant mean value of $a = 0.8(4)$ ms.

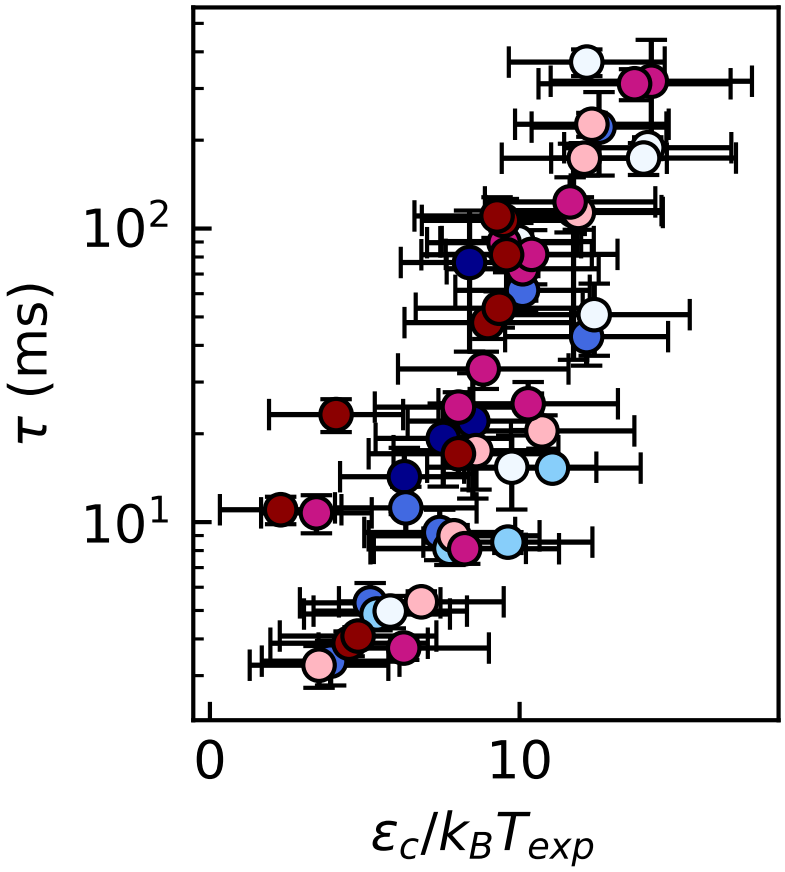

Figure 3.13: Collapse of the data onto a single curve when plotted as a function of the dimensionless parameter $\epsilon_c/k_BT_{\text{exp}}$

Chapter 4

Towards zero magnetic field environment for spinor superfluids

The precise control and characterization of magnetic fields is a fundamental requirement in a wide range of applications in experimental physics. While so far we focused on experiments where magnetic field stability was the primary concern, there exists a broad class of applications in which not only stability but also the absolute magnitude of the field plays a crucial role, and it is often necessary to reduce the field below a well-defined threshold. Representative examples include biomedical imaging techniques [113, 114], zero-field nuclear magnetic resonance [115, 116], metal detection [117, 118] and material characterization [119]. These applications have motivated the development of highly sensitive magnetometric techniques capable of operating in regime of extremely weak magnetic fields.

The measurement of weak magnetic fields has usually relied on superconducting quantum interference devices (SQUIDs) operating in cryogenic environments [120]. Alternative approaches based on atomic coherence in room temperature vapor cells [121, 122, 123] or atomic spin alignment [124] have been extensively developed. Recently, further experimental platform and techniques were made available [125], further expanding the range of accessible magnetic field sensitivities and spatial resolution.

In the context of ultracold atomic physics, cold gases have emerged as promising magnetic field sensors [126, 127], also exploiting the high sensitivity of spinor Bose-Einstein condensates to magnetic field inhomogeneities [128]. In particular, the ability to minimize and control magnetic fields opens the door to the investigation of new physical regimes of these systems. In particular, it enables the exploration of zero magnetic field physics in spinor condensates,

whose vector order parameter leads to a rich variety of ground state configurations [5, 18].

As discussed in Chapter 1 for the case of a $S = 1$ spinor condensate, the ground state depends on the competition between spin-dependent interaction energies and the external magnetic field, which lifts the degeneracy between different spin states [5]. Under the conditions of nonzero and fixed magnetization, spatially extended spinorial systems have been studied in the presence of a well defined magnetic field [129]. Conversely, the complementary regime, in which the system evolves in the absence of an external magnetic field, is yet largely unexplored with superfluids.

The regime, in which magnetic and interaction energies are comparable, has been studied using dipolar chromium gases in the presence of magnetic fields on the order of a few tenths of milligauss, enabled by the large magnetic dipole moment of chromium atoms [130]. In contrast, for ultracold gases of alkali-metal atoms, long-range magnetic dipole-dipole interactions are typically weak, around 36 times smaller than for chromium atoms [131], making the spin dependent interaction dominated by spin contact interactions. As a consequence, the magnetic field threshold below which novel spinor phases are expected is significantly reduced compared to the chromium case [5, 42, 132, 19]. Within the zero spatial mode approximation, this threshold is predicted to be of the order of a few hundreds of microgauss, and it is expected to be even lower for spatially extended condensates.

To address the topic of high-precision magnetic field control, the challenge lies in achieving and maintaining magnetic field stability and homogeneity at the microgauss level across the entire spatial extent of the atomic sample, both during a single experimental run and across repeated measurements. Moreover, conventional spectroscopic methods for magnetic field characterization, as discussed for instance in Chapter 2, become ineffective in the weak field regime. These spectroscopic method rely on resolving Zeeman-shifted transitions in a two level system using radio frequency and microwave radiation. While this approach is effective at sufficiently large magnetic fields, where the Zeeman splitting ($\approx$ 1.4MHz/G for atomic ^{23}Na) greatly exceeds the resonance linewidth, it fails in the microgauss regime, where the Zeeman structure is no longer resolved and the polarization of the driving field is generally not well-defined.

To overcome these limitations, this Chapter presents an experimental technique for magnetic field characterization and minimization exploiting the atoms as magnetic field sensors. This approach is particularly advantageous since the integration of a magnetometer inside the vacuum chamber is not realistic. The method is based on Landau-Zener spectroscopy [133] over an atomic gas of

sodium, and it exploits controlled ramps of the z-component of magnetic field amplitude and direction to probe the adiabaticity of the atomic spin dynamics.

Landau-Zener theory provides a powerful framework for magnetic field characterization. Here, two complementary protocols are developed: one for minimizing the magnetic field components in the transverse plane, and one for minimizing the field along the longitudinal z-axis. I will show that applying Landau-Zener (LZ) spectroscopy to a gas of sodium atoms [133], we achieve magnetic field minimization at the 10 μG level [134].

The Chapter is organized in three Sections. The first one describes the theoretical framework over which our protocol is based. The second one contains a description of the experimental protocols used for characterizing both the longitudinal and the transverse field, while the last Section discusses the experimental results.

4.1 Landau-Zener Spectroscopy

The Landau-Zener formalism provides a powerful framework for describing transitions in driven quantum systems and has been extensively employed in a wide variety of physical contexts ranging from molecular physics to nuclear collisions [135, 136] and semiconductors impurities [137]. It was originally introduced by Landau and Zener in 1932 to describe non-adiabatic transitions in two-level systems [138].

Assuming the system is initially prepared in a well-defined quantum state at large negative time, and assuming the existence of a second state such that the energy detuning between the two states varies linearly in time, the Landau-Zener model allows one to compute the probability for the system to remain in the initial state at large positive times.

This framework can be extended to describe three levels system with two distinct transitions and time dependent detunings, assuming that the two excited states are unoccupied at sufficiently large negative time. The solution of the three-level Landau-Zener problem can be constructed by decomposing the dynamics into two effective two-level transitions as shown by Atabek in [139].

The dynamics of the $F = 1$ hyperfine ground state of sodium, in the presence of a time-dependent magnetic field can be conveniently described within the Landau-Zener framework by a three component wave function

$$\vec{\Psi} = (\psi_{-1}, \psi_0, \psi_{+1}) \tag{4.1}$$

whose time evolution is governed by the Hamiltonian

$$H(t) = g_F \mu_B \begin{pmatrix} \alpha t & \Delta & 0 \\ \Delta & 0 & \Delta \\ 0 & \Delta & -\alpha t \end{pmatrix}. \tag{4.2}$$

where $g_F = -1/2$ is the Landé factor of the $F = 1$ hyperfine ground state, μ_B is the Bohr magneton and $\Delta = B_\perp/\sqrt{2}$ acts as a coupling between the states and defines the gap between the energy levels induced by the transverse component of the magnetic field $B_\perp = \sqrt{B_x^2 + B_y^2}$. The parameter α characterizes the rate at which the longitudinal magnetic field is swept across zero and determines the rate of the diabatic energy levels at the avoided crossing.

The sweep parameter α can be expressed in terms of the time derivative of the longitudinal magnetic field

$$\alpha = \left| |B(t)| \frac{\partial}{\partial t} \left(\arctan \frac{\dot{B}_z t}{|B(t)|} \right) \right|_{t=0} = |\dot{B}_z| \tag{4.3}$$

this expression directly relates the ramp on B_z to the variation of the Larmor precession frequency of the atomic spins around the applied magnetic field.

The Hamiltonian defined in Eq. (4.2) describes the evolution of the hyperfine ground state of sodium with total angular momentum $F = 1$, which includes the three Zeeman sublevels ($m_F = +1, 0, -1$) corresponding to the projection of F along the quantization axis, chosen here to be z-axis. In the low-magnetic-field regime considered here, their energies are determined by the linear Zeeman effect, as given by the Breit-Rabi formula (1.66).

In addition to the longitudinal magnetic component which sets the quantization axis B_z, a finite transverse field component $B_\perp = \sqrt{B_x^2 + B_y^2}$ is present. This component prevents the energy levels crossing even in the absence of longitudinal field, giving rise to avoided crossing whose minimum gap is proportional to $B_\perp$. As a result, the degeneracy between different m_F states is lifted even when $B_z = 0$.

The three central panels of Fig. 4.1[134] illustrate the time evolution of the energy levels during a linear ramp of the longitudinal magnetic field from a positive value $B_{z,\text{ramp}}$ to negative value $-|B_{z,\text{ramp}}|$, assuming that the field crosses zero at $t = 0$. In particular the three panels refer to different values of the transverse magnetic field, which decreases from top to bottom (as shown in the three left panels of Fig 4.1). The size of the energy gap between the $m_F = -1$ and $m_F = +1$ states decreases accordingly, affecting the spin dynamics.

Assuming the atomic sample to be initially prepared in the $m_F = -1$ state at large positive B_z, when the B_z is ramped through zero, population transfer to other Zeeman states can occur depending on the size of the energy gap, as

reported in the three right panels showing the experimental results of Stern-Gerlach measurement performed at the end of the ramp. Accordingly to the analytical model discussed in [133], the populations measured long after the field inversion are given by [140]

$$P_{+1} = p^2 \tag{4.4}$$

$$P_0 = 2p(1-p) \tag{4.5}$$

$$P_{-1} = (1-p)^2 \tag{4.6}$$

where p is the Landau-Zener transition probability,

$$p = e^{-2\pi|g_f|\mu_B \frac{\Delta^2}{2\hbar|\dot{B}_z|}} \tag{4.7}$$

From this expression it follows that a complete transfer from the initial state $m_F = -1$ to the final state $m_F = +1$ takes place when $p \sim 1$, corresponding to either a large ramp speed $|\dot{B}_z|$ or a small energy gap Δ, meaning a small transverse magnetic field modulus. This behavior can also be understood in terms of the adiabaticity condition for spin dynamics in a rotating magnetic field: adiabatic evolution requires the rate of change of the magnetic field direction to be much smaller than the Larmor frequency.

$$\left|\frac{\dot{B}_z}{|B|}\right| \ll \left|\frac{g_F \mu_B |B|}{\hbar}\right|. \tag{4.8}$$

Violation of this condition leads to diabatic transition between Zeeman states.

In particular, the probability for populating the $m_F = +1$ state exhibits a Gaussian dependence on the transverse magnetic field, with a root-mean-square width given by

$$\sigma_B = \sqrt{\frac{\hbar \dot{B}_z}{2\pi |g_F| \mu_B}} \tag{4.9}$$

4.2 Experimental protocols

4.2.1 Characterization of the transverse residual magnetic field

The objective of this procedure is to determine the optimal transverse magnetic field $B_\perp$ to minimize the residual transverse magnetic field. This contribution, which is generated by driving a current in two orthogonal pairs of coils, cancels

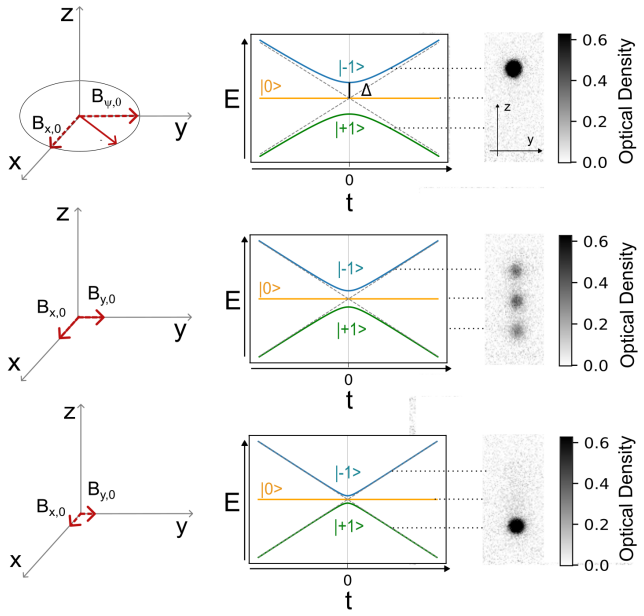

Figure 4.1: For each row, left panels show the transverse magnetic field component (decreasing from upper to lower row), central panels are the energy levels of the three states with $m_F = +1, 0, -1$ as function of t during the ramp in the longitudinal field from positive value $B_{z,\text{ramp}}$ to negative value $-|B_{z,\text{ramp}}|$ assuming the field crosses zero at $t = 0$. The right panels show the experimental results of the Stern-Gerlach measurements performed at the end of the ramp assuming all the atoms are at the beginning in the $m_F = -1$ state, giving the relative populations of the three states. In the upper panel, for large transverse magnetic field we have an adiabatic rotation, all the atoms remains in the $m_F = -1$ state, for lower panel, where the transverse magnetic field component is negligible we obtain a completely diabatic rotation, all the atoms are in the $m_F = +1$ state. For the intermediate situation we obtain a partial transfer.

the magnetic field arising from the residual magnetization of the magnetic shield.

The method is based on the measure of the population transferred to the $m_F = +1$ state as a function of the applied transverse compensation fields $B_{x,\mathrm{coils}}$ and $B_{y,\mathrm{coils}}$. For a given longitudinal field ramp speed, the LZ transfer shows a peaked structure whose center and height of the peak encode information about the residual transverse magnetic field components, and the width completely depends on the speed of the longitudinal field ramp. By iteratively adjusting the compensation fields to maximize the diabatic transfer, the compensating field can be optimized with high precision.

Two experimental schemes are employed to implement the LZ ramp, differing in whether the ramp is performed on a thermal cloud or on a condensate sample. In both cases, initial estimates of the compensation fields $B_{x,\mathrm{comp}}$ and $B_{y,\mathrm{comp}}$ are applied, and the longitudinal magnetic field is swept across zero with a tunable ramp duration Δt^*.

In Scheme A (red line in Fig. 4.2), the LZ ramp is applied before evaporation. The longitudinal magnetic field is linearly ramped from $B_{z,\mathrm{ramp}}$ to $-B_{z,\mathrm{ramp}}$ over Δt^*. Afterwards, the field is further reduced in 50 ms to a value $-B_{z,\mathrm{c}} = 130$ mG, satisfying $|B_{z,c}| \ll |B_{z,\mathrm{ramp}}|$. Subsequently, evaporative cooling in the optical trap is performed and condensation takes place. For state sensitive imaging, the infrared trapping potential is switched off and a vertical magnetic field gradient of 8G/cm is applied in order to spatially separate the three Zeeman components in a Stern-Gerlach measurement. Absorption imaging is then performed after 18ms of time of flight. Performing condensation before the imaging is necessary to enhance the spatial spin resolution, given the relatively small gradient field and the limited balistic expansion time.

Scheme B (blue line in Fig. 4.2), is designed to reduce the sensitivity of the measurement to magnetic field inhomogeneities by performing the LZ ramp on a condensed sample, which has a smaller spatial extension. In this case the order of evaporation and LZ ramp is reversed. The longitudinal field is initially set to $B_z = B_{z,\mathrm{c}} = 130$ mG, the value at which the evaporation in the optical trap takes place. The field is then ramped down in 50 ms to $B_{z,\mathrm{ramp}}$, after which the LZ sweep from $B_{z,\mathrm{ramp}}$ to $-|B_{z,\mathrm{ramp}}|$ is applied.

Even if the ramp duration is a tunable parameter, it must satisfy some constraints. The LZ ramp duration must be much longer than the coil response time constant $\tau = L/R \simeq 0.5$ ms, where L and R are the inductance and the resistance of the coils respectively, and much shorter than the lifetime of the sample in the trap ($\tau_{\mathrm{BEC}} \simeq 1$s, $\tau_{\mathrm{th}} \gg 1$s are the lifetime of a condensate and a thermal sample, respectively). Depending on the ramp duration, the amplitude $B_{z,\mathrm{ramp}}$ is varied between 1.5 mG and 750 μG, corresponding to

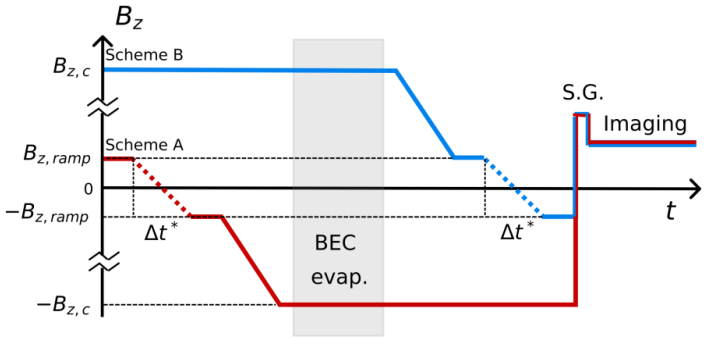

Figure 4.2: Transverse field minimization protocol. Longitudinal field B_z as a function of time. (Red line) Scheme A consists in a ramp from $B_{z,\mathrm{ramp}}$ to $-B_{z,\mathrm{ramp}}$ performed on thermal cloud, then the field is brought down to $-B_{z,c}$ in 50 ms before the evaporation in the optical trap. (Blue line) Scheme B starts with a field at $B_{z,c}$ at which the evaporation takes place, then the field is ramped down to $B_{z,\mathrm{ramp}}$ in 50 ms and the ramp from $B_{z,\mathrm{ramp}}$ to $-B_{z,\mathrm{ramp}}$ takes place o the condensate sample. In both cases the dotted line represent the ramp across zero which has a tunable duration Δt^*. The shaded gray area is the time during which evaporation to obtain condensation is performed.

ramp speed $|\dot{B}_z|$ ranging from 3 G/s down to 1.5 mG/s.

To determine the optimal compensation fields, the measurement is repeated for different values of $B_{x,\mathrm{coils}}$ and $B_{y,\mathrm{coils}}$. The optimal values are those that maximize the population transferred to $m_F = +1$ state, opposite to the initial state. The optimization is performed through an iterative procedure. In the first iteration, a scan of $B_{x,\mathrm{coils}}$ is performed with $|\dot{B}_z| = 300\mathrm{mG/s}$ and $B_{y,\mathrm{coils}} = 0$. In such a way we obtain a value $B_{x,0}$ corresponding to maximal transfer to the state $m_F = +1$. Subsequently, $B_{x,\mathrm{coils}}$ is fixed to $B_{x,0}$ and a scan over $B_{y,\mathrm{coils}}$ is performed to determine $B_{y,0}$. This procedure is iterated. At each iteration, the longitudinal ramp speed is decreased in order to increase the sensitivity to the residual field, since the slower the ramp the narrower the $m_F = +1$ transfer peak. The scheme of this iterative protocol is shown in panel (a) of Fig. 4.3 [134].

The experimental data are fitted using the Landau-Zener probability expressions for the three states defined in Eqs. 4.4, 4.5 and 4.6 from which the center of the transfer peak, the maximum transferred population $P_{+1,\mathrm{max}}$ and the width σ_B are extracted. The center of the peak corresponds to zero residual field along the scanned direction and it is used to calibrate the compensation coil currents.

Once the residual field along one transverse direction is minimized, the

residual field along the orthogonal direction can be inferred from the maximum transfer according to

$$B_y = \sigma_B \sqrt{-2 \ln(P_{1,\max})} \tag{4.10}$$

this quantity is reduced after each scan. Panel (b) of Fig. 4.3 shows the experimental result (dots) and the corresponding L-Z fits (solid line), for three different ramp speeds. As expected, slowing down the ramp leads to smaller values of σ_B, enhancing the resolution of the magnetic field characterization procedure.

Compensation of the residual magnetic gradient The presence of a residual magnetic field gradient provides an additional contribution to the width of the peak, which we expect to sum in quadrature with the theoretical width σ_B originating from the residual homogeneous magnetic field.

$$\sigma_{\text{tot}} = \sqrt{\sigma_{\text{grad}}^2 + \sigma_B^2} \tag{4.11}$$

This implies that, by further slowing down the ramp, the system eventually reaches the limit given by the contribution of the magnetic field gradient. For this reason, we also compensate for it. In particular, we compensate the gradient along the x direction, corresponding to the elongated axis of the condensate which is therefore the direction of highest sensitivity.

As stated above, the optimal value of the compensating magnetic field gradient is determined by repeating scan measurement along one of the two transverse directions for different values of $\nabla B_{x,\text{coils}}$ and identifying the value that produces the maximum narrowing of the peak. It is important to note, however, that the application of a compensating magnetic field gradient also induces a shift of the residual magnetic field along the same direction. As a consequence, the parameter $B_{x,\text{coils}}$ must be calibrated through iterative measurements which includes the optimization of the magnetic field gradient. For the calibration, we set the ramp velocity to 10 mG/s, ensuring that the effect of the residual gradient on the peak width is clearly observable. We then perform two successive scans of $B_{x,\text{coils}}$ and $B_{y,\text{coils}}$ to calibrate the fields for the new gradient value. Finally, an additional scan of $B_{x,\text{coils}}$ is carried out, from which the peak width σ_B is extracted and the value of the optimal compensation gradient, corresponding to the minimal peak width, is obtained.

Fig. 4.4 shows an example of measurement performed without gradient compensation (left panels) and with gradient compensation (right panels), both taken at a constant ramp speed of 3.75 mG/s. A clear reduction of the peak width can be observed when the gradient compensation is applied.

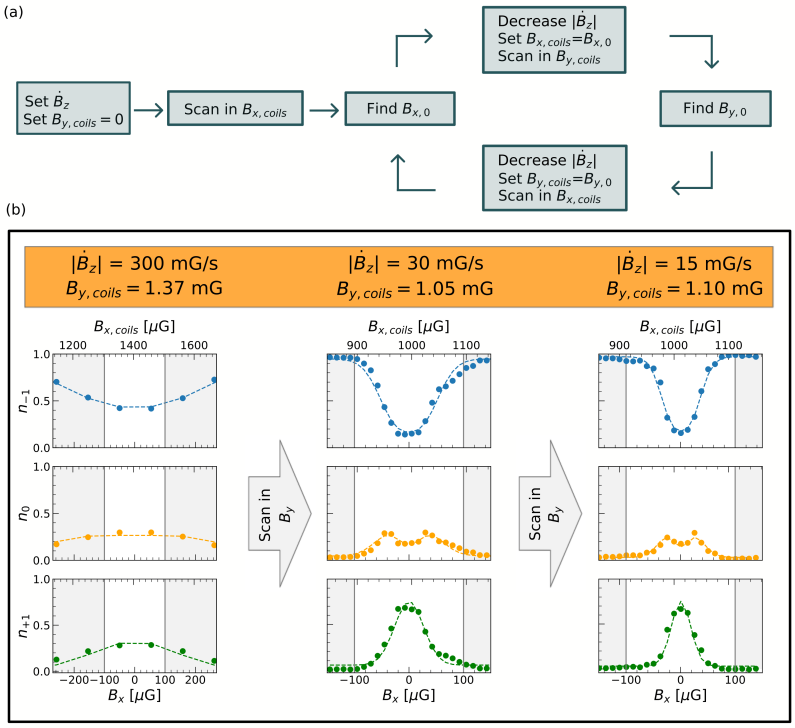

Figure 4.3: Panel (a) illustrates a scheme of the iterative compensation procedure. Panel (b) shows the relative populations of the three Zeeman sublevels, $m_F = -1, 0, +1$ (from top to bottom) measured for decreasing longitudinal-field ramp velocities (from left to right). In each panel, the experimental data are represented by dots, while the solid line corresponds to fits obtained using the Landau-Zener model. The populations are plotted as a function of the magnetic field component along the x direction. For each panel the upper horizontal axis indicates the magnetic field generated by the compensation coils, while the lower axis is shifted according to the fitted center of the transfer peak. The ramp speed used in each measurement is specified in the orange box as well as the value of the compensation field applied in the y direction during the corresponding scan. The offset in the compensating field in the first column is due to the fact that the data in that column were acquired with a few weeks delay with respect to the other set of data.

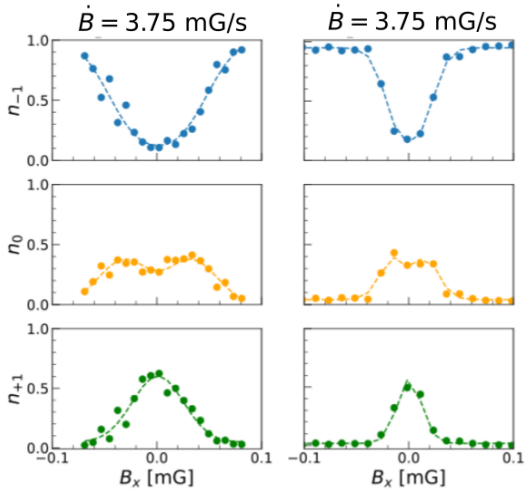

Figure 4.4: Relative populations, after applying the magnetic field ramp, of the three Zeeman states $m_F = -1, 0, +1$ (from top to bottom), without gradient compensation (left panels) and with gradient compensation (right panels).

4.2.2 Characterization of the longitudinal field

The protocol used to characterize the residual longitudinal magnetic field is shown in Fig. 4.5. The longitudinal field $B_z(t)$ is swept according to a sequence analogous to scheme B employed for transverse field compensation. The main difference is that in this case the ramp velocity is kept fixed, while the final value of the field $B_{z,\text{fin}}$ is varied. During the entire sequence, the transverse magnetic fields are kept at their optimal compensation values $B_{x,\text{coils}} = B_{x,0}$ and $B_{y,\text{coils}} = B_{y,0}$. In the case of $B_{z,\text{fin}} > 0$, the ramp does not crosses zero; thus LZ transfer to $m_F = +1$ state does not take place and the atoms remain in the $m_F = -1$ state. Conversely, if $B_{z,\text{fin}} < 0$, the ramp crosses zero and the transfer to $m_F = +1$ state takes place. In this way it is possible to identify the threshold value of $B_{z,\text{fin}}$ at which a change in the system's behavior is observed, corresponding to the zero crossing of the magnetic field. The magnetic field along y is omitted from Fig. 4.5 since it remains constant during the whole protocol, while the time dependence of the transverse field along x is shown. The field is initially set at $B_{x,0}$ and is then adiabatically ramped to a finite value before being returned to $B_{x,0}$ for the imaging stage. This procedure prevents from unwanted diabatic spin inversion before the Stern-Gerlach measurement in the $B_{z,\text{fin}} < 0$ case, since the imaging is always implemented at a positive value of B_z.

The experimental procedure begins with evaporative cooling taking place at a positive longitudinal magnetic field $B_{z,c} = 130$ mG. Once condensation

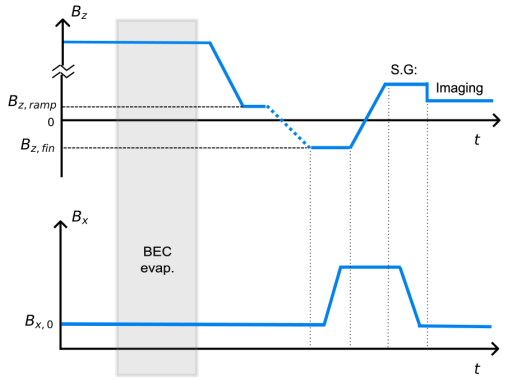

Figure 4.5: Protocol for the longitudinal field characterization. (Upper panel) field in z direction as a function of time. It is analogous to scheme B of the previous protocol with the only difference that the speed of the ramp is fixed while the final value $B_{z,\mathrm{fin}}$ is varied. (Lower panel) field in the x direction as function of time. It is fixed at the optimal value $B_{y,0}$ determined through the previous protocol, the it is ramped adiabatically to a finite value and then back to the $B_{x,0}$ value for the imaging procedure. The field along y-direction is not shown in the figure since it is kept fixed to the optimal value $B_{y,0}$.

is achieved, the field is ramped from positive value $B_{z,\mathrm{ramp}}$ to a variable final value $B_{z,\mathrm{fin}}$ at a constant rate $\dot{B}_z = -0.39$ G/s. Looking to the transferred population as a function of $B_{z,\mathrm{fin}}$ allows for the characterization of the residual longitudinal magnetic field. The robustness of this method is confirmed by repeating the measurement for different ramp velocities, which are found not to affect the experimental outcome.

4.3 Results

Transverse field characterization The experimental data for the Zeeman-state populations were fitted using Eqs. 4.4, 4.5 and 4.6 as fitting functions. A single global fit was performed, from which both the peak width σ_B and its amplitude were extracted. σ_B depends only on the speed of the longitudinal magnetic field ramp, while the amplitude of the peak is related to the transition probability and thus, to the residual transverse magnetic field $B_\perp$.

Panel (a) of Fig. 4.6 displays the extracted transition width σ_B as a function of the inverse magnetic-field ramp speed for the two protocols introduced in Sec. 4.2.1. Red markers refer to scheme A, where the Landau–Zener sweep

is applied to the thermal cloud, while blue markers correspond to scheme B, performed on the condensate. In both cases, σ_B decreases with decreasing ramp speed until a saturation regime is reached. A key role is played by the current-source configuration. Data obtained with the initial setup (two SRS and DELTA Elektronika current sources, see Sec. 2.1.5) are represented by circles and triangles, whereas stars denote measurements performed with the upgraded configuration based on bipolar, highly stable current generators (PROLAN BCS 002/10 and PROLAN BCS 1/1, see Sec. 2.1.5). The improved stability of the latter setup enables significantly narrower transition widths. With the original configuration, saturation occurs at ramp speeds around 3.75 mG/s, while the upgraded apparatus allows further reduction of the peak width, reaching ramp speeds as low as 1.5 mG/s without evident saturation.

The effect of magnetic-field gradient compensation is clear from the experimental data. Measurements performed without gradient compensation (empty symbols) exhibit a clear saturation at $\sigma_B \simeq 20$ μG, attributable to residual magnetic-field inhomogeneities. When the magnetic-field gradient compensation is implemented (filled symbols), the transition width is further reduced. Each data point corresponds to an average over several experimental realizations, and the error bars represent the associated standard deviations. Overall, the measured widths are in good agreement with Landau-Zener theoretical prediction (black dashed line), confirming that the model provides an accurate description of the experimental system.

Panel (b) of Fig. 4.6 reports the residual transverse magnetic field $B_\perp$ extracted from the same fits. The behavior is similar to those observed for σ_B. Without gradient compensation, $B_\perp$ saturates at approximately 25 μG. Compensation reduces this value substantially, leading to a minimum inferred residual field of 14 ± 2 μG with the first current-source configuration and 10.5 ± 1.8 μG with the upgraded setup. Although error bars are included, they are smaller than the marker size and therefore not visible in the figure.

Technical limitations on both the minimum achievable transition width and the smallest extractable residual transverse field arise from current noise in the sources driving the compensation coils, as well as from residual magnetic-field gradients along the x-direction originating from spatial inhomogeneities of B_y and B_z along the x-axis, which cannot be compensated within our experimental setup.

Long term measurements performed over several months indicate that the compensation of the residual magnetic field is generally stable over timescales of several weeks. However, sporadic abrupt variations of the compensation field, on the order of a few hundred μG, were observed (only a few events over six months) and could not be correlated with technical causes.

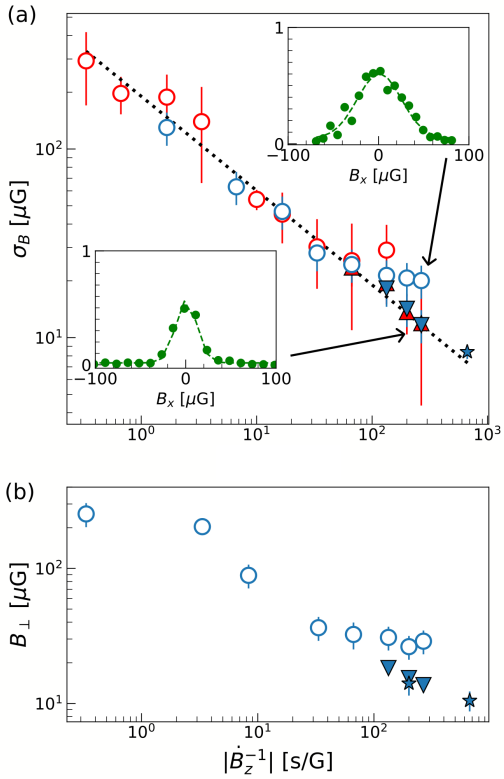

Figure 4.6: (a) Width σ_B of the Landau–Zener transfer probability as a function of the inverse magnetic-field ramp speed. The black dashed line represents the theoretical prediction from Landau–Zener theory. Red (blue) symbols correspond to experimental data acquired using scheme A (scheme B). Empty markers denote measurements performed without residual gradient compensation, while filled markers indicate data obtained with magnetic field gradient compensation. Star-shaped symbols identify measurements performed using the upgraded setup based on highly stable bipolar current generators (see Sec. 2.1.5). Error bars represent the standard deviation over independent experimental realizations. Insets: representative populations in the $m_F = +1$ state measured at a ramp speed of 3.75 μG/s, without (right) and with (left) gradient compensation. (b) Residual transverse magnetic field $B_\perp$ extracted from the population fits as a function of the inverse ramp speed. Error bars are smaller than the marker size and therefore not visible.

Longitudinal field characterization The characterization of the longitudinal magnetic field was carried out using again a single global fit for the experimental data of the populations in the three Zeeman state. The populations in the three states are modeled by the time dependent theory described in [133] and they are fitted through the following fitting functions:

$$P_{-1} = \frac{A}{1 + e^{-(x+x_0-x_c)/\tau}} \tag{4.12}$$

$$P_{+1} = B - \frac{B}{1 + e^{-(x-x_0-x_c)/\tau}} \tag{4.13}$$

$$P_0 = 1 - P_{-1} - P_{+1} \tag{4.14}$$

Within this framework, the parameter x_0 corresponds to the value of the magnetic field $B_{z,0}$ that compensates the residual longitudinal field. Fig 4.7 shows the experimental populations (symbols), obtained by averaging several experimental realizations, together with the results of the fit, from which we extract a compensation field of $B_{z,0} = -323 \pm 10$ μG.

By combining the results for the minimal transverse and longitudinal residual magnetic fields, we estimate that the experimental setup allows us to reach a minimum magnetic field modulus of (18 ± 5) μG. This value satisfies the conditions required for the observation of a nematic phase in an elongated ^{23}Na Bose-Einstein condensate.

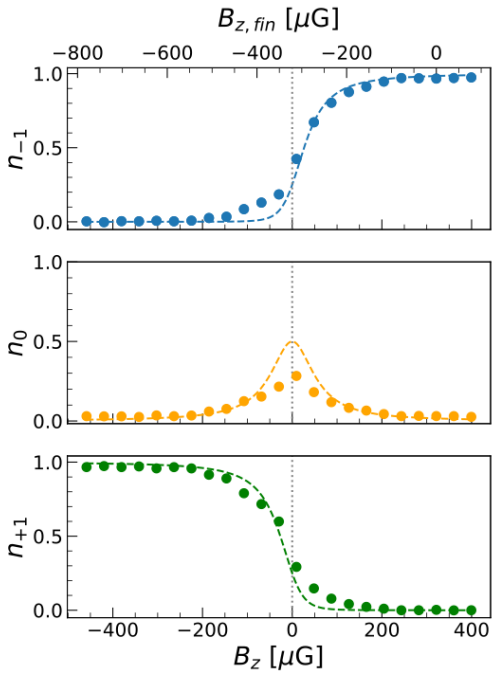

Figure 4.7: Example of the longitudinal magnetic field characterization. Each panel shows the relative population of the three Zeeman states as a function of the final longitudinal magnetic field $B_{z,\mathrm{fin}}$. Data points represent experimental measurements averaged over multiple realizations, with standard deviations smaller than the marker size. The dotted line correspond to the fits obtained using the time dependent model. The gray vertical dotted line indicates the value $B_{z,0}$ that compensates the residual longitudinal magnetic field.

Conclusions

In this thesis, I have presented two experimental investigations performed with superfluid mixtures of ^{23}Na atoms, which, respectively address out-of-equilibrium dynamics and precision control with ultracold gases.

In the first part of this thesis, I experimentally investigate the role of temperature in False Vacuum Decay. FVD was originally predicted in the cosmological context, where it is one of the leading explanation for the early Universe inflationary expansion. However, despite extensive theoretical studies on the subject, it remains unclear which observables could reveal a past decay of our Universe from a metastable false vacuum state to a true vacuum state. In our experimental platform, this decay phenomenon manifests through the stochastic nucleation of spin domains (bubbles) separated by domain walls. In particular, our system consists of a Bose mixture of the hyperfine states $|F = 1, m_F = -1\rangle$ and $|F = 2, m_F = -2\rangle$, coherently-coupled by microwave radiation.

The high degree of tunability and controllability of our platform makes it particularly suitable for studying decay processes whose rates depend exponentially on system parameters. In particular, the coherent coupling strength can be precisely tuned, driving the system through a quantum phase transition between a paramagnetic and a ferromagnetic phase where the energy imbalance between the two minima of the effective double-well potential can be precisely adjusted, allowing the preparation of an extended metastable configuration. Within this framework, our superfluid system has enabled the first experimental observation of false vacuum decay in a controllable environment [12]. Experimentally, we observe the decay of a metastable state prepared in the ferromagnetic regime through the nucleation and growth of spin domains.

A central result of this thesis is the measurement of the decay rate of the metastable state as a function of temperature [91]. We observe that increasing the temperature enhances the nucleation rate of spin domains, resulting in a faster relaxation of the field. The observed decay dynamics is in good

agreement with theoretical predictions based on the finite-temperature extension of instanton theory. These results confirm that thermal fluctuations of the surrounding thermal bath enhance the fluctuations of the macroscopic field, thereby accelerating the decay process. These findings establish ultracold atomic mixtures as a versatile platform for experimentally testing finite-temperature quantum field theory as for example the Higgs field stability [98, 99] and may provide new insights for the understanding of early Universe due to the application of FVD to inflationary models [100, 101, 102].

Future developments could extend these studies towards regimes that are largely unexplored. In particular, improving the control of the trapping potential and developing non-destructive imaging techniques allow for the exploration of new aspects of FVD. The implementation of a digital micromirror device (DMD) enables the realization of homogeneous trapping geometries, which gives us access to the systematic study of free bubble dynamics. In particular, in such a homogeneous system it would be possible to study bubble interaction and collisions. Furthermore, the realization of a uniform two-dimensional condensate would open the possibility of investigating FVD in a largely unexplored regime [141]. In two dimensions, not only the size but also the shape of the nucleated bubbles becomes relevant, leading to domain walls geometries with different energy costs. Moreover, the development of non destructive imaging techniques would allow real-time tracking of bubble expansion following their stochastic nucleation [142]. Finally, it would be interesting to access the purely quantum regime of false vacuum decay, but reaching the required temperature remains technically challenging.

The second part of this thesis focuses on the development of high-precision magnetic-field control techniques for spinor Bose gases. Using an $F = 1$ spin mixture, we implement a protocol capable of measuring and compensating residual magnetic fields with a sensitivity at the level of approximately 10 μG [134] which is well below the sensitivity of conventional magnetometric techniques. The method relies on monitoring the Zeeman population dynamics induced by diabatic spin rotations.

Experimentally, we track the evolution of the populations in the three Zeeman sublevels following controlled spin rotations. The resulting dynamics provides a sensitive probe for small magnetic-field components and gradients. The observed population dynamics is accurately reproduced by a theoretical model based on Landau–Zener transitions in an effective three-level system, demonstrating excellent quantitative agreement between experiment and theory. This approach effectively turns the ultracold atomic ensemble into a highly

sensitive magnetic-field sensor, allowing to reduce the magnetic field modulus to the target value of few tens of microGauss.

This level of control of the magnetic field opens the possibility of exploring new regimes of spinor Bose–Einstein condensates where the physics is dominated by spin-dependent interactions rather than by Zeeman shifts. In particular, it enables progress towards the realization of a spatially-extended $F = 1$ condensate in the interaction-dominated regime at near-zero magnetic field. In this regime, mean-field theory for antiferromagnetic spinor condensates predicts the emergence of a nematic order parameter [143], whereas full many-body theory predicts that the ground state corresponds to a highly entangled singlet state [16]. Signatures of the nematic phase have been observed experimentally in relatively small systems containing a few thousand atoms [15]. In these systems, the critical magnetic field required to observe the phase transition to the interaction-dominated regime is estimated to be on the order of hundreds of milligauss [15]. Beyond-mean-field effects have been explored in even smaller samples containing around one hundred atoms [19]. However, these phenomena remain largely unexplored in spatially extended condensates for which achieving the required conditions demands magnetic-field stability well below typical experimental limits. The technique developed in this work provides the level of magnetic-field control and sensitivity required for the experimental realization of the interaction-dominated quantum states also in extended geometries, allowing the investigation of condensate fragmentation due to symmetry (in this case the spin rotational symmetry) and to probe the collective modes and superfluid properties of this fragmented phase.

The realization of an extended singlet condensate would open the way to a number of further investigations, including the characterization of the system elementary excitation spectrum and the study of topological excitations, such as nematic spin vortices (NSVs) whose emergence and stability have been theoretically investigated in [144, 145, 146, 147]. The structure of the vortex core critically depends on the quadratic Zeeman energy, with a transition from a normal core to a polar core occurring below a threshold value for the quadratic Zeeman shift. The properties of these spin vortices have been theoretically analyzed in quasi-two-dimensional geometries, where their excitation spectrum has been calculated in order to assess their dynamical stability. Although nematic spin vortices are generally predicted to be dynamically unstable, theoretical studies [146] indicate that a stable regime can be reached by increasing the strength of the spin-dependent interactions. Identifying and accessing this parameter regime would open the possibility of experimentally observing stable nematic spin vortices and systematically investigating their properties.

A key element underlying both experimental investigations presented in this thesis is the high degree of stability of the experimental apparatus with respect to magnetic-field fluctuations. This stability enables both the controlled preparation of metastable states required for the study of false vacuum decay and the high-resolution magnetic-field characterization required for precision measurements in spinor gases. More broadly, the level of magnetic-field control achieved in this work establishes our system as a robust platform for exploring new regimes of non-equilibrium dynamics, topological defects, and interaction-driven quantum phases in ultracold quantum gases. These results highlight how ultracold atomic mixtures, combined with precise control of external parameters, provide a powerful experimental setting for realizing and studying paradigmatic models of quantum field theory and many-body physics.

List of Figures

List of Tables

Bibliography

[1] D. Guéry-Odelin and C.Cohen-Tannoudji. "Advances in Atomic Physiscs: An Overview". In: *World Scientific Publishing Company* (2011).

[2] E. Cornell and C. Wienmann. "Bose-Einstein Condensation in a diluite gas: the first 70 years and some recent experiment (Nobel Lecture)". In: (2002).

[3] W. Ketterle. "Nobel Lecture". In: (2001).

[4] D.M.Stamper-Kurn et al. "Optical confinement of a Bose-Einstein condensate." In: *Phys.Rev.Lett* (1998), pp. 2027–2030.

[5] D.M.Stamper-Kurn and M. Ueda. "Spinor bose gases: Symmetries, magnetism and quantum dynamics." In: *Rev. Mod. Phys.* (2013), pp. 1191–1244.

[6] J. Inoue, B.K. Chackrabarti, and S.Suzuki. *Qunatum Ising Phases and Transitions in Transverse Ising Model*. Springer, 2008.

[7] Subir Sachdev. *Quantum Phase Transitions*. 2nd. New York: Cambridge University Press, 2011.

[8] R. Cominotti et al. "Ferromagnetism in an Extended Coherently Coupled Atomic Superfluid". In: *Phys. Rev. X* 13 (2 2023), p. 021037. DOI: 10.1103/PhysRevX.13.021037. URL: https://link.aps.org/doi/10.1103/PhysRevX.13.021037.

[9] Anna Berti. "Simulation of curved-space quantum field theories with two-component Bose-Einstein condensates: from black hole physiscs to cosmology." PhD thesis. University of Trento, 2024.

[10] Sidney Coleman. "Fate of the false vacuum: Semiclassical theory". In: *Phys. Rev. D* 15 (10 1977), pp. 2929–2936. DOI: 10.1103/PhysRevD.15.2929. URL: https://link.aps.org/doi/10.1103/PhysRevD.15.2929.

[11] A.D. Linde. “Fate of the false vacuum at finite temperature: Theory and applications”. In: *Physics Letters B* 100.1 (1981), pp. 37–40. ISSN: 0370-2693. DOI: https://doi.org/10.1016/0370-2693(81)90281-1. URL: https://www.sciencedirect.com/science/article/pii/0370269381902811.

[12] A. Zenesini et al. “False vacuum decay via bubble formation in ferromagnetic superfluids”. In: *Nature Physics* (2024).

[13] Yu-Xin Chao et al. “Probing false vacuum decay and bubble nucleation in a Rydberg atom array”. In: *arXiv preprint arXiv:2512.04637* (2025). arXiv: 2512.04637 [quant-ph].

[14] J. Vodeb et al. “Stirring the false vacuum via interacting quantized bubbles on a 5,564-qubit quantum annealer”. In: *Nature Physics* 21 (2025).

[15] David Jacob et al. “Phase diagram of spin-1 antiferromagnetic Bose-Einstein condensates”. In: *Phys. Rev. A* 86 (6 Dec. 2012), p. 061601. DOI: 10.1103/PhysRevA.86.061601. URL: https://link.aps.org/doi/10.1103/PhysRevA.86.061601.

[16] Luigi De Sarlo et al. “Spin fragmentation of Bose–Einstein condensates with antiferromagnetic interactions”. In: *New Journal of Physics* 15.11 (Nov. 2013), p. 113039. DOI: 10.1088/1367-2630/15/11/113039. URL: https://doi.org/10.1088/1367-2630/15/11/113039.

[17] Arnau Sala et al. “Shortcut to adiabaticity in spinor condensates”. In: *Phys. Rev. A* 94 (4 Oct. 2016), p. 043623. DOI: 10.1103/PhysRevA.94.043623. URL: https://link.aps.org/doi/10.1103/PhysRevA.94.043623.

[18] V. Corre. “Magnetism in Spin-1 Bose Einstein Condensate with Antiferromagnetic Interactions.” PhD thesis. Ecole normale supérieure, 2014.

[19] B. Evrad et al. “Observation of fragmentation of a spinor Bose-Einstein condensate”. In: *Science* 373 (2021), p. 1340.

[20] S.N. Bose. “Bose plancks gesetz und lichtquantenhypothese.” In: *Z. Physics* 26 (1924), pp. 178–181.

[21] A. Einstein. “Quantentheorie des einatomigen idealen Gases.” In: *Sitzungsberichte der Preussischen Akademie der Wissenschaften* (1925), pp. 1–3.

[22] K. Huang. *Statistical mechanics*. New York: Wiley, 2008. Chap. 12.

[23] C.J. Pethick and H. Smith. *Bose Einstein Condensation in Diluite Gases*. Cambridge University Press, Cambridge, 2011.

[24] Franco Dalfovo et al. "Theory of Bose-Einstein condensation in trapped gases". In: *Rev. Mod. Phys.* 71 (3 Apr. 1999), pp. 463–512. DOI: 10.1103/RevModPhys.71.463. URL: https://link.aps.org/doi/10.1103/RevModPhys.71.463.

[25] Lev Pitaevskii and Sandro Stringari. *Bose Einstein condensation and superfluidity*. International series of monographs on physics. Oxford: Oxford University Press, 2016.

[26] C. C. Bradley, C. A. Sackett, and R. G. Hulet. "Bose-Einstein Condensation of Lithium: Observation of Limited Condensate Number". In: *Phys. Rev. Lett.* 78 (6 Feb. 1997), pp. 985–989. DOI: 10.1103/PhysRevLett.78.985. URL: https://link.aps.org/doi/10.1103/PhysRevLett.78.985.

[27] G. Modugno. "Bose-Einstein Condensation of Potassium Atoms by Sympathetic Cooling". In: *Science* 294.5545 (2001), pp. 1320–1322. DOI: 10.1126/science.1066687.

[28] A. Mosk et al. "Mixture of ultracold lithium and cesium atoms in an optical dipole trap". In: *Applied Physics B* 73.8 (2001), pp. 791–799. DOI: 10.1007/s003400100743.

[29] Tetsu Takekoshi et al. "Ultracold Dense Samples of Dipolar RbCs Molecules in the Rovibrational and Hyperfine Ground State". In: *Physical Review Letters* 113.20 (2014), p. 205301. DOI: 10.1103/PhysRevLett.113.205301.

[30] E. Wille et al. "Exploring an ultracold Fermi-Fermi mixture: Interspecies Feshbach resonances and scattering properties of ^{6}Li and ^{40}K". In: *Physical Review Letters* 100.5 (2007), p. 053201. DOI: 10.1103/PhysRevLett.100.053201.

[31] M. Taglieber et al. "Quantum Degenerate Two-Species Fermi-Fermi Mixture Coexisting with a Bose-Einstein Condensate". In: *Physical Review Letters* 100.1 (2008), p. 010401. DOI: 10.1103/PhysRevLett.100.010401.

[32] Cheng-Hsun Wu et al. "Ultracold Fermionic Feshbach Molecules of ^{23}Na-^{40}K". In: *Physical Review Letters* 109.8 (2012), p. 085301. DOI: 10.1103/PhysRevLett.109.085301.

[33] Bo Huang, Michael M. Parish, and Nikolaj T. Zinner. "Breathing mode of a Bose-Einstein condensate repulsively interacting with a fermionic reservoir". In: *Physical Review A* 99.4 (2019), p. 041602. DOI: 10.1103/PhysRevA.99.041602.

[34] F. Schreck et al. "Quasipure Bose-Einstein Condensate Immersed in a Fermi Sea". In: *Physical Review Letters* 87.8 (2001), p. 080403. DOI: 10.1103/PhysRevLett.87.080403.

[35] I. Ferrier-Barbut et al. "A mixture of Bose and Fermi superfluids". In: *Science* 345.6200 (2014), pp. 1035–1038. DOI: 10.1126/science.1255380.

[36] F. Ferlaino et al. "Dipolar oscillations in a quantum degenerate Fermi Bose atomic mixture". In: *Journal of Optics B: Quantum and Semiclassical Optics* 5.2 (2003), S3–S8. DOI: 10.1088/1464-4266/5/2/351.

[37] D. S. Hall et al. "Dynamics of Component Separation in a Binary Mixture of Bose-Einstein Condensates". In: *Physical Review Letters* 81 (1998), pp. 1539–1542.

[38] C. J. Myatt et al. "Production of Two Overlapping Bose-Einstein Condensates by Sympathetic Cooling". In: *Physical Review Letters* 78 (1997), pp. 586–589.

[39] M. R. Matthews et al. "Watching a Superfluid Untwist Itself: Recurrence of Rabi Oscillations in a Bose-Einstein Condensate". In: *Physical Review Letters* 83 (1999), pp. 3358–3361.

[40] J. Stenger et al. "Spin domains in ground-state Bose–Einstein condensates". In: *Nature* 396.6709 (1998), pp. 345–348.

[41] E. M. Bookjans, A. Vinit, and C. Raman. "Quantum Phase Transition in an Antiferromagnetic Spinor Bose-Einstein Condensate". In: *Physical Review Letters* 107 (2011), p. 195306.

[42] K. Jiménez-García et al. "Spontaneous formation and relaxation of spin domains in antiferromagnetic spin-1 condensates". In: *Nature Communications* 10.1 (2019), p. 1422.

[43] M.-S. Chang et al. "Observation of Spinor Dynamics in Optically Trapped ^{87}Rb Bose-Einstein Condensates". In: *Physical Review Letters* 92 (2004), p. 140403.

[44] D. S. Petrov. "Quantum Mechanical Stabilization of a Collapsing Bose–Bose Mixture". In: *Physical Review Letters* 115.15 (2015), p. 155302. DOI: 10.1103/PhysRevLett.115.155302.

[45] G. Semeghini et al. “Self-Bound Quantum Droplets of Atomic Mixtures in Free Space”. In: *Physical Review Letters* 120.23 (2018), p. 235301. DOI: 10.1103/PhysRevLett.120.235301.

[46] C. R. Cabrera et al. “Quantum liquid droplets in a mixture of Bose–Einstein condensates”. In: *Science* 359.6373 (2018), pp. 301–304. DOI: 10.1126/science.aao5686.

[47] C. D’Errico et al. “Observation of quantum droplets in a heteronuclear bosonic mixture”. In: *Physical Review Research* 1.3 (2019), p. 033155. DOI: 10.1103/PhysRevResearch.1.033155.

[48] L. D. Landau and E. M. Lifshitz. “On the theory of the dispersion of magnetic permeability in ferromagnetic bodies”. In: *Physikalische Zeitschrift der Sowjetunion* 8 (1935), pp. 153–164.

[49] V.G. Bar’yakhtar and B.A. Ivanov. “The Landau-Lifshitz equation: 80 years of hystory, advances, and prospects”. In: *Low Temperature Physiscs* (2015), pp. 663–669.

[50] Tilman Zibold. “Classical Bifurcation and Entanglement Generation in an Internal Bosonic Josephson Junction”. PhD thesis. University of Heidelberg, 2012.

[51] Helmut Strobel et al. “Fisher information and entanglement of non-Gaussian spin states”. In: *Science* 345.6195 (2014), pp. 424–427. DOI: 10.1126/science.1241825.

[52] Chaohong Lee et al. “Phase-dependent spontaneous spin polarization and bifurcation delay in coupled two-component Bose-Einstein condensates”. In: *Physical Review A* 69.3 (2004), p. 033611. DOI: 10.1103/PhysRevA.69.033611.

[53] E. Nicklas et al. “Nonlinear dressed states at the miscibility-immiscibility threshold”. In: *Physical Review A* 92.5 (Nov. 2015), p. 053614. DOI: 10.1103/PhysRevA.92.053614.

[54] S. Bresolin et al. “Oscillating Solitons and ac Josephson Effect in Ferromagnetic Bose-Bose Mixtures”. In: *Physical Review Letters* 130.22 (2023), p. 220403. DOI: 10.1103/PhysRevLett.130.220403.

[55] A. Farolfi et al. “Quantum-torque-induced breaking of magnetic interfaces in ultracold gases”. In: *Nature Physics* 17.12 (2021), pp. 1359–1363. DOI: 10.1038/s41567-021-01336-0.

[56] Riccardo Cominotti. “Experiments with Coherently-Coupled Bose-Einstein condensates: from magnetism to cosmology”. PhD thesis. University of Trento, 2023.

[57] Matthias Vojta. "Quantum phase transitions". In: *Reports on Progress in Physics* 66.12 (2003), pp. 2069–2110. DOI: 10.1088/0034-4885/66/12/R01.

[58] E. Ising. "Beitrag zur Theorie des Ferromagnetismus". In: *Zeitschrift für Physik* 31 (1925), pp. 253–258.

[59] Markus Greiner et al. "Quantum phase transition from a superfluid to a Mott insulator in a gas of ultracold atoms". In: *Nature* 415.6867 (2002), pp. 39–44. DOI: 10.1038/415039a.

[60] Kristian Baumann et al. "Dicke quantum phase transition with a superfluid gas in an optical cavity". In: *Nature* 464.7293 (2010), pp. 1301–1306. DOI: 10.1038/nature09009.

[61] D. L. Campbell et al. "Magnetic phases of spin-1 spin–orbit-coupled Bose gases". In: *Nature Communications* 7.1 (2016), p. 10897. DOI: 10.1038/ncomms10897.

[62] Alessio Recati and Sandro Stringari. "Coherently Coupled Mixtures of Ultracold Atomic Gases". In: *Annual Review of Condensed Matter Physics* 13.1 (2022), pp. 407–432. DOI: 10.1146/annurev-conmatphys-031620-104951.

[63] Claas Abert. "Micromagnetics and Spintronics: Models and Numerical Methods". In: *European Physical Journal B* 92.6 (2019), p. 120. DOI: 10.1140/epjb/e2019-10034-0.

[64] I. Carusotto and E. Mueller. "Imaging of spinor gases". In: *Journal of Physics B: Atomic, Molecular and Optical Physics* (2004).

[65] Y. Di, Y. Wang, and H. Wei. "Dipole-quadrupole decomposition of two coupled spin 1 systems". In: *J. Phys. A: Math. Theor.* (2010).

[66] S. Millman, I. I. Rabi, and J. R. Zacharias. "On the Nuclear Moments of Indium". In: *Phys. Rev.* 53 (5 Mar. 1938), pp. 384–391. DOI: 10.1103/PhysRev.53.384. URL: https://link.aps.org/doi/10.1103/PhysRev.53.384.

[67] G. Breit and I. I. Rabi. "Measurement of Nuclear Spin". In: *Phys. Rev.* 38 (11 1931), pp. 2082–2083. DOI: 10.1103/PhysRev.38.2082.2. URL: https://link.aps.org/doi/10.1103/PhysRev.38.2082.2.

[68] J. Stenger et al. "Spin domains in ground-state Bose-Einstein condensates". In: *Nature* (1998).

[69] S. Knoop et al. "Feshbach spectroscopy and analysis of the interaction potentials of ultracold sodium". In: *Phys. Rev. A* 83 (4 Apr. 2011), p. 042704. DOI: 10.1103/PhysRevA.83.042704. URL: https://link.aps.org/doi/10.1103/PhysRevA.83.042704.

[70] Oliver Penrose and Lars Onsager. "Bose-Einstein Condensation and Liquid Helium". In: *Phys. Rev.* 104 (3 Nov. 1956), pp. 576–584. DOI: 10.1103/PhysRev.104.576. URL: https://link.aps.org/doi/10.1103/PhysRev.104.576.

[71] Bertrand Evrard et al. "Observation of fragmentation of a spinor Bose-Einstein condensate". In: *Science* 373.6561 (2021), pp. 1340–1343. DOI: 10.1126/science.abd8206. URL: https://www.science.org/doi/abs/10.1126/science.abd8206.

[72] Yvan Castin and Christopher Herzog. "Bose–Einstein condensates in symmetry breaking states". In: *Comptes Rendus de l'Académie des Sciences - Series IV - Physics* 2 (Apr. 2001), pp. 419–443. DOI: 10.1016/S1296-2147(01)01183-0.

[73] Arturo Farolfi. "Spin dynamics in two-component Bose-Einstein condensates". PhD thesis. University of Trento, 2020.

[74] L. Botti et al. "Noninvasive system for the simultaneous stabilization and control of magnetic field strength and gradient". In: *Review of Scientific Instruments* (2006).

[75] C.J.Dedman et al. "Active cancellation of stray magnetic fields in a Bose-Einstein condensation experiment". In: *Review of Scientific Instruments* (2007).

[76] Eleonora Fava. "Static and dynamics properties of a miscible two-component Bose-Einstein condensate". PhD thesis. University of Trento, 2018.

[77] Giacomo Colzi. "A new apparatus to simulate fundamental interactions with ultracold atoms". PhD thesis. University of Trento, 2018.

[78] A. Farolfi et al. "Design and characterization of a compact magnetic shield for ultracold atomic gas experiments". In: *Review of Scientific Instruments* (2019).

[79] Giacomo Colzi et al. "Sub-Doppler cooling of sodium atoms in gray molasses". In: *Phys. Rev. A* 93 (2 2016), p. 023421. DOI: 10.1103/PhysRevA.93.023421. URL: https://link.aps.org/doi/10.1103/PhysRevA.93.023421.

[80] E. Arimondo, M. Inguscio, and P. Violino. "Experimental determinations of the hyperfine structure in alkali atoms". In: *Rev. Mod. Phys.* (1977).

[81] Wo Yei, A. Sieradzan, and M.D. Havey. "Delayed-detection measurement of atomic Na $3p^2P_{3/2}$ hyperfine structure using polarization quantum-beat spectroscopy". In: *Phys. Rev. A* (1993).

[82] W.A. van Wijngaarden and J. Li. "Measurement of hyperfine structure of sodium $3P_{1/2,3/2}$ states using optical spectroscopy". In: *Zeitschrift fur Physics D* (1994).

[83] *LDC501 Datasheet*. ThinkSRS. 2023. URL: https://www.thinksrs.com/downloads/pdfs/catalog/LDC500c.pdf.

[84] Rudolf Grimm, Matthias Weidemuller, and Yurii B. Ovchinnikov. "Optical Dipole Traps for Neutral Atoms". In: *Adv. At. Mol. Opt. Phys.* (2000), pp. 95–170. DOI: 10.1016/S1049-250X(08)60186-X.

[85] K. Dieckmann et al. "Two-dimensional magneto-optical trap as a source of slow atoms". In: *Phys. Rev. A* 58 (5 1998), pp. 3891–3895. DOI: 10.1103/PhysRevA.58.3891. URL: https://link.aps.org/doi/10.1103/PhysRevA.58.3891.

[86] G. Lamporesi et al. "Compact high-flux source of cold sodium atoms." In: *Review of Scientific Instruments* 84 (6 2013).

[87] Wolfgang Ketterle et al. "High densities of cold atoms in a dark spontaneous-force optical trap". In: *Phys. Rev. Lett.* 70 (15 1993), pp. 2253–2256. DOI: 10.1103/PhysRevLett.70.2253. URL: https://link.aps.org/doi/10.1103/PhysRevLett.70.2253.

[88] Daniel Steck. *Sodium D Line Data*. 2003.

[89] Wolfgang Ketterle and N.J. Van Druten. "Evaporative Cooling of Trapped Atoms". In: *Advances in Atomic, Molecular, and Optical Physics* (1996), pp. 181–236.

[90] Giacomo Colzi et al. "Production of large Bose-Einstein condensates in a magnetic-shield-compatible hybrid trap." In: *Phys. Rev. A* 97 (5 2018), p. 053625. DOI: 10.1103/PhysRevA.97.053625. URL: https://link.aps.org/doi/10.1103/PhysRevA.97.053625.

[91] Riccardo Cominotti et al. "Observation of Temperature Effects on False Vacuum Decay in Atomic Quantum Gases". In: *Phys. Rev. Lett.* 135 (18 2025), p. 183401. DOI: 10.1103/l396-yysb. URL: https://link.aps.org/doi/10.1103/l396-yysb.

[92] Carmelo Mordini. "Measurement of the density profile of quantized vortices and of the equation of state in a 3D interacting Bose gas". PhD thesis. University of Trento, 2019.

[93] *ORCA-Flash4.0 V3 Digital CMOS Camera Datasheet*. Hamamatsu Photonics. 2023. URL: https://www.hamamatsu.com/eu/en/product/cameras/cmos-cameras/C13440-20CU.html.

[94] A. Farolfi et al. "Observation of Magnetic Solitons in Two-Component Bose-Einstein Condensates". In: *Phys. Rev. Lett.* 125 (3 2020), p. 030401. DOI: 10.1103/PhysRevLett.125.030401. URL: https://link.aps.org/doi/10.1103/PhysRevLett.125.030401.

[95] C. Mordini et al. "Single-shot reconstruction of the density profile of a dense atomic gas". In: *Opt. Express* (2020), pp. 29408–29418.

[96] Y. Castin and R. Dum. "Bose-Einstein Condensates in Time Dependent Traps". In: *Phys. Rev. Lett.* 77 (27 1996), pp. 5315–5319. DOI: 10.1103/PhysRevLett.77.5315. URL: https://link.aps.org/doi/10.1103/PhysRevLett.77.5315.

[97] C.L.Degen, F. Reinhard, and P.Cappellaro. "Quantum sensing". In: *Rev.Mod.Phys* (2017). DOI: 89:035002.

[98] J. Elias-Miro et al. "Higgs mass implications on the stability of the electroweak vacuum". In: *Physics Letters B* (2012), pp. 222–228.

[99] T. Markannen, A. Rajantie, and S. Stopyra. "Cosmological aspects of Higgs vacuum metastability". In: *Frontiers in Astronomy and Space Science* (2018).

[100] C.J. Hogan. "Gravitational radiation from cosmological phase transitions." In: *Monthly Notices of the Royal Astronomical Society* (1986), pp. 629–636.

[101] M.E. Shaposhnikov. "Baryon Asymmetry of the Universe in Standard Electroweak Theory." In: *Nucl. Phys. B* (1987), pp. 757–775.

[102] Stephen M. Feeney et al. "First observational tests of eternal inflation: Analysis methods and WMAP 7-year results". In: *Phys. Rev. D* 84 (4 2011), p. 043507. DOI: 10.1103/PhysRevD.84.043507. URL: https://link.aps.org/doi/10.1103/PhysRevD.84.043507.

[103] Curtis G. Callan and Sidney Coleman. "Fate of the false vacuum. II. First quantum corrections". In: *Phys. Rev. D* 16 (6 1977), pp. 1762–1768. DOI: 10.1103/PhysRevD.16.1762. URL: https://link.aps.org/doi/10.1103/PhysRevD.16.1762.

[104] A.D. Linde. "Decay of the false vacuum at finite temperature". In: *Nuclear Physics B* 216.2 (1983), pp. 421–445. ISSN: 0550-3213. DOI: https://doi.org/10.1016/0550-3213(83)90293-6. URL: https://www.sciencedirect.com/science/article/pii/0550321383902936.

[105] O. Fialko et al. "Fate of the false vacuum: Towards realization with ultra-cold atoms." In: *Europhysics Letters* (2015).

[106] Thomas P. Billam et al. "Simulating Seeded Vacuum Decay in a Cold Atom System". In: *Phys. Rev. D* 100.6 (2019), p. 065016. DOI: 10.1103/PhysRevD.100.065016. URL: https://link.aps.org/doi/10.1103/PhysRevD.100.065016.

[107] Gianluca Lagnese et al. "False vacuum decay in quantum spin chains". In: *Phys. Rev. B* 104 (20 2021), p. L201106. DOI: 10.1103/PhysRevB.104.L201106. URL: https://link.aps.org/doi/10.1103/PhysRevB.104.L201106.

[108] Steven Weinberg. *Lectures on Qunatum Mechanics*. Cambridge University Press, 2015.

[109] L.D. Landau and E.M. Lifshitz. *Quantum Mechanism: Non-Relativistic Theory. Course of Theoretical Physics.* Elsevier Science, 1981.

[110] D. Szász-Schagrin and G. Takács. "False vacuum decay in the $(1 + 1)$-dimensional φ^4 theory". In: *Phys. Rev. D* 106 (2 2022), p. 025008. DOI: 10.1103/PhysRevD.106.025008. URL: https://link.aps.org/doi/10.1103/PhysRevD.106.025008.

[111] A.D. Linde. "On the vacuum instability and the Higgs meson mass". In: *Physics Letters B* 70.3 (1977), pp. 306–308. ISSN: 0370-2693. DOI: https://doi.org/10.1016/0370-2693(77)90664-5. URL: https://www.sciencedirect.com/science/article/pii/0370269377906645.

[112] A. Farolfi et al. "Manipulation of an elongated internal Josephson junction of bosonic atoms." In: *Phys. Rev. A* (2021).

[113] Matthew J. Brookes et al. "Magnetoencephalography with optically pumped magnetometers (OPM-MEG): the next generation of functional neuroimaging". In: *Trends in Neurosciences* 45.8 (2022), pp. 621–634. ISSN: 0166-2236. DOI: https://doi.org/10.1016/j.tins.2022.05.008. URL: https://www.sciencedirect.com/science/article/pii/S0166223622001023.

[114] T. H. Sander et al. "Magnetoencephalography with a chip-scale atomic magnetometer". In: *Biomed. Opt. Express* 3.5 (2012), pp. 981–990. DOI: 10.1364/BOE.3.000981. URL: https://opg.optica.org/boe/abstract.cfm?URI=boe-3-5-981.

[115] M.C.D: Tayler et al. “Invited Review Article: Instrumentation for nuclear magnetic resonance in zero and ultralow magnetic field.” In: *Rev. Sci. Instrumm* (9 2017).

[116] M. P. Ledbetter et al. “Zero-field remote detection of NMR with a microfabricated atomic magnetometer”. In: *Proceedings of the National Academy of Sciences* 105.7 (2008), pp. 2286–2290. DOI: 10.1073/pnas.0711505105. URL: https://www.pnas.org/doi/abs/10.1073/pnas.0711505105.

[117] P.Bevington, R. Gartman, and W. Chalupczak. “Enhanced material defect imaging with a radio-frequency atomic magnetometer.” In: *J. Appl. Phys* (9 2019).

[118] L.M. Rushton et al. “Unshielded portable optically pumped magnetometer for the remote detection of conductive objects using eddy current measurements”. In: *Review of Scientific Instruments* (12 2022).

[119] Michael V. Romalis and Hoan B. Dang. “Atomic magnetometers for materials characterization”. In: *Materials Today* 14.6 (2011), pp. 258–262. ISSN: 1369-7021. DOI: https://doi.org/10.1016/S1369-7021(11)70140-7. URL: https://www.sciencedirect.com/science/article/pii/S1369702111701407.

[120] G.L. Romani, S.J. Williamson, and L. Kaufman. “Biomagnetic INstrumentation”. In: *Rev. Sci. Intrum.* (12 1982), pp. 1815–1845. URL: https://doi.org/10.1063/1.1136907.

[121] J. Dupont-Roc, S. Haroche, and C. Cohen-Tannoudji. “Detection of very weak magnetic fields (109gauss) by 87Rb zero-field level crossing resonances”. In: *Physics Letters A* 28.9 (1969), pp. 638–639. ISSN: 0375-9601. DOI: https://doi.org/10.1016/0375-9601(69)90480-0. URL: https://www.sciencedirect.com/science/article/pii/0375960169904800.

[122] D. Budker et al. “Resonant nonlinear magneto-optical effects in atoms”. In: *Rev. Mod. Phys.* 74 (4 2002), pp. 1153–1201. DOI: 10.1103/RevModPhys.74.1153. URL: https://link.aps.org/doi/10.1103/RevModPhys.74.1153.

[123] D. Budker and M. Romalis. “Optical magnetometry”. In: *Nat. Phys.* (2007), pp. 227–234.

[124] A. Meraki et al. “Zero-field optical magnetometer based on spin alignment”. In: *Phys. Rev. A* 108 (6 2023), p. 062610. DOI: 10.1103/PhysRevA.108.062610. URL: https://link.aps.org/doi/10.1103/PhysRevA.108.062610.

[125] Morgan W. Mitchell and Silvana Palacios Alvarez. "Colloquium: Quantum limits to the energy resolution of magnetic field sensors". In: *Rev. Mod. Phys.* 92 (2 2020), p. 021001. DOI: 10.1103/RevModPhys.92.021001. URL: https://link.aps.org/doi/10.1103/RevModPhys.92.021001.

[126] T. Isayama et al. "Observation of Larmor spin precession of laser-cooled Rb atoms via paramagnetic Faraday rotation". In: *Phys. Rev. A* 59 (6 1999), pp. 4836–4839. DOI: 10.1103/PhysRevA.59.4836. URL: https://link.aps.org/doi/10.1103/PhysRevA.59.4836.

[127] Y. Cohen et al. "A cold atoom radio-frequecy magnetometer." In: *Appl. Phys. Lett.* (7 2019).

[128] Marcin Witkowski et al. "Matter-wave interference versus spontaneous pattern formation in spinor Bose-Einstein condensates". In: *Phys. Rev. A* 88 (2 2013), p. 025602. DOI: 10.1103/PhysRevA.88.025602. URL: https://link.aps.org/doi/10.1103/PhysRevA.88.025602.

[129] L. Chomaz et al. "Dipolar physics: A review of experiments with magnetic quantum gases". In: *Rep. Prog. Phys.* (2022).

[130] B. Pasquiou et al. "Spontaneous Demagnetization of a Dipolar Spinor Bose Gas in an Ultralow Magnetic Field". In: *Phys. Rev. Lett.* 106 (25 2011), p. 255303. DOI: 10.1103/PhysRevLett.106.255303. URL: https://link.aps.org/doi/10.1103/PhysRevLett.106.255303.

[131] M. Fattori et al. "Magnetic Dipolar Interaction in a Bose-Einstein Condensate Atomic Interferometer". In: *Phys. Rev. Lett.* 101 (19 2008), p. 190405. DOI: 10.1103/PhysRevLett.101.190405. URL: https://link.aps.org/doi/10.1103/PhysRevLett.101.190405.

[132] T. Zibold et al. "Spin-nematic order in antiferromagnetic spinor condensates". In: *Phys. Rev. A* 93 (2 2016), p. 023614. DOI: 10.1103/PhysRevA.93.023614. URL: https://link.aps.org/doi/10.1103/PhysRevA.93.023614.

[133] Y. B. Band and Y. Avishai. "Three-level Landau-Zener dynamics". In: *Phys. Rev. A* 99 (3 2019), p. 032112. DOI: 10.1103/PhysRevA.99.032112. URL: https://link.aps.org/doi/10.1103/PhysRevA.99.032112.

[134] C. Rogora et al. "Progress toward a zero-magnetic-field environment for ultracold-atom experiments". In: *Phys. Rev. A* 110 (1 July 2024), p. 013319. DOI: 10.1103/PhysRevA.110.013319. URL: https://link.aps.org/doi/10.1103/PhysRevA.110.013319.

[135] A. Thiel. "The Landau-Zener effect in nuclear molecules". In: *Journal of Physics G: Nuclear and Particle Physics* 16 (1990).

[136] H. Voit et al. "Molecular orbital formation and Landau-Zener transitions in the $^{13}C + ^{12}C$ collision". In: *Nuclear Physics A* 476 (3 1988).

[137] G.E. Murgida, D.A Wisniacki, and P.I. Tamborenea. "Landau-Zener transitions in a semiconductor quantum dot". In: *Journal of Modern Optics* (2009).

[138] Clarence Zener. "Non-adiabatic crossing of energy levels". In: *Proceedings of the Royal Society of London: A Mathematical, Physical and Engineering Sciences* (1932).

[139] O.Atabek, R. Lefebvre, and M. Jacon. "Semiclassical multistate curve-crossing models: Reduction of the transition amplitudes to diabatic and adiabatic phase integrals". In: *Journal of Chemical Physics* (1984).

[140] C.E.Carroll and F.T. Hioe. "Transition probabilities for the three-level Landau-Zener model." In: *J. Phys. A* (1986), p. 2061.

[141] A. Ivanov, M. Matteini, and M. Nemevšek et al. "Analytic thin wall false vacuum decay rate". In: *J. High Energy Phys.* (2022).

[142] P. B. Wigley et al. "Non-destructive shadowgraph imaging of ultra-cold atoms". In: *Opt. Lett.* 41.20 (2016), pp. 4795–4798. DOI: 10.1364/OL.41.004795. URL: https://opg.optica.org/ol/abstract.cfm?URI=ol-41-20-4795.

[143] M. Koashi and M. Ueda. "Exact eigenstates and magnetic response of spin-1 and spin-2 bose-einstein condensates". In: *Phys. Rev. Lett.* (2000).

[144] J. Lovegrove, M.O. Borgh, and J. Ruostekoski. "Energetically stable singular vortex cores in an atomic spin-1 Bose-Einstein condensate". In: *Phys. Rev. A* (2012).

[145] J. Lovegrove, M.O. Borgh, and J. Ruostekoski. "Stability and internal structure of vortices in spin-1 Bose-Einstein condensates with conserved magnetization". In: *Phys. Rev. A* (2016).

[146] A.P.C. Underwood et al. "Properties of a nematic spin vortex in an antiferromagnetic spin-1 Bose-Einstein condensate". In: *Phys. Rev. A* (2020).

[147] H. Takeuchi. "Phys. Rev. Lett." In: *Quantum Elliptic Vortex in a Nematic-Spin Bose-Einstein Condensate* (2021).